Adaptive Tire Model
For Dynamic Tire-Road Friction
Force Estimation

by

Jonathan Spike

A thesis
presented to the University of Waterloo
in fulfillment of the
thesis requirement for the degree of
Master of Applied Science
in
Mechanical Engineering

Waterloo, Ontario, Canada, 2013

AUTHOR'S DECLARATION

I hereby declare that I am the sole author of this thesis. This is a true copy of the thesis, including any required final revisions, as accepted by my examiners.

I understand that my thesis may be made electronically available to the public.

Abstract

As vehicle dynamics research delves deeper into better insights in performance, modeling, and vehicle controls, one area remains of utmost importance: tire and road friction forces. The vehicle's interaction with the road remains the dominant mean of vehicle control. Ultimately, the tire-road interaction will determine the majority of the vehicle's capabilities and as the understanding of the interface improves, so too can the performance.

With more computationally intensive systems being instrumented into modern vehicle systems, one is able to observe a great deal of important vehicle states directly for the remaining vehicle information; excellent estimation techniques are providing the rest of the insights. This study looks at the possible improvements that can be observed by implementing an adaptive dynamic tire model that is physical and flexible enough to permit time varying tire performance. The tire model selected is the Average Lumped LuGre Friction Tire Model, which was originally developed from physical properties of friction and tire systems.

The material presented here examines the possibility of an adaptive tire model, which can be implemented on a real-time vehicle platform. The adaptive tire model is just one section of an entire control strategy that is being developed by General Motors in partnership with the University of Waterloo. The approach allows for estimated and measured vehicle information to provide input excitation for the tire model when driven with real-world conditions that enabling tire estimations. The tire model would then provide the controller information indicating the expected tire capacity and compares it with the instantaneous loading. The adaptive tire model has been tested with flat road experimental cases and the results provided reasonable estimates. The experimentation was performed with a fully instrumented research vehicle that used in-wheel force transducers, and later repeated with a completely different non-instrumented fully electric vehicle.

The concepts and investigation presented here has initiated the ground work for a real-time implementation of a full adaptive tire model. Further work is still required to evaluate the influence of a range of operating conditions, tire pressure, and of different tire types. However, the findings indicate that this approach can produce reasonable results for the specified conditions examined.

Acknowledgements

During my graduate career, I have been fortunate to have received help by outstanding individuals. These individuals have guided my career and have helped move me toward a more confident and capable person.

Dedication

To my wife, father

&

in loving memory of my mother.

Their love, strength, and perseverance have been my beacon of aspiration. Their combined support and motivation have propelled me to where I am, for that I am truly thankful.

Table of Contents

List of Figures

List of Tables

Nomenclature

Symbol	Units	Description
σ_0	$[m^{-1}]$	LuGre tire model rubber stiffness
σ_1	$[s/m]$	LuGre tire model rubber dampening
σ_2	$[s/m]$	LuGre tire model relative viscous dampening
μ_s	$[-]$	LuGre tire model static friction
μ_k	$[-]$	LuGre tire model Coulomb friction
V_s	$[m/s]$	Stribeck relative velocity
θ	$[-]$	LuGre tire model road adhesion
κ	$[m^{-2}]$	Distributed correction factor
V_r	$[m/s]$	Relative velocity between the tire and the ground
z_i	$[m]$	Internal friction state in the direction of i
$z_{ss,i}$	$[m]$	Steady-state internal friction state in the direction of i
ω	$[rad/s]$	Wheel rotation rate
V_i	$[m/s]$	Wheel linear velocity at the wheel center in the direction of i
R_e	$[m]$	Effective tire radius
γ_c	$[deg]$	Tire camber angle
F_x	$[N]$	Longitudinal force
F_y	$[N]$	Lateral force
F_z	$[N]$	Vertical force
$F_{ss,i}$	$[N]$	Steady-state force in the direction of i

Chapter 1
Introduction

The modern tire is a deceptively complex device that allows the transfer of power from the vehicle drive train to become useful locomotion. With the exception of some aerodynamics, the only way a passenger vehicle is able to provide any motion, handling, braking, or control is though the tire's interaction with the road's surface. This study examines the passenger tires from the requirement of a control perspective. For a tire to be useful and in the form that a controller might utilize it properly, three major considerations must be met. First, there must be a model that can reasonably represent the important input to output relations of the tire. The relationship to obtain tire forces and force capacity is the main consideration for this study. Second, the model complexity must allow for fast computation in order to be utilized with the controller all the while, keeping as high accuracy as possible. Third, the model needs to be useful in real world applications. That being, the system must allow for components of the model to be time variant though estimation in conjunction with the control system. In order to appreciate the immensity of such a challenge, a developed overview of tires and how studying them has led to such a specific need in modern vehicle dynamics research is first explained.

Passenger vehicle tires are based on the tubeless radial tire concept that comprises of rubber, steel, and fiber systems fused together in a well-orchestrated engineering process. The development of which can be traced back over two centuries with milestones including Robert W. Thompson's work on the first pneumatic tire in 1845 and the invention of the radial tire design in 1946 [1]. Extensive research and development has been investigated in the area of measuring and characterizing tires in order to better understand their limitations and capabilities.

1.1 Motivation

As modern vehicles development improves vehicles safety systems to provide newer and better methods, an increase in information about the vehicle is required. This can include operating condition, the limits that the environment will permit, and the performance limitation of the vehicle itself. In order to mediate this increase in information demand of modern vehicle safety systems, one

must obtain increasingly more accurate models, vehicle dynamics understanding, accurate estimation, and improved sensory information.

The purpose of this investigation is to examine a possible estimation improvement with a vehicle tire model. The intention is, the more information known regarding the tire and the capabilities it has with the ground at any point in time, the more effective vehicle stability and energy management systems can be. This would lead to the potential that one could intelligently control a vehicle without exceeding the physical limits that the tire-road interface presents, thus improving safety and vehicle control. The ramifications of such an insight would allow safety systems to be used to a maximum potential, for braking or collision avoidance. Furthermore, an optimal energy usage can be employed to capitalize on the benefit of knowing which wheel is capable of delivering more force and by how much. This potential to distribute the tire loading will allow for better cornering, acceleration, and braking control by applying the required force to the wheels that will optimize the result based on the commanded vehicle maneuver.

1.2 Background

Vehicle control systems such as Anti-lock Brake Systems (ABS), Traction Control Systems (TCS), and Electronic Stability Control (ESC) have been developed to avoid dangerous situations and improve vehicle safety by performing driver-assisted actions. However, these systems are based on a reactive approach, whereby the problem situation has started before the response begins [2]. Alternatively, a vehicle control strategy that utilized knowledge of the current road and vehicle dynamic limitations to proactively and holistically manage the vehicle motion would provide an advantageous vehicle stability approach. Amongst other motivating factors, this control strategy concept has led to the estimation work being examined as part of Holistic Cornering Control (HCC).

1.2.1 Full Vehicle Research Project and Connected Material

The central concept is that the vehicle dynamics development work is being improved around the Holistic Cornering Control. The HCC is a control concept that has the objective to match the desired forces and torque at the vehicle's center of mass from a reference signal. The reference signal can be obtained from the driver command interpreter (DCI), where the desired forces and torque values are

obtained through the observation of the driver's inputs and relating them to the vehicle's current state. Once the HCC has been provided a reference objective, the most energy efficient way of reaching this objective is normally preferred with the exception of emergency maneuvers. This control operation must be done without compromising stability or the vehicle's responsiveness.

During normal driving, with good to ideal road conditions, this objective is not unreasonable. However, when the vehicle is operating close to the limits, either through aggressive driving or less than ideal road conditions, then the task becomes significantly more complex. The most notable challenge is the limitation of the tire friction capacity. Hence, a strategy was devised to provide the necessary insight: that being to utilize a Full Vehicle Estimation (FVE) and Adaptive Tire Model. Figure 1 is provided to visualize the connected structure described. The FVE provides the required observations of the force loading that each wheel undergoes, while the Adaptive Tire Model provides insight into the limitations of the individual wheels. These two systems work harmoniously, as shown in Figure 2.
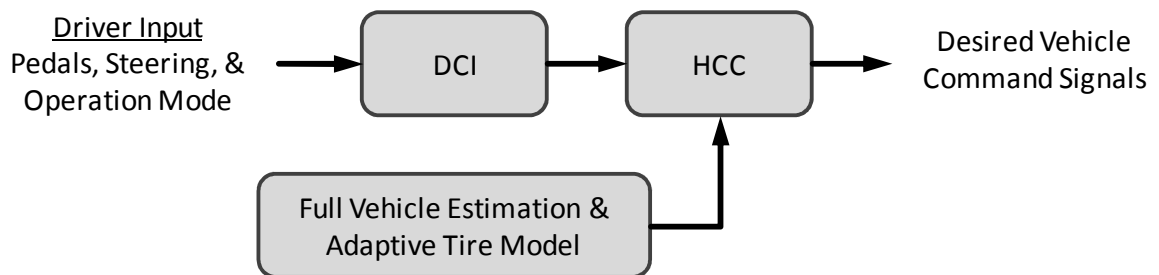
Figure 1: High Level Component Structure and Flow of Signal Information

1.2.2 The Full Vehicle Estimation Overview

The Full Vehicle Estimation is a parallel research topic that was developed in conjunction with the Adaptive Tire Model concept deliberated within. The purpose of FVE was to have an algorithm that was capable of estimating vehicle states and parameters normally required by safety, control, and driver assistance applications. The component that makes FVE especially suited for the Adaptive Tire Model was that the entire approach does not include a tire model. Instead, the estimation separates the

results into the kinematic and kinetic components. The structure of the approach was designed to be modular, allowing for different fidelity models and a diverse sensor set while still maintaining the basic function. The utilization of this estimation will be discussed in subsequent sections.

1.2.3 Interconnected Estimation Approach

The unification of the FVE with the Adaptive Tire Model would allow the tire model to bridge the discrepancies between the kinematic and kinetic components of the vehicle motion. To accomplish this, individual tires are considered the fusion point between the two estimated results and are adjusted though state and parameter identification. By relating the independently calculated kinematic and kinetic components, the tire model can be provided input excitation from one system and be compared against the results of the other. Thus, allowing the means for an Adaptive Tire Model structure that implements parameter identification and provides the possibility of online implementation. Figure 2 has been provided to illustrate the interconnectivity described.
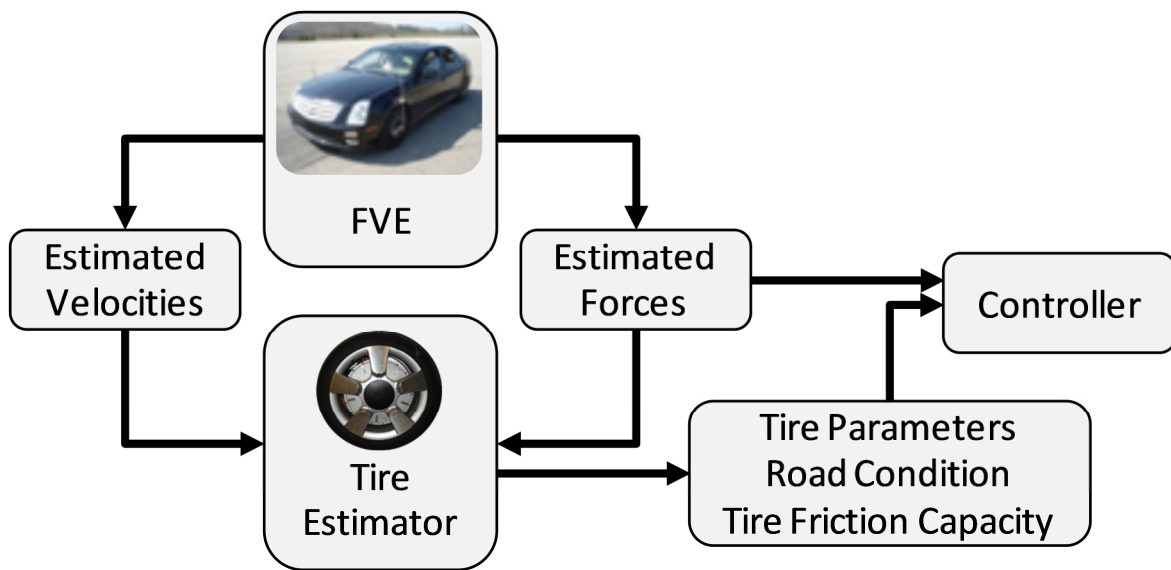
Figure 2: Full Vehicle Estimation and Adaptive Tire Model Estimation Structure

This approach eliminates the static predefined tire model system and can be made to account for many changes that the wheels will experience throughout the vehicle's lifetime. Additionally, by

allowing each tire to be individually adjusted, the vehicle can observe changes that affect the driving performance in real would scenarios. For instance, the vehicle can experience split mu road surfaces or have different tire wear, age, and type. All the while, this structure permits the flexibility to account for such varied conditions.

1.3 Problem Statement and Objectives

The objective is to investigate the possibility of developing an Adaptive Tire Model that can be used to determine friction capacity limitations for individual wheels on a production vehicle. In order to ascertain this target objective, one is required to develop an understanding of the tire model that would best suit the control needs and fit the objective outlined. Then, one must evaluate the estimation capabilities of the model with an estimation approach both in simulation and experimentally. The subsequent section outlines this document and explains the steps taken to achieve the objective.

1.4 Thesis Outline

The current chapter is the first of six presented in this thesis. This chapter initiates the topic of tire friction force modeling and estimation, while providing insight into the importance of this work.

Chapter 2 begins the discussion of the tire modeling and describes the approaches that have been developed, meanwhile revealing fundamental concepts required to understand tire friction force modeling. Additionally, this chapter will introduce the background information needed to grasp the estimation that is used with the tire model throughout this thesis.

Chapter 3 provides insight into the estimation approach and details into how the entire process can work in simulation. Here, the selected model is examined in detail and connected with vehicle simulation software package to discover the effects of the estimation and accuracy possible in simulation.

Chapter 4 explores the real world application of the developed approach. This is done by examining the model and estimation techniques with a vehicle that is fully instrumented. Such instrumentation includes sensors that are not available on production vehicles.

Chapter 5 brings together the culmination of work from a joint research endeavor. This chapter discusses the results when the tire model is provided with input information from a full vehicle estimation system instead of direct instrumentation data.

Chapter 6, the final chapter, concludes the thesis by summarizing the findings and providing culminating remarks. The chapter includes insights for future progress and possible development ideas gained from this study.

Chapter 2
Literature Study

This chapter pertains to the literature with regards to tire modeling and estimation techniques that relates to the subsequent sections below. The chapter begins with a general background on tire modeling, followed by the tire modeling that is similar to the selected model used for the remainder of this study. Next, the literature study includes Kalman Filter techniques that will be used in conjunction with the tire model. And lastly, an overview of the development that relates directly with the objective and the methods selected throughout this investigation is provided.

2.1 Tire Models: A General Overview

While there have been many that have put significant effort into modeling tires and into discovering the general behaviors, one individual is frequently referred to or compared against. Pacejka's work on the tire modeling is extensive and can be seen in his works "Tyre and Vehicle Dynamics" [3] along with his other collaborative works as seen in [4, 5]. Pacejka describes in [3] the general response of the tire behavior, more specifically, the steady-state response compared with the tire slip. This general modeling known as the 'Magic Formula' as shown in Equations (2.1) and (2.2) [5], and is based on empirical data such as observed in [4].

$$Y = Dsin\big(C\ arctan(B\phi)\big) + S_y \qquad (2.1)$$

$$\phi = (1 - E)(X + S_h) + (E/B)\arctan\big(B(X + S_h)\big) \qquad (2.2)$$

Where: B = Stiffness Factor   C = Shape Factor,
         D = Peak Factor   E = Curvature Factor,
         S_h = Horizontal Shift S_y = Vertical Shift

This generic form of the Magic Formula can be used to provide a steady-state response that directly related the tire slip to the longitudinal force, as shown in Figure 3. The parameters selected for Figure 3 are selected for the longitudinal force with a 6kN load found in [5]. This response has several key components that are highly useful in control modeling and understanding the control limitations.

Figure 3 also illustrates the particular components of interest: the linear region, peak friction force, and the saturation region. While driving on a dry asphalt or pavement surface, most driving is performed within the linear region of the tire response, as Carlson noted: "During ordinary driving …the tire slip rarely exceeds 2%." [6]. However, during more aggressive maneuvers or when driving on less than ideal road conditions one may surpass the peak force that the tire is expected to provide. This can result in instability, sliding, and a condition where vehicle control strategies may fail; hence knowing a tire's response can be advantageous to a vehicle stability control strategy.
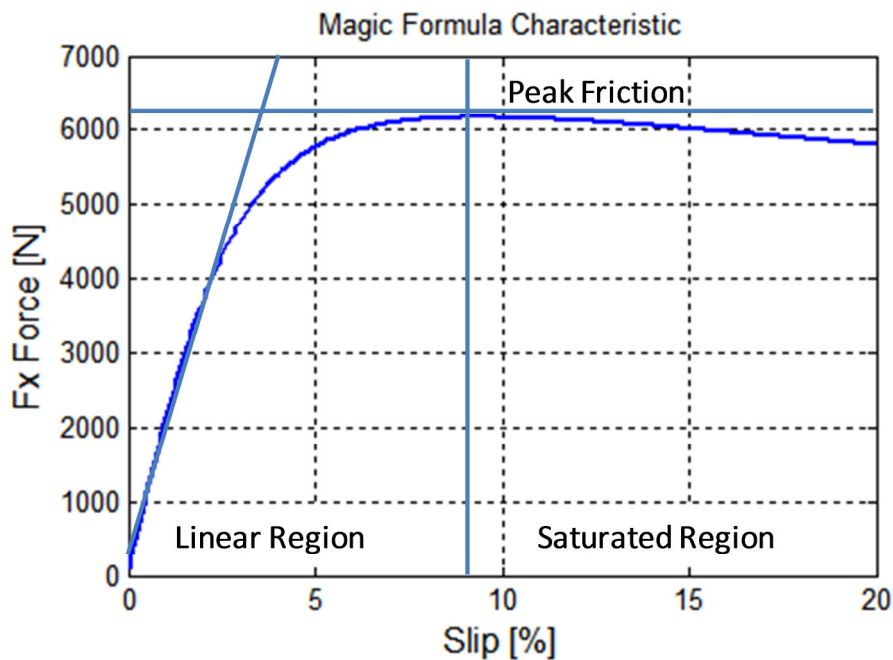
Figure 3: Magic Formula Characteristic Response

In the case of the Magic Formula, the steady-state response is a function of tire slip on the road surface. As a result, when the wheel slip changes, so too does the expected force. The tire's slip is defined in Equations (2.3) and (2.4). In either braking or driving cases, the relative velocity V_r is being utilized in the same way [7]. The relative velocity is defined as V_r with the component V_x in terms of the tire coordinate frame. Furthermore, the slip is characterized as being between -1 and +1 from the wheel being fully locked during braking, to the wheel fully skidding during driving, respectively. Similarly, in the rare case of pure rolling condition, the slip is evaluated as being equal to zero.

8

$$Slip_{drive} = \frac{V_r}{R_e \omega} = \frac{R_e \omega - V_x}{R_e \omega} \quad V_x < R_e \omega, \qquad Drive\ Case: R_e \omega \neq 0 \qquad (2.3)$$

$$Slip_{brake} = \frac{V_r}{V_x} = \frac{R_e \omega - V_x}{V_x} \quad V_x > R_e \omega, \qquad Brake\ Case: V_x \neq 0 \qquad (2.4)$$

By utilizing the slip in this form, the braking case is provided as a negative slip. This is, however, different than some literature that would normally have the braking case with positive slip [7]. This approach allows for a more intuitive and natural form of slip that allows for comparisons considering driving and braking cases simultaneously. Similarly, slip in the lateral direction can be defined as the slip angle α_{slip}. The lateral slip, frequently noted in degrees, is the angle between the tire's longitudinal velocity and the tire's lateral velocity as defined in Equation (2.5).

$$\alpha_{slip} = \arctan\left(\frac{V_y}{V_x}\right) \qquad (2.5)$$

In order to visualize the tire and the tire coordinates, Figure 4 has been provided from [8] and uses the diagram developed within [4]. Figure 4 illustrates: γ_c as the wheel camber angle, α_{slip} as the lateral slip angle, and ω as the wheel rotation rate.
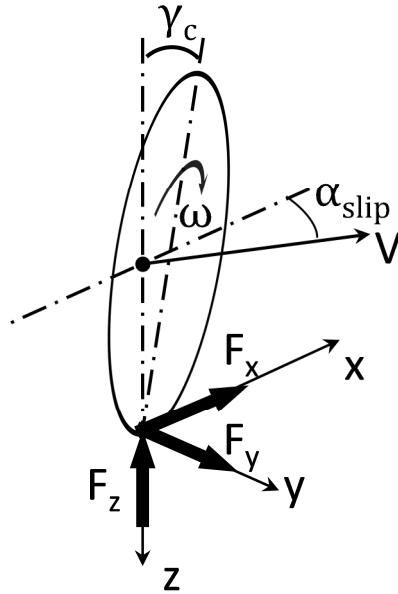
Figure 4: Tire Coordinate System and Related Components

Beyond the basic linear tire model or the Magic Formula, several other tire models have been proposed. Some approach the problem with a semi-empirical solution much like the TMeasy model [1], while others attempt a physical tire model such as the TreadSim model [1]. Further still, a highly detailed tire model approach with numerical analysis such as FEM can prove highly accurate and provide great detail with regards to tire behavior. Each of these models, however, have their advantages and disadvantages and need to be selected based on the desired application. The semi-empirical approach can yield highly accurate results for a very specific set of conditions. Unfortunately, as noted in [9], these models are difficult to extend to include the effect of inflation pressure, operating temperature, speed performance changes, tire wear, and tire age. On the other hand, the highly accurate numerical approach can be defined for nearly any operating condition and configuration imagined. The disadvantage is that the accuracy gained comes at the cost of computational complexity. For the purpose of defining an adaptive tire model to meet the outlined objective, a physical model that characterizes the key components with reasonable complexity and accuracy is the desired approach.

10

2.1.1 Combined Tire Slip Response

The combined longitudinal and lateral tire force response is defined differently for various tire models and approaches. However, a common method of evaluating the combined friction characteristics is to utilize the friction ellipse. Pacejka was also able to determine the friction ellipse structure with the Brush model, and observed that: "Often, the shape appears to be more asymmetric than predicted by the simple brush model. This may be due to a slight increase in the contact length while braking (making the tire stiffer)..." [3]. Others, E. Velenis for instance, directly utilized the elliptical response in a successful extension of the LuGre model to include the coupled longitudinal and lateral force response [10, 11].

2.1.2 Physical Tire Models

The basic structure of the tire model is to provide an estimate of force in the longitudinal and lateral directions, along with the self-aligning moment. Each of these components are calculated based on the input as shown in Figure 5.

Inputs   Outputs

Wheel Slip   Longitudinal Force F_x
Camber angle γ ⟶ Tire Model ⟶ Lateral Force F_y
Vertical Force F_z Self-Aligning Moment M_z
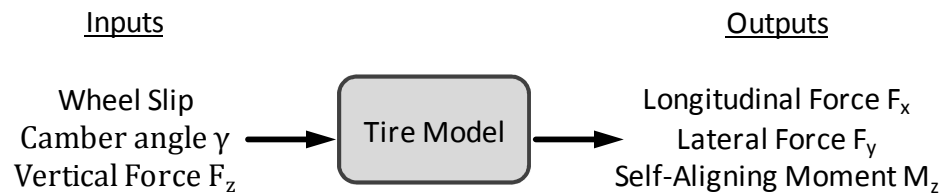
Figure 5: Tire Model Basic Input and Output

Within the physical tire model group, several different approaches exist. There is the Brush model, as described by Pacejka in [3], where the tire is assumed to have multiple contact points that are deflected as the tire is loaded. This approach allows for an analysis that can approximate the two dimensional force components and the self-aligning moment when utilizing a non-uniform normal load distribution. However, the model is limited to the steady-state condition. The steady-state is seldom the case in reality, particularly when the vehicle is experiencing changes in loading as it is during vehicle maneuvers. One model that attempts to overcome this limitation is the Dahl model noted in [12, 13], the model includes transient properties. The Dahl model is based on the stress-strain

curve from classical solid mechanics with the inclusion of Coulomb friction [7]. However, the Dahl model is not able to accurately produce the peak results observed with the Magic Formula empirical approach. Alternatively, the LuGre model continues the insights discovered by the Dahl model that combines the tire deflection and tire rate of deflection, with the relative velocity of the contact patch to form a more comprehensive physical tire model.

2.1.3 The LuGre Tire Model

The LuGre model, much like the Dahl model, allows for the effects of hysteresis loops and pre-sliding tire displacement. This is possible by the fact that the model considers a bristle point contact with the ground and includes the properties of a spring and a damper. Additionally, the model permits the parameters to have physical meaning and can be used to observe changes in road characteristics such as dry and wet conditions [13]. The model parameter components are provided in Table 1 for reference, and Figure 6 provides a visual representation of the LuGre tire model.
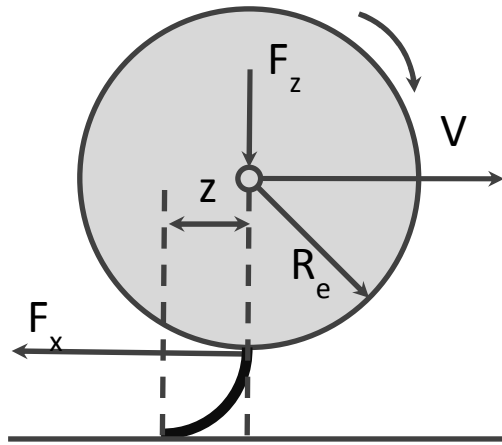
Figure 6: Braking Phase, LuGre Friction Tire Model Deflection

The initial LuGre dynamic friction model used in the context of a tire model was described by [13, 14] with Equations (2.6) to (2.8). The use of $\gamma = \frac{1}{2}$ instead of $\gamma = 2$ in Equation (2.8) was a variation compared with the general LuGre friction model [15]. This modification was done to allow for an improved estimate of the LuGre steady-state characteristics to better suit that of the Magic Formula.

12

$$\dot{z} = V_r - \frac{\sigma_0 |V_r|}{g(V_r)} z \tag{2.6}$$

$$F = (\sigma_0 z + \sigma_1 \dot{z} + \sigma_2 V_r) F_n \tag{2.7}$$

$$g(V_r) = \mu_k + (\mu_s - \mu_k) e^{-\left|\frac{V_r}{V_s}\right|^{\gamma}} \tag{2.8}$$

Table 1: LuGre Parameters and Physical Characteristic Definition

Parameter	Parameter Definition
σ_0	rubber longitudinal lumped stiffness
σ_1	rubber longitudinal lumped damping
σ_2	viscous relative damping
μ_k	normalized Coulomb friction
μ_s	normalized Static friction
V_s	Stribeck relative velocity
F_n	normal force
V_r	relative velocity
z	internal friction state

The point contact friction behavior is shown in Equation (2.8), describing the response as a function of relative velocity. This behavior utilizes the Stribeck effect shown in Figure 7, where the friction response is a nonlinear function. Within Figure 7, the terms F_c and F_s are defined as the Coulomb friction force and the maximum static friction force, respectively. These two friction forces transition by the Stribeck effect as defined by the Stribeck speed V_s and the Stribeck exponent γ, typically $\gamma \in [0.5, 2]$, [8].
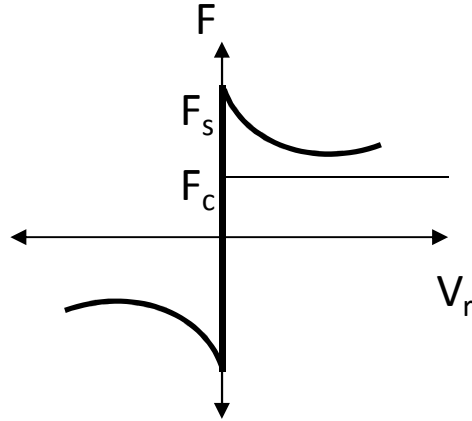
Figure 7: Friction Response as a Function of Velocity

Unfortunately, the proposed model does not account for a significant component that alters the general behavior of the tire dynamic response. The contact patch significantly affects the tire output. However, by considering this model with multiple bristles over the entire contact patch as described in the Distributed LuGre Friction model, one can improve the model performance.

2.1.4 Distributed LuGre Tire Model

By accounting for the distribution of vertical loading over the tire's patch, the Distributed LuGre Tire Model can provide more accurate results comparable to FEM analysis. This is accomplished by considering the form of Equations (2.6) to (2.8) in the application of multiple bristle contact points over the patch length. Then, the process of integrating the individual bristle elements yields the desired result. Equations (2.9) to (2.10) shows the modified form required [7].

$$\frac{dz}{dt}(\zeta, t) = V_r - \frac{\sigma_0 |V_r|}{g(V_r)} z(\zeta, t) \tag{2.9}$$

$$F = \int_0^L dF(\zeta, t) = \int_0^L \left(\sigma_0 z(\zeta, t) + \sigma_1 \frac{\partial z}{\partial t}(\zeta, t) + \sigma_2 V_r \right) dF_n(\zeta) \tag{2.10}$$

By following the steps and process described by [8], the tire deflection variable z is a function of both the discreet integral deflection element (ζ) and time (t) as shown in Equation (2.11).

14

$$\frac{dz}{dt}(\zeta, t) = \frac{\partial z(\zeta, t)}{\partial \zeta} d\zeta + \frac{\partial z(\zeta, t)}{\partial t} dt \qquad (2.11)$$

$$\frac{d\zeta}{dt} = R_e |\omega| \qquad (2.12)$$

Inserting Equations (2.11) and (2.12) into Equation (2.9) produces the partial differential Equation (2.13) [7, 8, 14].

$$\frac{dz}{dt}(\zeta, t) = V_r - \frac{\sigma_0 |V_r|}{g(V_r)} z(\zeta, t) - R_e |\omega| \frac{\partial z(\zeta, t)}{\partial \zeta} \qquad (2.13)$$

And lastly, following the steps noted in [7] and substituting Equation (2.14) to Equation (2.10), produces the final output force described in (2.15).

$$dF_n(\zeta) = f_n(\zeta) d\zeta \qquad (2.14)$$

$$F = \int_0^L \left(\sigma_0 z(\zeta, t) + \sigma_1 \frac{\partial z}{\partial t}(\zeta, t) + \sigma_2 V_r \right) f_n(\zeta) d\zeta \qquad (2.15)$$

The distributed form of the LuGre model separates the contact patch length into ζ-elements that are then integrated with predetermined normal load and determined element deflections. This is however, impractical for use with most tire applications due to the unknown normal load distribution. This limitation can be overcome by directly measuring the normal load or by reasonable approximation. The approximation approach is used to define the Average Lumped LuGre Friction Tire Model discussed next.

2.1.5 Average Lumped LuGre Tire Model

The Average Lumped LuGre Friction Tire Model provides a compact representation of the distributed model previously described. This can be accomplished by assuming a normal load distribution simplification and representing the collective tire deflection as an average tire deflection. The current

literature discusses several approaches, however, the three main approaches to simplify the normal distribution are presented. The lumped model form replaced Equation (2.13) with Equation (2.16) [7] and reused the originally proposed structure shown in Equations (2.7) and (2.8), where κ accounts for the distributed estimations/assumptions made.

$$\dot{z} = V_r - \frac{\sigma_0 |V_r|}{g(V_r)} z - \kappa R_e |\omega| z \tag{2.16}$$

The first approach assumes a constant term, κ, to account for the normal load distribution. The second, is to assume a time varied uniform load distribution, $\kappa(t)$, that is adjusted based on the tire deflection, z. The last approach is to assume an asymmetric trapezoidal normal load distribution profile. By utilizing the trapezoidal shape, the equation then "…satisfies the associated boundary conditions and allows the effects of the pneumatic trail to appear" [11], thus accounting for the tire self-aligning moment as a further extension of the tire model.

The constant κ-estimate described in [7] can be first approximated by using a parabolic distribution estimate. Setting the boundary conditions to have zero tire deflection results in the Equation (2.17), where L is the contact patch length.

$$\kappa = \frac{2}{L} \tag{2.17}$$

Canudas-de-Wit continues by indicating a more realistic approach, which allows for the deflection to gradually build along the patch length, yielding the result provided in Equation (2.18) [7].

$$\kappa = \frac{7}{6}\frac{1}{L} \approx 1.16667\frac{1}{L} \tag{2.18}$$

Furthermore, by considering the use of sliding and adhesion region results in an acceptable range, where: $1/L \leq \kappa \leq 2/L$ [7], or as suggested by Tsiotras, the range should be smaller $1.1/L \leq \kappa \leq$

16

$1.4/L$ [16]. Meanwhile, the uniform normal load distribution approach that utilizes the tire deflection to account for loading is defined in Equation (2.19) [7, 16].

$$\kappa_i = \frac{1 - e^{-L/z}}{1 - \frac{z}{L}(1 - e^{-L/z})}, \qquad where: \kappa = \frac{\kappa_i}{L} \qquad (2.19)$$

The resulting difference was minimal as Tsiotras noted, only a slightly faster convergence to the expected response of the distributed form of the model was observed, compared with the constant κ approach [16]. Deur notes that $\kappa_i \in [1, 2]$ and that the constant factor κ of approximately 1.2 can adequately be used in place of the uniform load estimation approximation noted in Equation (2.19) instead [8]. The last distribution described provides an approach that can logically extend the model to include the aligning moment and allows the moment to contain a sign change during higher lateral slip as observed in practice [11]. Figure 8, illustrates several methods considered for the normal load distribution contained within [16], yet the asymmetric trapezoidal approach proved to be reasonable and effective for calculations. This approach is used to determine the steady-state tire deflection Z_{ss} that is then directly applied to Equation (2.20) in order to solve for κ_{ss}. Lastly, κ_{ss} is used in Equation (2.16) instead of κ as the steady-state approximation of the load distribution factor.

$$\kappa_{ss} = \frac{1}{R_e|\omega|}\left(\frac{V_r}{Z_{ss}} - \frac{\sigma_0|V_r|}{g(V_r)}\right) \qquad (2.20)$$
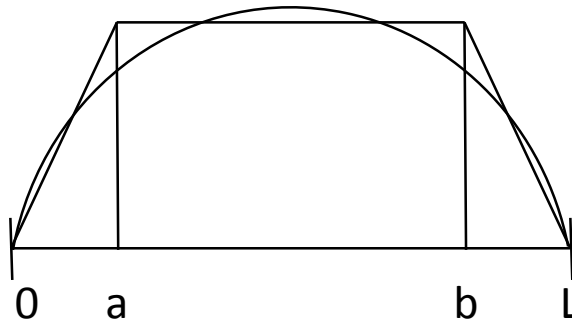
Figure 8: Normal Load Distribution Forms along the Patch Length

17

However, the variation as a result of the camber angle is omitted in each of these distribution models. The advantage of the trapezoidal model or a variation on such an approach (as provided in [16]) is that the model fidelity can be improved by providing adequate insight into the tire normal load distribution. The normal load profile can be significantly different laterally compared with longitudinally. Similarly, the lateral profile will need to be adjusted based on which side of the vehicle the wheel is on. As the left side tire and right side tire can move mirrored to one another the resulting normal load profile that is affected by suspension and camber angles, will be mirrored too. In order to limit the possibilities considered within this thesis, both the camber angle correction and the self-aligning moment estimation are not included.

2.2 Kalman Filter

The Kalman Filter is an estimation technique that is for a: "linear, discrete-time, and finite-dimensional system" [17]. The Kalman Filter utilizes a linear model, direct measurement, and linear optimization calculations to approximate the value being estimated. The estimation process was introduced by R. Kalman in 1960 [18] and provides an excellent solution to Gaussian noise distribution problems. While it is not possible to directly apply the Kalman Filter to a nonlinear system such as a nonlinear tire model, different approaches can overcome this limitation. Three such solutions are noted to account for the linear limitation of the Kalman Filter. The first is to consider a globally linearization of the model that can directly be applied within the Kalman Filter. This process can often be effective for nearly linear systems that have a dominant operating point. However, this approach suffers from the major disadvantage of assuming a single operating point where linear assumption was made. Alternatively, the second approach expands on the idea of the first. The Extended Kalman Filter (EKF) allows the model to be linearly estimated at each time-step around the current estimation point. This second method allows a nonlinear model to be linearly approximated as needed, while utilizing the effective Kalman Filter estimation structure. The third and last approach discussed, is the Unscented Kalman Filter (UKF), originally proposed by Julier [19]. The UKF method draws from the advantages of the Kalman Filter optimization concept without linearization. The UKF does this by directly utilizing the nonlinear function and propagating multiple data points at each time step. However, the work presented will examine the possible implementation of the last two

Kalman Filter approaches discussed; the general form for each method follows the original Kalman Filter structure.

The Kalman Filter structure and the connected information can be observed in Figure 9. As shown, the Kalman Filter is outlined by a dashed line while the input and measurement signals drive the recursive estimator. The plant may be either a physical system or a virtual model that the Kalman Filter will try to estimate the model states and track the plant output. The approach calculates a gain known as the Kalman Gain, which is directly applied to the error between the measured signal and the model's calculated output signal. This gain is obtained by finding the minimum mean-square estimate based on the covariance matrices [17].
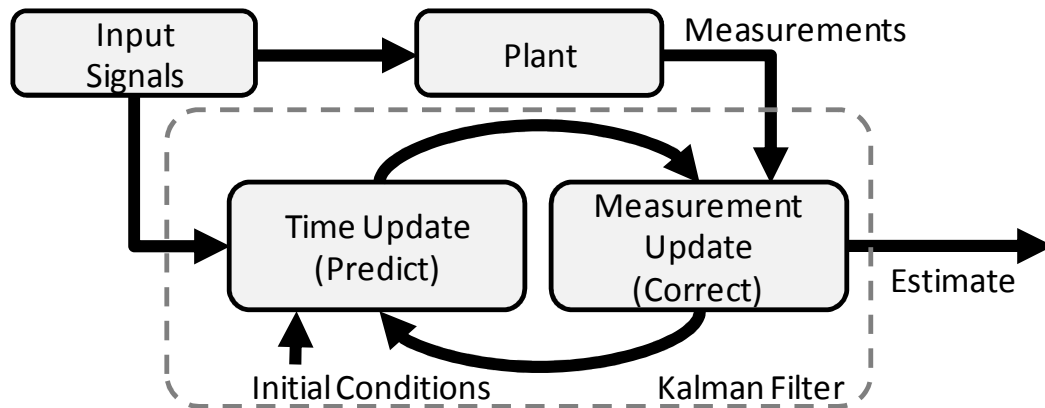
Figure 9: Kalman Filter General Structure

In general, this method can produce excellent results and is extremely fast to compute, hence, making the Kalman Filter and its variations highly desirable for many diverse estimation applications.

2.2.1 Extended Kalman Filter

As suggested by the name, the Extended Kalman Filter is an extension of the method discussed in the previous section. The purpose of the EKF is to apply the methods of the Kalman Filter to a non-linear model without first linearly estimating the model about a single operating point. The EKF linearization occurs at each discrete-time step, through the use of Jacobian matrices. Table 2 contains the equations that define the EKF approach.

The EKF utilizes the first order Taylor series estimate of the nonlinear function [17] and can be applied easily to many applications. The Jacobian calculation is often computationally the most complex task of the EKF and can be the greatest limiting factor since the EKF cannot be applied when the partial derivative is without a unique solution. In these cases, further approximations or modifications to the model are needed to allow the EKF to be utilized. This is because the EKF estimates by propagating the mean value through the linearly approximated motion model and measurement models. The results are then evaluated with the covariance to estimate the mean value. Alternatively, the next section describes the nonlinear solution that does not require the linear estimate of the model and propagates multiple data points to converge on the estimated value.

Table 2: Extended Kalman Filter Equations [20] [21]

EKF Initialize:

$$\hat{x}_0 = E[x_0] \tag{2.21}$$

$$P_{x_0} = E[(x_0 - \hat{x}_0)(x_0 - \hat{x}_0)^T] \tag{2.22}$$

Time-update equation, where k $\in$ {1,..., ∞}

$$\hat{x}_k^- = F(\hat{x}_{k-1}, u_{k-1}, v) \tag{2.23}$$

$$P_{x_k}^- = A_{k-1} P_{x_{k-1}} A_{k-1}^T + B_k R^v B_k^T \tag{2.24}$$

Measurement-update equations

$$K_k = P_{x_k}^- C_k^T \left(C_k P_{x_k}^- C_k^T + D_k R^n D_k^T \right)^{-1} \tag{2.25}$$

$$\hat{x}_k = \hat{x}_k^- + K_k [y_k - H(\hat{x}_k^-, \bar{n})] \tag{2.26}$$

$$P_{x_k} = (I - K_k C_k) P_{x_k}^- \tag{2.27}$$

Where

$$A_k \triangleq \left. \frac{\partial F(x, u_k, \bar{v})}{\partial x} \right|_{\hat{x}_k}, \quad B_k \triangleq \left. \frac{\partial F(\hat{x}_k^-, u_k, v)}{\partial v} \right|_{\bar{v}}$$

$$C_k \triangleq \left. \frac{\partial H(x, \bar{n})}{\partial x} \right|_{\hat{x}_k}, \quad D_k \triangleq \left. \frac{\partial H(\hat{x}_k^-, n)}{\partial n} \right|_{\bar{n}} \tag{2.28}$$

And where R^v and R^n are the covariance of v_k and n_k, respectively. Additionally the noise means are denoted by $\bar{n} = E[n]$ and $\bar{v} = E[v]$, are usually assumed to be zero.

Matrix B and D are often simplified to the [I].

2.2.2 Unscented Kalman Filter

Another adaptation of the Kalman Filter is the Unscented Kalman Filter. The unscented transformation (UT) was applied to the Kalman Filter to obtain the UKF approach. This technique utilizes a minimum number of sigma points [19] [21] around the current mean value to propagate through the nonlinear function. The resulting distribution is used to find a weighted mean and covariance of the output. These sigma points are then propagated through the function and are evaluated to find the output mean and output covariance. [22]

The UKF requires additional parameters to configure how the estimation technique will be performed. These parameters, in conjunction with the covariance, will define how the sigma points are distributed around the mean value. Equations (2.29) to (2.31) define the weighted values for the mean and covariance, as part of the equations that describe the UKF calculation process.

$$\lambda = \alpha^2 (L + \kappa) - L \tag{2.29}$$

$$W_0^m = \frac{\lambda}{L + \lambda}, \ W_0^c = \frac{\lambda}{L + \lambda} + (1 - \alpha^2 + \beta) \tag{2.30}$$

$$W_i^m = W_i^c = \frac{\lambda}{2(L + \lambda)}, \qquad i = 1, \dots, 2L \tag{2.31}$$

Typically, α is defined as being very small between 1 and 10^{-4} and affects the distribution of sigma points. Meanwhile, β is normally equal to 2 as noted for optimal values with Gaussian distributions. And lastly, κ is a secondary scaling parameter, often $\kappa = 0$ or $\kappa = 3 - L$ [19, 20, 21]. However, if $\kappa < 0$ then the weight, W_0, can result in the covariance being calculated as non-positive, semi-definite and may require adjusting [22]. The equations that define the rest of the UKF are provided in Table 3 for the case where the noise has zero mean value.

UKF Initialize:

$$\hat{x}_0 = E[x_0] \tag{2.32}$$

$$P_{x_0} = E[(x_0 - \hat{x}_0)(x_0 - \hat{x}_0)^T] \tag{2.33}$$

Calculate sigma points:

$$\mathcal{X}_{k-1} = \left[\hat{x}_{k-1}, \qquad \hat{x}_{k-1} + \gamma \sqrt{P_{x_k}}, \qquad \hat{x}_{k-1} - \gamma \sqrt{P_{x_k}} \right] \tag{2.34}$$

Time-update equation, where $k \in \{1, ..., \infty\}$

$$\boldsymbol{\mathcal{X}}_k = F(\mathcal{X}_{k-1}, u_{k-1}) \tag{2.35}$$

$$\hat{x}_k^- = \sum_{i=0}^{2L} W_i^{(m)} \boldsymbol{\mathcal{X}}_{i,k} \tag{2.36}$$

$$P_{x_k}^- = \sum_{i=0}^{2L} W_i^{(c)} [\boldsymbol{\mathcal{X}}_{i,k} - \hat{x}_k^-][\boldsymbol{\mathcal{X}}_{i,k} - \hat{x}_k^-]^T + R^v \tag{2.37}$$

$$\boldsymbol{\mathcal{Y}}_k = H[\mathcal{X}_k, u_k] \tag{2.38}$$

$$\hat{y}_k^- = \sum_{i=0}^{2L} W_i^{(m)} \boldsymbol{\mathcal{Y}}_{i,k} \tag{2.39}$$

Measurement-update equations:

$$P_{\hat{y}_k \hat{y}_k} = \sum_{i=0}^{2L} W_i^{(c)} [\boldsymbol{\mathcal{Y}}_{i,k} - \hat{y}_k^-][\boldsymbol{\mathcal{Y}}_{i,k} - \hat{y}_k^-]^T + R^n \tag{2.40}$$

$$P_{\hat{x}_k \hat{y}_k} = \sum_{i=0}^{2L} W_i^{(c)} [\boldsymbol{\mathcal{X}}_{i,k} - \hat{x}_k^-][\boldsymbol{\mathcal{Y}}_{i,k} - \hat{y}_k^-]^T \tag{2.41}$$

$$K_k = P_{\hat{x}_k \hat{y}_k} P_{\hat{y}_k \hat{y}_k}^{-1} \tag{2.42}$$

$$\hat{x}_k = \hat{x}_k^- + K_k[y_k - \hat{y}_k^-] \tag{2.43}$$

$$P_{x_k} = P_{x_k}^- - K_k P_{\hat{y}_k \hat{y}_k} K_k^T \tag{2.44}$$

And where: R^v and R^n are the covariance for process and measurement noise, respectively.

2.3 Relevant Research Applications

By understanding and making note of past research, one can improve on ideas that have been previously developed. This section discusses three projects that are of interest as they pertain to the objective outlined by this thesis. The research examines the potential to implement various forms of the LuGre friction model with different estimation techniques.

The first publication noted is by A. Asadian et al. with the paper "A Compact Dynamic Force Model for Needle-Tissue Interaction" [23]. Asadian examines how a modified version of the LuGre friction model can be applied to medical research. Needle-tissue interaction modeling is combined with an EKF estimation approach. The EKF was able to provide promising results in order to resolve both the state estimation and the parameter estimation simultaneously. The second publication of interest examines the simulation of the LuGre friction model applied with the use of vehicle dynamics simulation software CarSim®. Chen and Wang [24], apply a recursive least squares algorithm to estimate the term that relates to the ground condition. Similarly, the third publication by Canudas-de-Wit and Horowitz [12], with the application of a Lyapunov-based approach, tries to use the same tire model. These last two approaches indicate that the ground condition parameter can be observed. However, the tire model used in both does not account for the patch conditions noted in the tire model previously mentioned. These three publications, however, have been limited to simulation but do indicate that the main parameters can be observed and that the application of the LuGre model with varied parameters is possible.

Chapter 3
Tire Force Estimation Using Adaptive Tire Model

3.1 Introduction

Contained within this chapter is the explanation of the LuGre model selected and the model combined with the estimation approaches. Furthermore, to understand the model and how to best utilize the estimation method, this chapter includes an analysis of the model proposed. This is accomplished three fold: firstly, by examining the behavior and response of the model, secondly, by determining the dominant parameters that contribute to the force response output, and thirdly by evaluating the estimation techniques used with the model to provide insight into the best approach to utilize.

3.2 The Tire Model

The Average Lumped LuGre Friction Tire Model was selected based on the fact that the tire uses physical characteristics for the parameters. The model's ability to account for a variety of road conditions, computing transient tire behavior, and being reasonably compact for real-time implementation make this model an ideal candidate. The equations that describe the one-dimensional form of this model are provided in Equation (3.1) to (3.4) [7] [11], where the subscript i indicates the direction (either x-longitudinal or y-lateral) within the tire coordinate frame. The tire coordinate frame is provided in Figure 10, conforming to the SAE convention, and is based on a similar figure from Pacejka [3]. This is the reason for the negative terms to be combined with the vertical force in Equation (3.4), since the vertical force will be less than zero.

Additionally, one should note that the linear velocity being considered is located at the wheel centre. Hence, the tire model described is in agreement with the general tire model description discussed in Chapter 2.
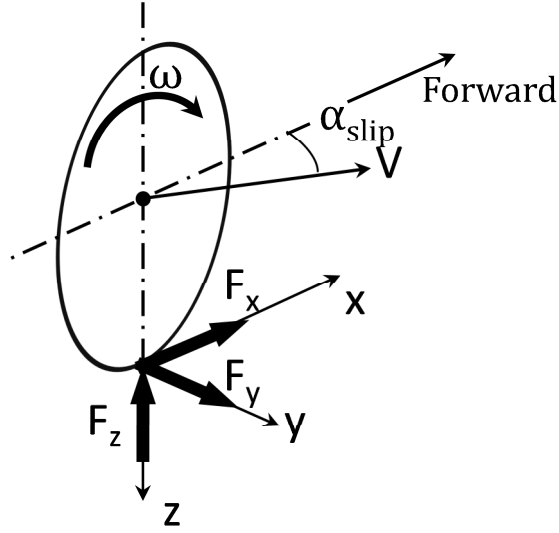
Figure 10: Non-Rotational Tire Coordinate and Component Diagram

$$\dot{z}_i = V_{ri} - C_0 z_i \tag{3.1}$$

$$C_0 = \frac{\sigma_{oi}|V_{ri}|}{\theta g(V_{ri})} + \kappa_i|\omega|R_e \tag{3.2}$$

$$g(V_{ri}) = \mu_{ki} + (\mu_{si} - \mu_{ki})e^{\left|\frac{V_{ri}}{V_s}\right|^\gamma} \tag{3.3}$$

$$F_i = (-\sigma_{0i}z_i - \sigma_{1i}\dot{z}_i - \sigma_{2i}V_{ri})F_z \tag{3.4}$$

As for the relative velocity V_{ri} in the longitudinal and lateral direction, each component is calculated independently. Equations (3.5) and (3.6) provide the relative velocity equation based on the tire coordinate system.

$$V_{rx} = R_e\omega - V_x \tag{3.5}$$

$$V_{ry} = V_y = V_x\tan(\alpha_{slip}) \tag{3.6}$$

This form of the LuGre model used the assumption of the uniform normal load distribution, which assumed a constant value for κ_i. By utilizing the principle described in the literature [7] [11], κ_i is defined as being within a range governed by the length of the contact patch (L_i) in the related

25

direction. The relation between the load distribution compensation term (κ_i) and the length of the contact patch (L_i) is defined in Equation (3.7). This study utilized the $\kappa_i = (7/6)(1/L_i)$ version as noted in [7], where the constant scaling term $\kappa_0 = 7/6$.

$$\kappa_i = \frac{\kappa_0}{L} \; where \; \frac{1}{L_i} \le \kappa_i \le \frac{2}{L} \tag{3.7}$$

An additional consideration taken in the model definition includes the method in which the parameter Θ was utilized. The selected approach defined Θ as the road adhesion parameter [7]. Alternatively, Θ would have been inversely defined as $\Theta^* = 1/\Theta$, where Θ^* refers to the Road Classification Factor [12] [24]. Equation (3.8) provides the ranges for these two definitions of Θ and Θ^*.

$$0 < \Theta \le 1 \le \Theta^* \tag{3.8}$$

In both cases, the ideal condition is a value of one. However, the Θ adhesion definition has two distinct advantages over the alternative. Firstly, the parameter has an upper and lower bound separate from any physical limitation, thus helping with the identification and estimation process. Secondly, the adhesion definition is more intuitive as Θ decreases, so too does the capability of the tire's force output. This second detail is observed in Table 4, which provides the physical meaning of the different Θ values.

Table 4: Physical Meaning of Tire Model Θ Parameter [7] [25] [14]

Θ^*	Θ	Physical Connection
1	1	Ideal Road Condition
2	1/2	Rain/Wet Condition
4	1/4	Snow Condition
6	1/6	Very poor, Ice Condition

Lastly, the γ parameter that is used to define part of the response within Equation (3.3), characterizes the transition from μ_s to μ_k. This is assumed to be one. While this value has been noted to be both ½ and 2 by [7] [25] depending on the desired implementation, the value of γ can be varied. The parameter selection specified is based on that of [11] from the parameter matched results, and will assume that the transition shown in Figure 11 will be accounted for by the remaining terms

26

within Equation (3.3) instead. In order to attain a confident definition of γ, one needs a detailed characterization of the particular tire being investigated; such is not the case here.

Contained within Figure 11, are the results of the three values normally associated with γ, as already noted. In Figure 11 (A), one can observer that the general trend moves the value of $g(V_r)$ to a constant value of μ_k in this case $\mu_k = 0.93$. However, Figure 11 (B) provides the general result within a more practical operating region. Considering the case where the wheel is moving at 50km/hr and with a slip ratio of 0.3, this will only result in a relative velocity of 4.17m/s during braking conditions. Hence, only in very extreme cases will the relative velocity be significantly larger than 5m/s. Consequently, the general trend considered is minimally altered by the slight change in γ. In order to reduce the number of parameters requiring identification, the assumed value of one is perceived to be reasonable for γ.

(A) (B)
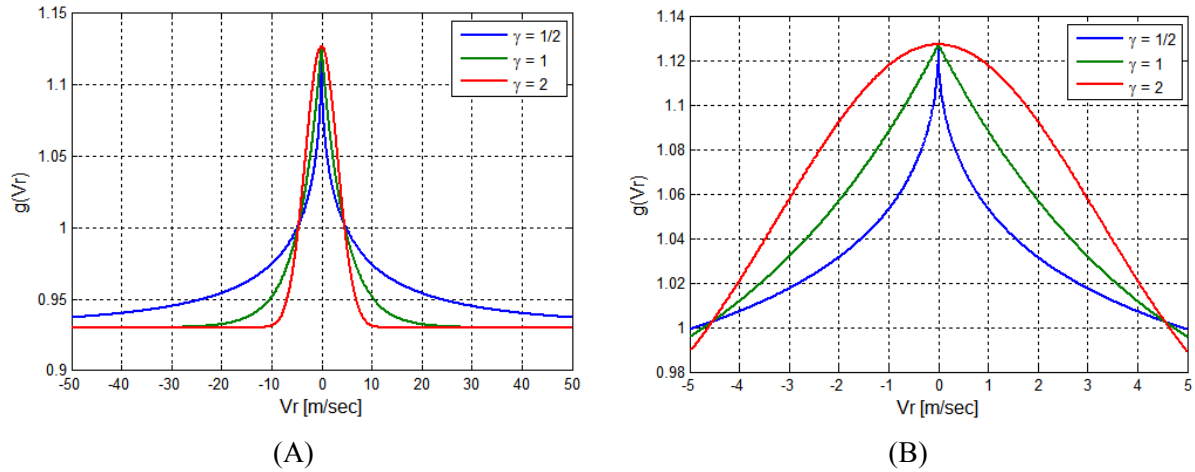
Figure 11: Response of g(V$_r$) with Varied γ

Now that the model selection and reasoning is established, one requires insight into the dominant characteristics of the model to best understand how to implement an estimation approach with the systems.

3.3 Steady-State Tire Model and Analysis

The steady-state form of the LuGre Friction Tire Model allows one to compare the response with other well-known models such at the Magic Formula. The process of obtaining the steady-state model

requires the evaluation of $\dot{z}_i = 0$, (3.9) and solving for z as $z_{ss,i}$ from Equation (3.1). This results in Equation (3.10) and can allow for $F_{ss,i}$ as shown in Equation (3.11) [11].

$$\dot{z}_i = 0 = V_{ri} - C_0 z_{ss,i} \tag{3.9}$$

$$z_{ss,i} = \frac{V_{ri}}{\frac{\sigma_{oi}|V_{ri}|}{\theta g(V_{ri})} + \kappa_i |\omega| R_e} \tag{3.10}$$

$$F_{ss,i} = (-\sigma_{0i} z_{ss,i} - \sigma_{2i} V_{ri}) F_z \tag{3.11}$$

For example, the steady-state form of the LuGre friction tire model can be seen in comparison with the data available from CarSim® for a standard D-Class sedan as shown in Figure 12. The CarSim® modeling software and the process of matching the model to the data provided is explained in subsequent sections. The normalized force information is defined as the longitudinal (F_x) and lateral (F_y) force components that are divided by the absolute vertical load (F_z). Furthermore, each case is considered separately with pure longitudinal and pure lateral slip case to define the results of Figure 12.
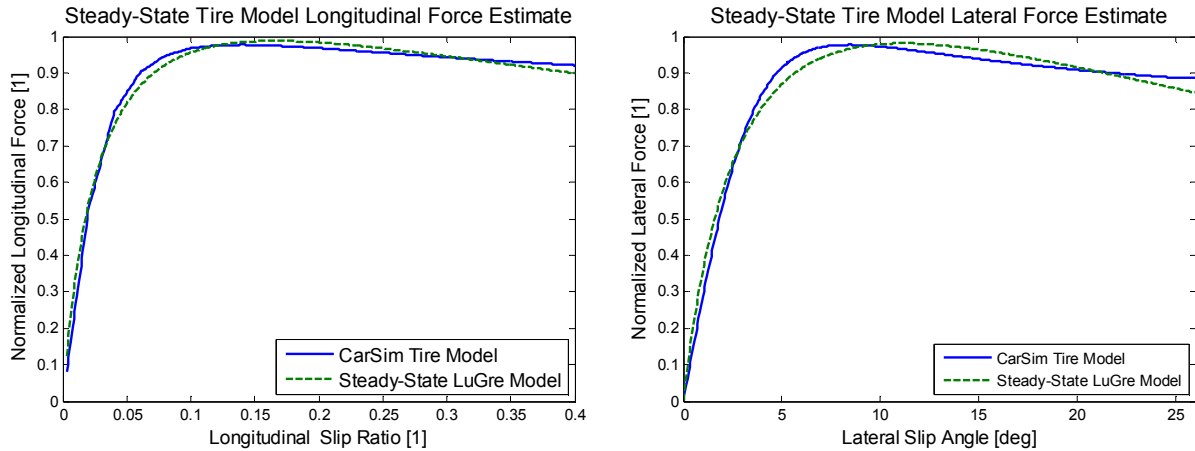
Figure 12 CarSim and LuGre Model Normalized Steady-State Response

The comparison in Figure 12 is made with the longitudinal velocity assumption of 50km/hr and a vertical load of 4400N. This resulted in an absolute error of less than 4.2% along the entire slip response.

In order to determine the dominant parameters, a local parameter evaluation is considered by performing a partial differentiation of the steady-state form of the model. This approach considers the results of the output of the partial differential equation over a range of velocities and slip conditions. This approach is limited to the local sensitivity performance for the model and therefore a parameter selection was made based on effective model parameters from past studies [7]. Canudas-de-Wit's parameters were selected with the same assumption of a constant κ term, where the term was defined in Equation (3.12). The parameter is defined as $\kappa_0 = 1.2$ [7] while the remaining terms are provided within Table 5.

$$\kappa = \frac{\kappa_0}{L} \tag{3.12}$$

Table 5: LuGre Steady-State Parameters [7]

Parameter	Value	Unit
σ_0	395.86	m^{-1}
σ_2	0.0012	s/m
μ_s	1.127	1
μ_k	0.93	1
V_s	4.553	m/s
L	0.2	m
κ	6	m^{-2}
θ	1	1
R_e	0.325	m

For the detailed results of the steady-state analyses of the partial derivatives refer to Appendix A, where the description and plotted results can be found. However, to summarize the findings: the two most significant terms by considering the greatest magnitude of response over the operating region were R_e and σ_2. These two terms are followed by the subsequent θ, μ_s, and μ_k parameters that all have a similar order of response, but noticeably different profiles. Due to the nature of Equation (3.3) and the fact that the relative velocity is governed by slip characteristics, one can expect that μ_s and μ_k will have a complementary behavior as slip varies. Sure enough, this complement is noticeable as μ_k has the greatest contributions with the greatest slip values. Inversely, μ_s contributes the most with minimal slip and also with all very small velocities. Additionally, the parameter θ is the term that has

been characterized to govern the overall response of the function as the tire model experiences diverse road conditions. As a result, one expects Θ to have a noticeable contribution to the function output and throughout the entire operating region. This is the case and would suggest that the parameter Θ is the third most significant term to consider. Finally, the remaining parameters appear to have little contribution to the function output. This would suggest that the model is less sensitive to variations in the κ and V_s parameter selections.

These findings would suggest that the parameters R_e, σ_2, and Θ would be the most important parameters to consider when performing parameter identification. This is because these values have the greatest impact over the entire operating region. Notable consideration must be given when identifying μ_s and μ_k as these two parameters impact the system with the same order of magnitude as Θ. Furthermore, one can notice that the partial differentiation of the parameter (with the exception of σ_2) have discontinuous cases. These discontinuities may prove a limiting factor and should be considered when performing and examining the limitations of estimation approaches. Fortunately, the discontinuities are all either at zero velocity or zero slip, and may allow for a simple modification to compensate for these conditions. This would be reasonable since real world operation near both problem areas are dominated by noise and are not conducive for parameter estimation.

The final component of interest with the steady-state model is the tire deflection state. By considering the model and coordinates described within this chapter allows for the tire model to make physical sense with the steady-state tire deflection, whereby the resulting deflection is predominantly proportional to the steady-state force [1]. This relationship can be observed by examining Figure 13 and Figure 14.
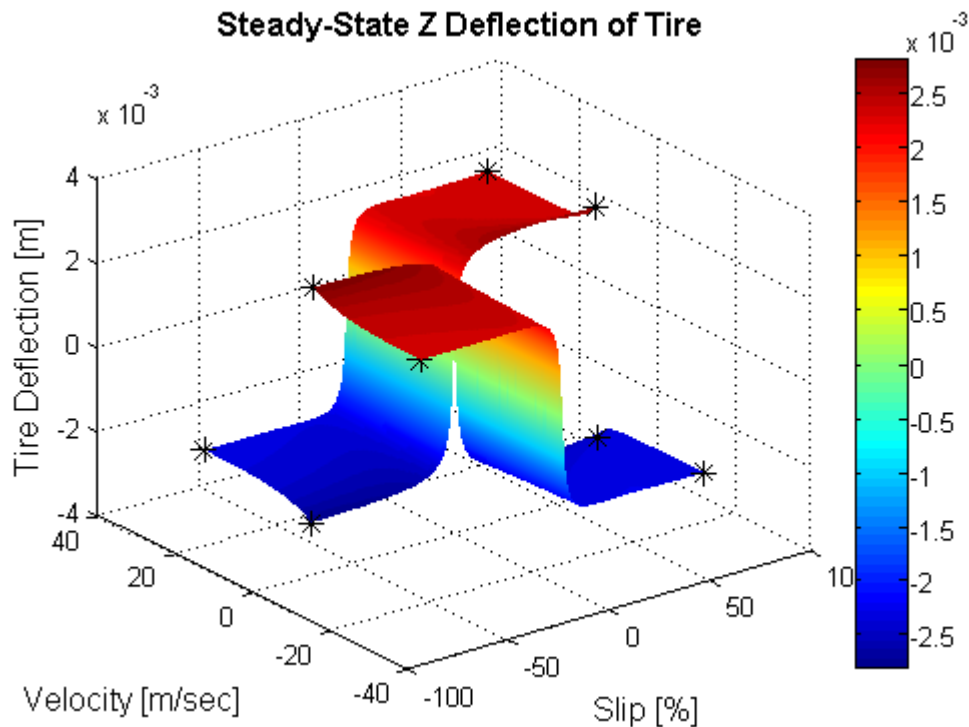
Figure 13: LuGre Tire Model, Steady-State Tire Deflection

Moreover, the steady-state deflection provides insight into the expected magnitude that the model will generate. In this case, a tire deflection of less than ±4mm is a physical possibility and is not in violation of any observable phenomenon. This adds credence to the tire model.

Furthermore, when one examines the results of Figure 13, one can notice how the deflection appears to have two surface responses. This is the result of considering the tire model for both forward and backward motion. In fact the surfaces are joined at one point, that being at zero slip and zero velocity. This is the result of the tire physically deforming as the force in a particular direction increase and cannot instantaneously deflect in the other direction. Instead the tire model indicates that a particular tire deflection will not instantaneously change directions without having to reduce the speed to zero first. The same phenomenon can be observed with the steady-state friction force considered in Figure 14.

31
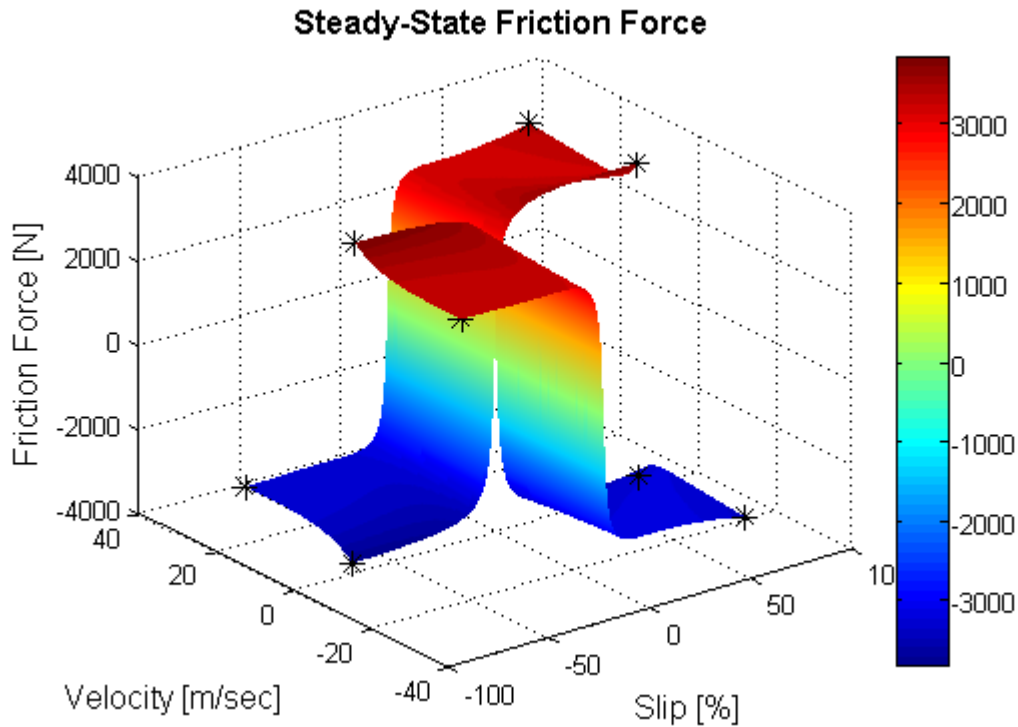
Figure 14: LuGre Tire Model, Longitudinal Steady-State Force

Additionally, Figure 14 provides insight into the fact that the tire model force response varies with respect to velocity. This can be observed by examining how the force response along the surfaces varied even when examining the response with a constant slip ration. The force response, much like the partial derivatives, is limited by a discontinuity at the zero velocity condition. This shortcoming is a common limitation shared by many tire models governed by a slip excitation [26].

3.4 Estimation with Tire Model

Based on the conclusion of the previous sections, the tire model parameters will be separated into two groups, the parameters that are assumed constant and the estimated set. The estimated set will include the tire state Z_i along with θ, R_e, and σ_2. To begin with, an artificial sinusoidal input signal was used to examine both the dynamic model response and to provide the estimation approaches with rich and persistent excitation [27].

32

3.4.1 Simulated Model Excitation: Rich Signal Input

The artificial sinusoidal input signal selected for exciting the tire dynamics model with rich, persistent excitation [27] is described. This excitation method was also selected to make note of numerical limitations of the model when using a time step conducive for real-time applications.

The artificial signal is selected to allow the wheel to be moving at a nominal velocity with the changing input resembling a driver modulating the accelerator pedal position continuously. The artificial signal's actual excitation is defined by Equations (3.13) to (3.15) and the resulting longitudinal force will be considered as feedback information.

$$V_x = R_e \omega(t)\big(1 - Slip_d(t)\big), \qquad where\ \omega(t) = \omega_1(t) + \omega_2(t) \tag{3.13}$$

$$\omega_1(t) = \frac{55}{6}\sin\left(\frac{t}{2}\right) + \frac{50}{3}, \qquad \omega_2(t) = \frac{5}{6}\sin\left(\frac{3t}{2}\right) + \frac{50}{3} \tag{3.14}$$

$$Slip_d(t) = \frac{9}{200}\sin\left(\frac{2}{5}t\right) + \frac{3}{50}, \tag{3.15}$$

The artificial sinusoidal input was applied to the model and the calculation for the state was compared with different numerical methods. Figure 15 and Figure 16 have been provided to illustrate how the different approaches affected the motion.

The performance of the three methods used: Euler, Heun, and Runge–Kutta (RK) [28] were effectively identical when compared with a time interval of 1 msec. This too can be said for the tire deflection when applied with a 10 msec time interval. Figure 15 shows three approaches with minimal appreciable difference in state.

33
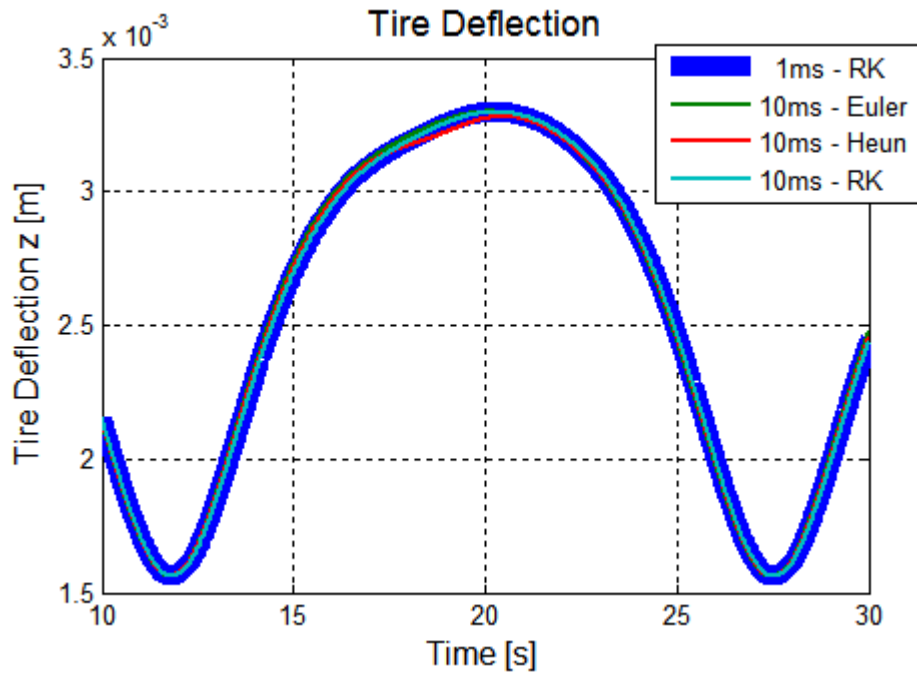
Figure 15: Numerical Evaluation of Tire Model Deflection

However, the tire model's rate of deflection required the use of higher order numerical solvers to provided reasonably consistent data. This would suggest that the RK approach will need to be sued with further application of this tire model. Figure 16 has been provided to clearly illustrating this numerical shortcoming. As a result, the estimation approaches have been modified to include the RK approach within the Kalman filter motion model. This is most notable applied to the Jacobian calculation required within the EKF. The evaluation and results of the estimation techniques for the aforementioned excitation, along with the remaining two, have been provided within the subsequent sections.
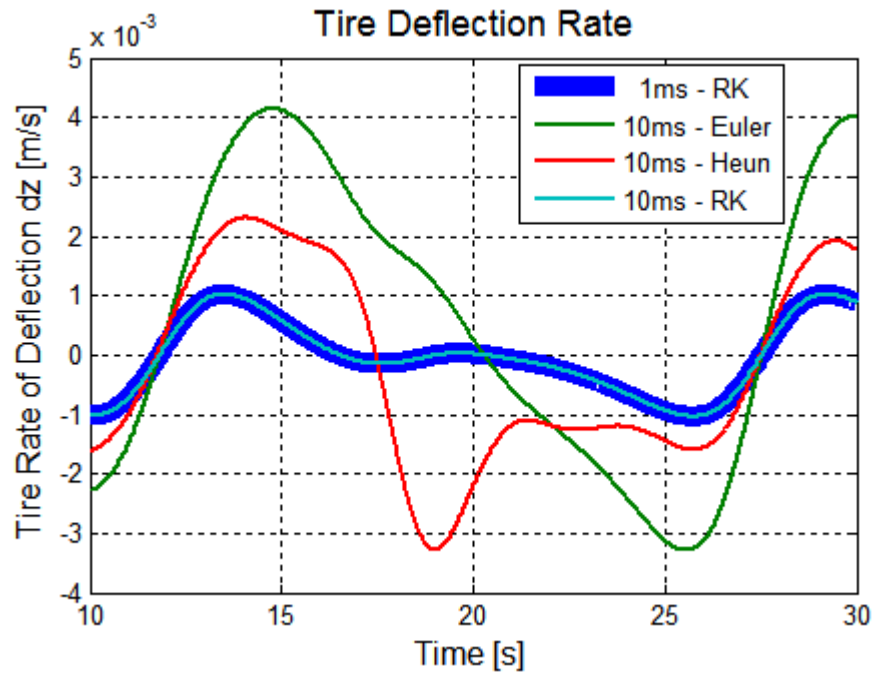
Figure 16: Numerical Evaluation of Tire Model Deflection Rate

3.4.2 CarSim® Model Excitation for Real World Simulation

As part of the vehicle dynamics research development, modeling software has become quite essential. Once such simulation package used was CarSim®. This software simulator provides a variety of full vehicle models, track test scenarios, vehicle response plots, interconnectivity with external models such as Matlab® or Simulink®, and lastly, it provides a virtual graphical environment as shown in Figure 17. This simulation package had the advantage of allowing for subcomponents to be modeled separately while still retaining the full vehicle behaviors and performances that provided a holistic full vehicle result.

By utilizing the vehicle modeling package, one can obtain realistic vehicle excitation without the inherent complexity or noise challenges that are associated with real vehicle experimentation. The vehicle simulation was used to determine if an estimation approach is effective and what some possible limitations were when examining maneuvers inspired by real world driving.
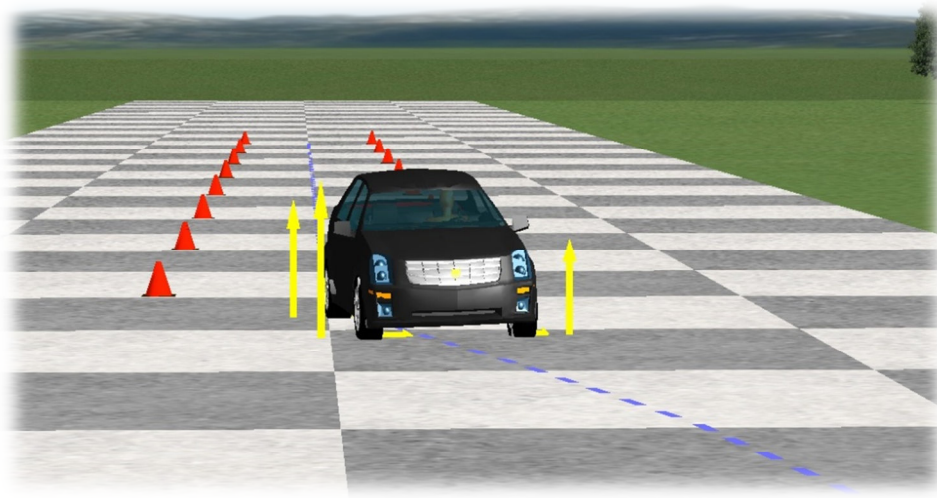
Figure 17: CarSim® Visualization of a Vehicle in a Double Lane Change Maneuver

Just as before, the tire model will be provided with the kinematic excitation at the wheels. The difference now is that the information was directly obtained from the simulation software with the vehicle selection of a D-Class sedan. In an effort to ensure compatibility with the response of the simulation software, the steady-state LuGre tire model components were parameter-matched to the relatable information available within CarSim®. The result was provided in Figure 12, as previously mentioned. The technique of matching the terms made use of a nonlinear least squares algorithm located within the Matlab® function library called 'lsqnonlin'. As a result, the parameters obtained can be noted in Table 6.

The two test cases obtained from CarSim® are as follows:

CarSim® Test 1 - Acceleration and Brake:

The vehicle accelerated from rest with a constant rate of climb assigned to the throttle for the first 10 seconds. Followed by, coasting without pedal input before engaging the brakes at the 15th second. The brakes were maintained at a constant level until the vehicle returned to rest.

CarSim® Test 2 - Hard Braking with ABS Engaged:

The vehicle is initially at a constant speed of 100km/hr and allowed to coast without pedal input. Next, the brake system is abruptly engaged aggressively and remains constant for the remainder of

the test. The loading on the brake is high enough as to activate the ABS system, thus resulting in modulated wheel behavior that can clearly be noticed in the results.

Table 6: Simulation and Estimation Tire Parameters

Parameter	Value	Unit
σ_0	282.087	m^{-1}
σ_2	0.0	s/m
μ_s	1.376	1
μ_k	0.643	1
V_s	6.75	m/s
L	0.19	m
R_e	0.325	m
κ	$\dfrac{7}{6}\dfrac{1}{L}$	m^2

In order for an evaluation of σ_2 estimation capabilities, the optimized version required augmentation. As a result, σ_2 for the estimation will be the same as that found in Table 5.

3.5 Results of Extended and Unscented Kalman Filter Estimation

The Kalman filters used the same configuration for the covariance matrices and were provided with the same excitation, initial conditions and limits. The state limits were used to ensure that the model would remain within a physically possible parameter set. The only notable variation from each test was the initial condition of the state used in the plant and the value is indicated with the respective test case in Appendix A. Otherwise, the parameters and the limits applied to them can be found within Table 7.

Table 7: Simulation Parameters and Condition

Parameter	Plant	Unit	Est. IC	UB	LB
z_x	-	m	0.001	0.005	-0.005
θ	0.9	1	0.70	1.0	1/8
R_e	0.325	m	0.330	0.340	0.310
σ_2	0.0012	s/m	0.0004	0.0048	0.0

For the detailed results of the specific test cases, refer to the following subsections.

3.5.1 Results for Rich and Persistent Excitation Scenario

The testing time for the persistent excitation was selected to be 30 seconds as this time allows the visual convergence of the estimation process to an equilibrium point. The first 15 seconds encompasses any transient behavior, while the remaining 15 seconds illustrates the repeating pattern that generally persists from that time point onward due to the sinusoidal nature of the excitation. Additionally, the plant's initial tire deflection was specified to allow for a smooth tire response with z_{x0} set to 0.0029m.

The results from the persistent excitation test case can be observed within Figure 18 to Figure 23. One can note that the process resulted in an excellent state and force estimation contained within Figure 18and Figure 19 respectively, showing strong pairing between the plant and the respective Kalman filter.
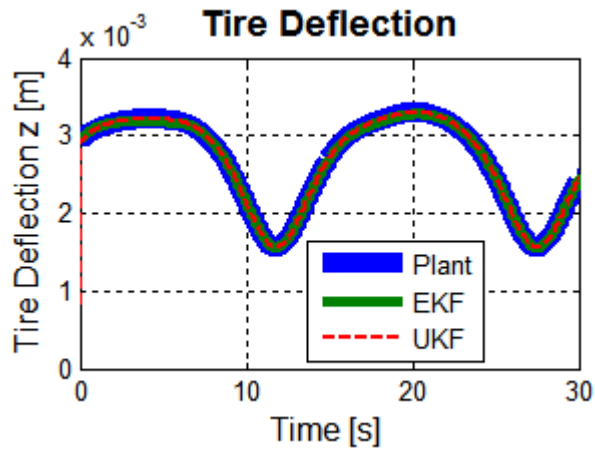
Figure 18: Persistent Excitation - Tire Deflection Estimation

However, the performance of the parameter estimation does vary between the different approaches. Firstly, the parameter defining the road θ was estimated acceptable well for both the EKF and UKF as each converged to within 6% of the target parameter value. See Figure 20 for details. Secondly, the largely dominant parameter R_e was able to be resolved to within a similar accuracy for this test scenario. Figure 21, shows the estimates initially being limited by the boundaries before resolving to remain oscillating between the actual value of R_e and the upper bound.
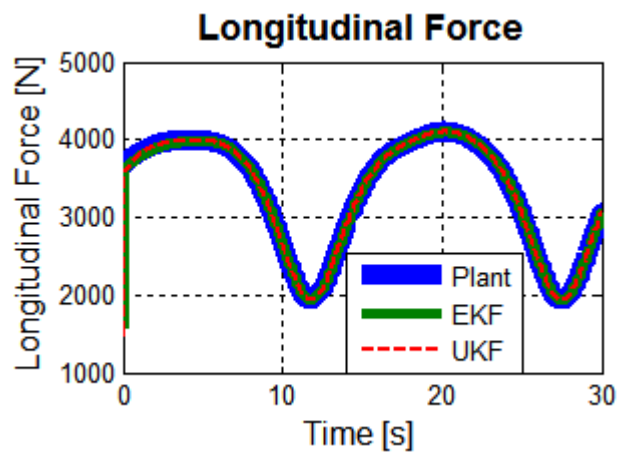
Figure 19: Persistent Excitation - Longitudinal Force Estimation
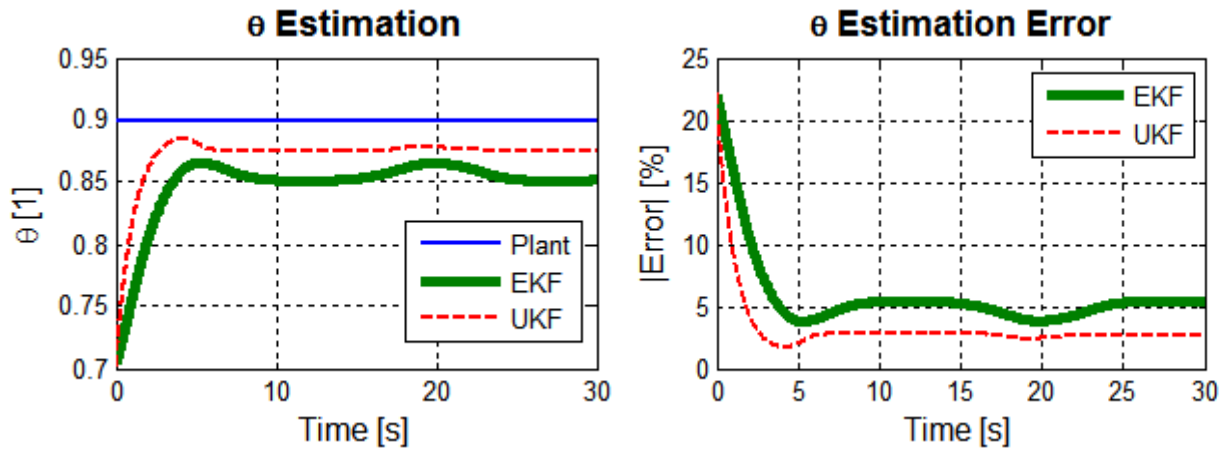
Figure 20: Persistent Excitation - Ɵ Parameter Estimation

Meanwhile, the last parameter shown in Figure 22 provided the greatest difference between the EKF and UKF estimates. The σ_2 estimate performed by the UKF was adjusted nearly immediately and remained for the remaining time. In contrast, the EKF swung dramatically with the predicted value of σ_2 bouncing off of the upper and lower bounds repeatedly.
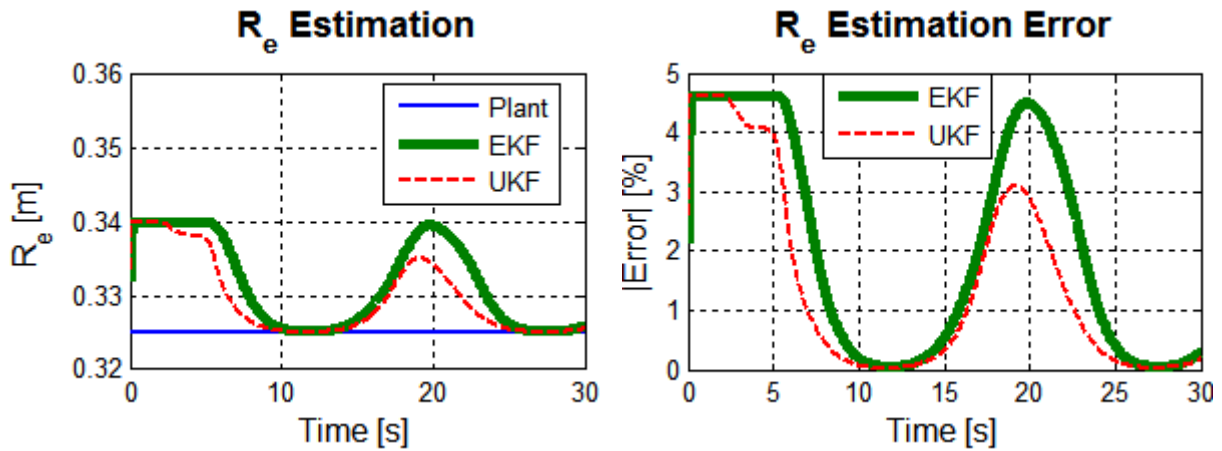
Figure 21: Persistent Excitation - R_e parameter Estimation
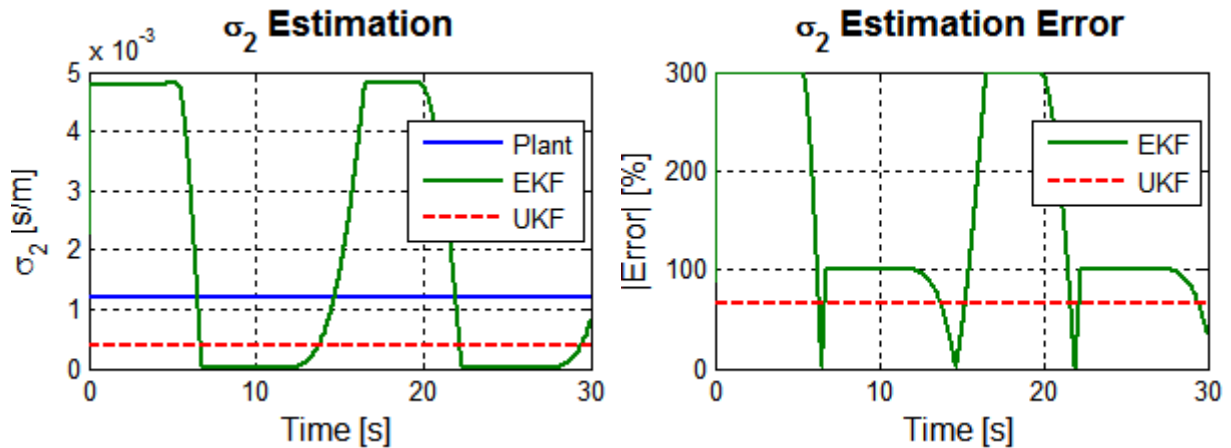
Figure 22: Persistent Excitation - σ_2 Parameter Estimation

Lastly, in order to have a comparable insight into the level of excitation with the subsequent test cases, Figure 23 was provided to indicate the slip experienced during the simulation. By comparing the slip observed with the steady-state response of Figure 12, one can expect that a peak slip ration of 0.1 would excite the peak value of the steady-state model. As a result, any parameters that are directly related to the peak performance of the tire model would likely be easily observed. Fortunately, the parameter ϴ was observed in just such a manner as ϴ can significantly limit the magnitude of the peak friction force.
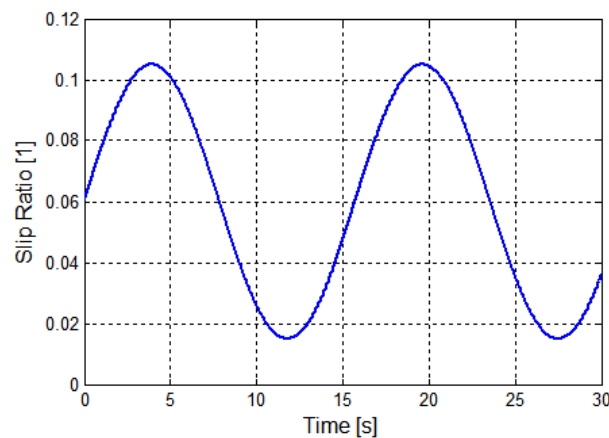
Figure 23: Persistent Excitation - Slip Information

41

For a similar comparison with only three terms: z_x, θ, and R_e, refer to Appendix A for details. This reduced set performed very similarly suggesting that the influence that the EKF experienced with a wide range of σ_2 was minimal to the overall estimation process.

3.5.2 Results for CarSim® Test 1: Acceleration and Brake

The acceleration and brake test resembles the most normal driving behavior that would be examined and will provide insight into real world driving excitation with estimation.
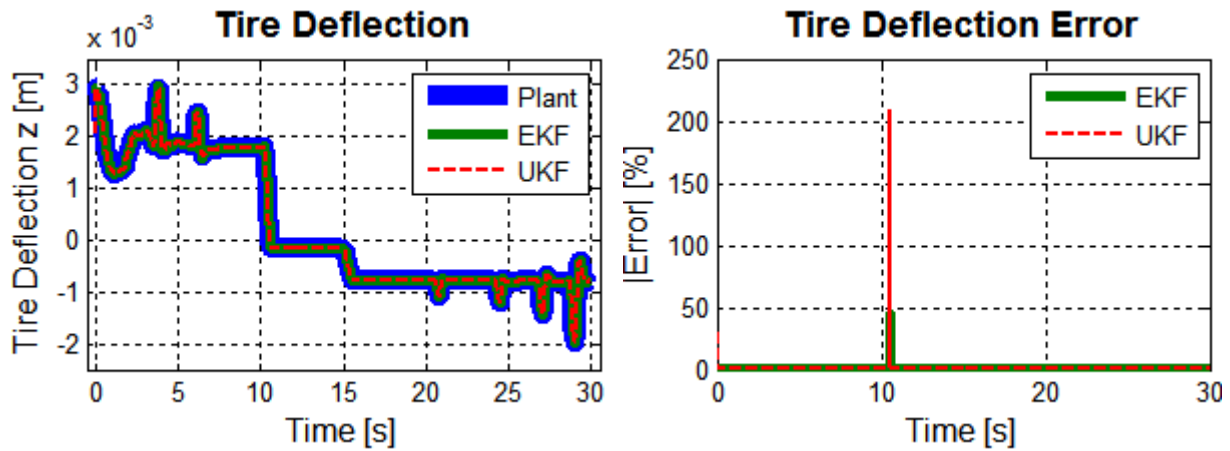
Figure 24: CarSim® Test 1: Acceleration and Brake - Tire Deflection Estimation

Figure 24 shows the state estimation for both techniques are able to accurately replicate the state position of the plant, other than the transition from driving to coasting at t=10 seconds, that resulted in a slight braking condition and spike in the state error. The absolute tire deflection error was maintained to less than 1.5% with both estimations. This high level of accuracy was carried forward to the force estimation shown in Figure 25 suggesting that the estimators do not have difficulty accommodating this level of excitation.
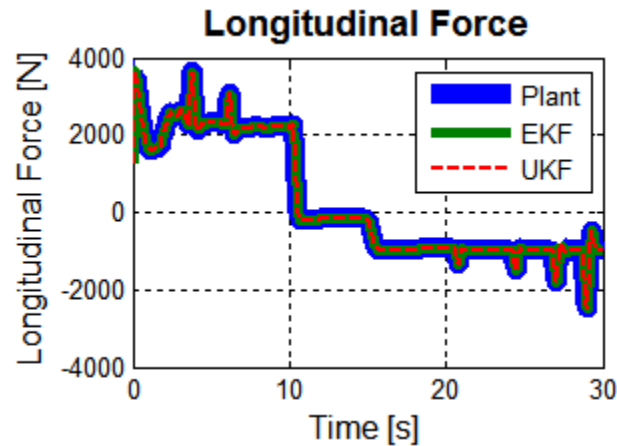
Figure 25: CarSim® Test 1: Acceleration and Brake - Longitudinal Force Estimation

However, the parameter estimation that was performed was not generally as accurate as the state or force estimation. The parameter that was most accurately approximated was the R_e term. Meanwhile the θ parameter showed little to not variation. This might be the result of minimal slip condition allowing the model to operate mainly within the linear tire response region and not exciting the peak performance that would indicate changes in the θ parameter. Figure 26 shows how the slip ratio was minimal throughout the entire maneuver while Figure 27 provides the estimated results.

(A) - Full Time Range   (B) - Initial Slip Response
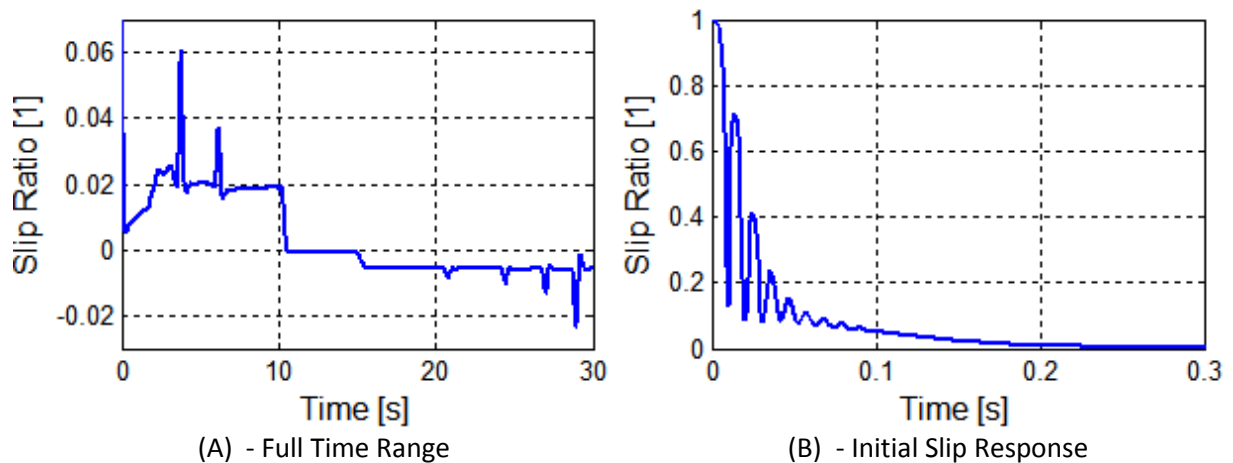
Figure 26: CarSim® Test 1: Acceleration and Brake - Slip Information

The greatest advantage from this observation was that the effective radius was most easily obtained from minimal wheel excitation. Since R_e can greatly change the model's output response being able to estimate it quickly and easily is vital to a more accurate tire model performance.
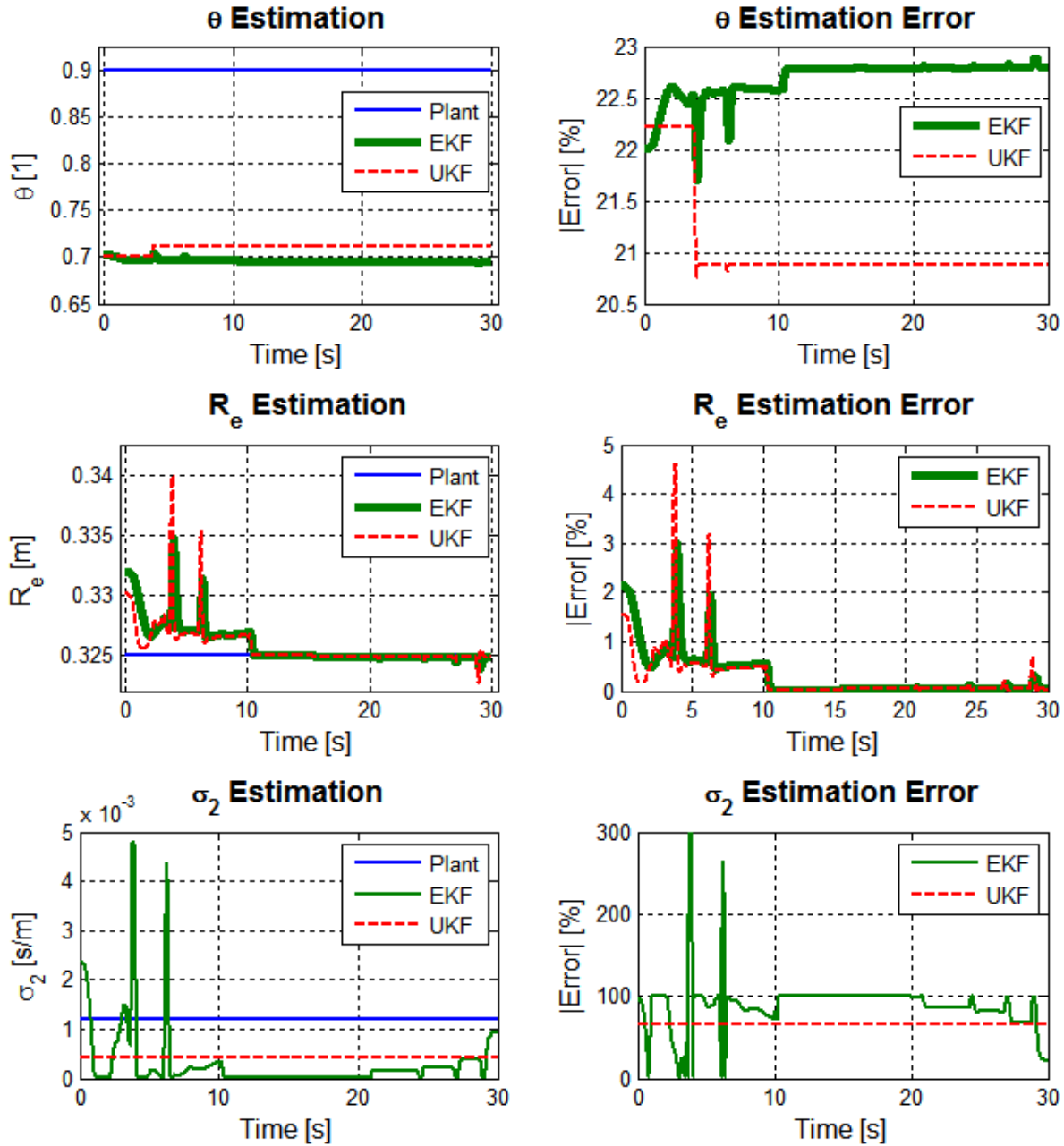
Figure 27: CarSim® Test 1: Acceleration and Brake - Parameter Estimation

Unfortunately, the EKF once again had significant fluctuations with the σ_2 parameter, all the while the UKF settled on a value that was partially between the initial condition and the plant parameter. This might lead one to suspect that the σ_2 parameter was difficult to observe with this estimation approach. In order to evaluate this possibility the estimation was performed without σ_2. The results from the reduced parameter estimation set can be examined by referring to Appendix A. Once again, the general outcome from the reduced set was essentially identical to that of the full estimation set previously described.

3.5.3 Results for CarSim® Test 2: Hard Braking with ABS Engaged

The final test case, the ABS enabled test with aggressive braking was intended to overcome the limitation observed in the previous maneuver. This test can be noted as being much more aggressive by visually examining the larger slip shown in Figure 28. The slip during this test is generally much larger in magnitude. Likewise, the slip contains significant variations as a result of the ABS system modulates the wheel brakes. An important consideration with regards to Figure 28 is that the slip has been bounded between ±1. The reason is that when the magnitude of $R_e\omega$ or V_x becomes exceedingly small the numerical calculations at low speeds produce slip data that is no longer meaningful. However, based on the performance of the estimator with the persistent excitation, one would expect that this test scenario would yield the most promising simulation results.

(A) Full Time Range   (B) - ABS Active Time Range
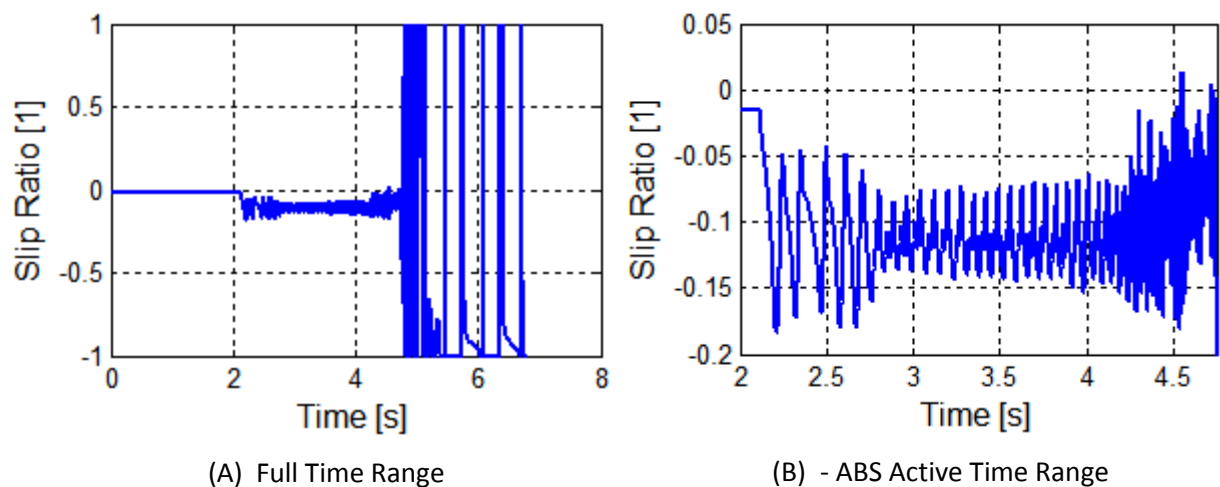
Figure 28: CarSim® Test 2: Hard Braking with ABS Engaged – Slip Information

Unfortunately, that was not the case. In fact, this maneuver provided the most unstable estimation particularly from the EKF. The EKF estimated the state to be repeatedly at the limit, all the while producing force that was well in excess of that experienced in simulation. Figure 29 and Figure 30 highlight how the EKF was not able to produce adequate results.
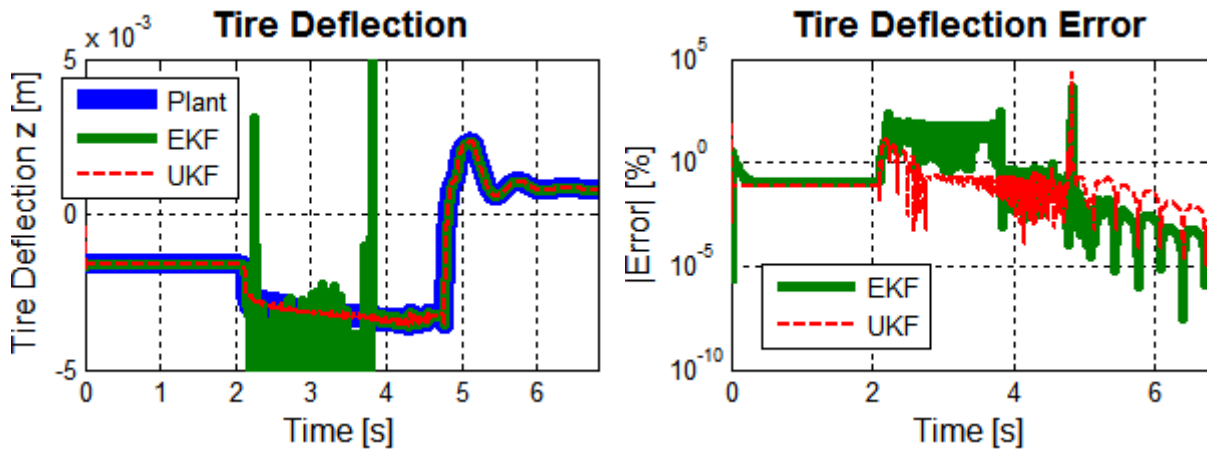
Figure 29: CarSim® Test 2: Hard Braking with ABS Engaged - Tire Deflection Estimation
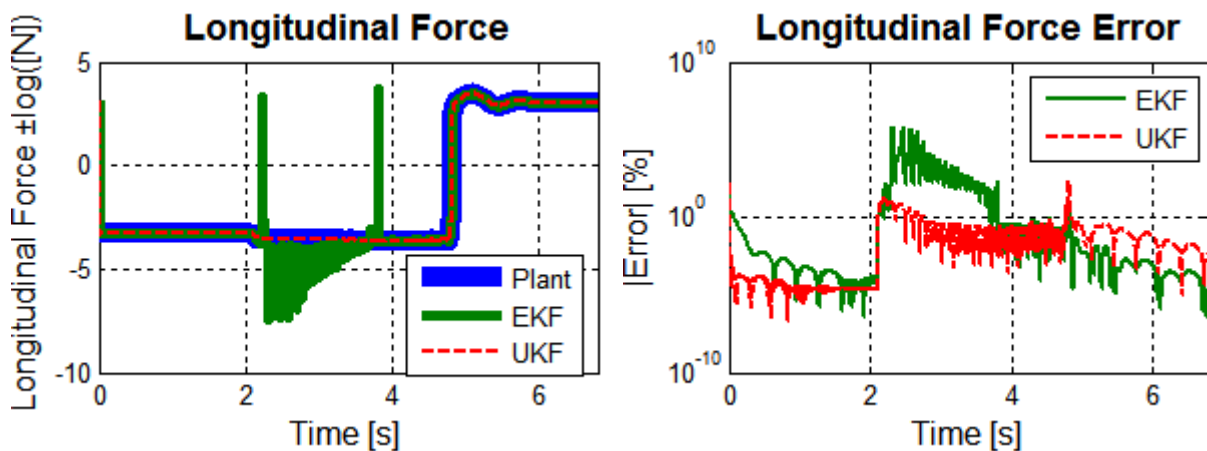
Figure 30: CarSim® Test 2: Hard Braking with ABS Engaged - Longitudinal Force Estimation

While it can be noted, that the UKF was able to perform better than the EKF based on the results shown in Figure 31, as the UKF's output resembled that of the plant's force response. The UKF estimation was able to produce these forces and state results accurately without correctly approximating the parameters throughout the entire process.
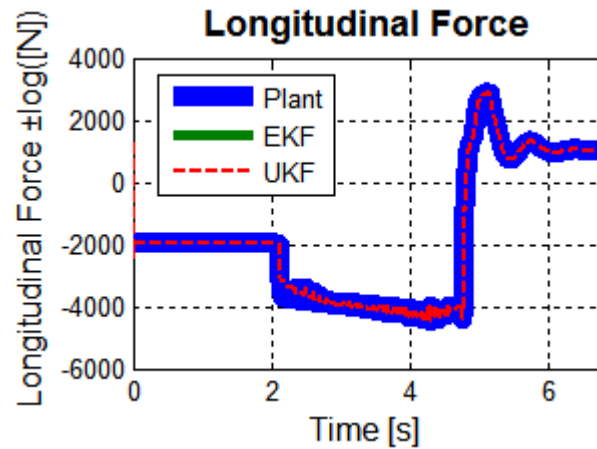
Figure 31: CarSim® Test 2: Hard Braking with ABS Engaged - Longitudinal Force Estimation UKF Estimate Only

Figure 32 shows how the most problematic term was R_e in this case as the estimated value in both methods showed the greatest fluctuation fortunately the error remained within 5%. Both estimation methods diverged with only the UKF being able to recover to an extent. The maneuver is also dominated with transient responses that make the estimation difficult, even with a reduced parameter estimation set as was shown with the examination included in Appendix A.
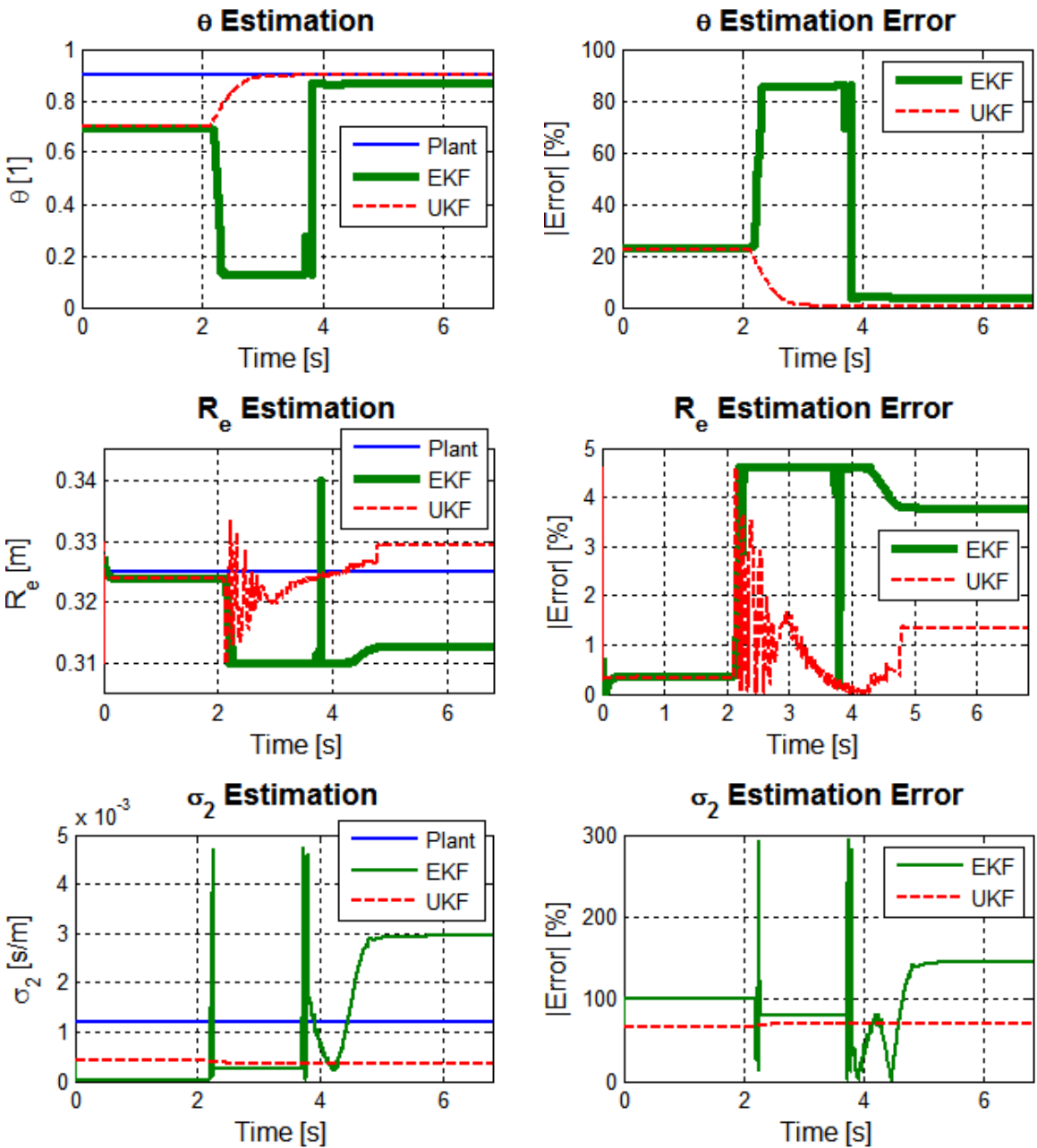
Figure 32: CarSim® Test 2: Hard Braking with ABS Engaged - Parameter Estimation

The high rate of fluctuation that excited the model within this test case might be too fast for the combined model and estimation to accurately account for the parameters using the linearized EKF approach.

3.5.4 Simulated Model Adaptive Response with Rich Signal Input

As a final consideration, the adaptability of the estimation techniques was considered. For this evaluation the persistent excitation test case was once again used to provide excitation to the system. The parameter list was then reduced to only R_{eff} and Θ, while still estimating the tire deflection state z. The results, as shown in Figure 33 and Figure 34, indicate that the UKF method is capable of determining the parameter values if provided sufficient excitation to do so. Additionally, the parameters have been selected to change after 12 seconds for R_{eff} and 14 seconds for Θ using a constant slop to the new values as shown in Figure 34.
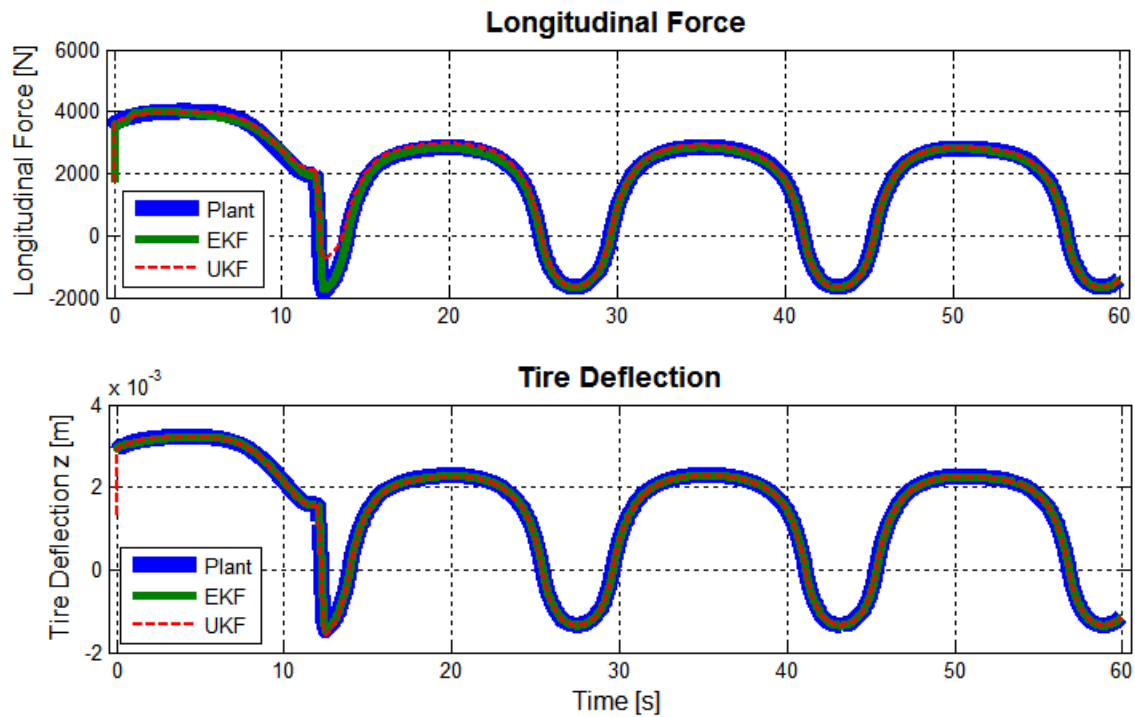
Figure 33: Tire Force and Deflection Estimation with Time Varied Parameters
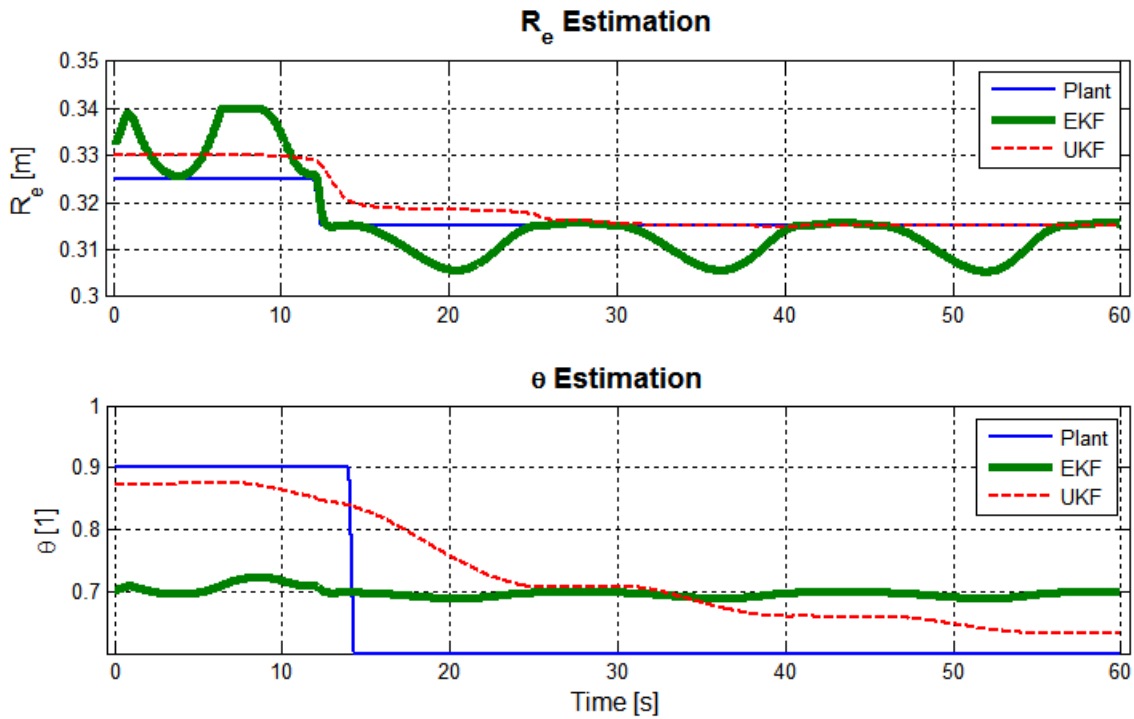
Figure 34: Tire Parameter Estimation with Time Varied Parameters

From the results, one can observe that the EKF approach provided oscillation continuously while the UKF was able to converge to the desired results, eventually. The approach presented Figure 34 has additionally applied adjustment to try and allow both methods a smoother convergence to the final result. This was done by slightly reducing the parameters estimated variance in the Kalman filters. However, this only provided noticeable improvements in the estimation with the UKF. It is worth noting that each method was able to accurately estimation both the state and force values throughout the entire estimation process. The estimated force and deflection accuracy did discrepancy around the transition time of the parameters. However, this discrepancy is to be expected.

3.6 Conclusion and Summary of Findings

Based on the results of the simulation investigation, the LuGre tire model has four main terms that would ideally be estimated using an online estimation approach. However, from the approaches examined, the parameters can prove to be difficult to obtain unless a persistent excitation is provided. The simulation process has also revealed that different excitation can permit different parameter estimation. The θ parameter proved to be difficult to observe unless a significant slip excitation was present to excite the model beyond the linear region. Furthermore, R_e was best observed in the opposite case with minimal slip data while nearly none of responses examined allowed σ_2 to be observed.

The possibility exist that a parallel estimation approach for the R_e and σ_2 parameters could be advantageous. This parallel approach would likely require some level of oversight to ensure that the excitation provided to the parameter identification is in a form that ensures the best performance. The possibility of a parallel estimation is physically supported by the nature of the parameters since R_e and σ_2 are connected to how the tire is shaped and the material itself. The advantage is that these parameters could be evaluated at a much slow estimation rate than the tire deflection or road classification. Provided that σ_2 can be estimated at all, the simulations performed suggest that σ_2 is prone to be unobservable.

Lastly, the LuGre model and concept has had significant development along with revisions by many researchers. This disjointed development lead to the extensive analysis that was performed to allow for greater confidence in the selection of the model structure chosen. The selected approach combines many authors' efforts and uses reasonable simplifications that enable the tire model parameters to be estimated, as is discussed in the subsequent chapter. This same approach and insight was also used to extend the model in the lateral direction, this too is explained in further detail below.

Chapter 4
Experimentation

4.1 Introduction

Contained within this chapter is the real-world implementation of the method simulated previously. By utilizing the insights from the simulation process, the tire model and estimator were applied to a fully instrumented vehicle. This vehicle provided additional sensor data collection that is not found on production vehicles and thus allows for significant research insights. Furthermore, this chapter will discuss the experimental processes and examine the tire model's performance with the UKF estimator and changes required to operate with real-world data.

4.1.1 Experimental Research Vehicle Description

Thanks to GM's kind contribution, the University of Waterloo research group was able to use a fully instrumented Cadillac STS® test vehicle. The most notable sensor set found on this research vehicle was the wheel hub sensors. These wheel hub sensors allowed for high speed real-time access to the forces and moments exerted on each wheel. The second sensor system that is unique to this research vehicle was the inertial measurement data with global positioning information. The sensor was a six axis IMU with GPS that provided position, velocities, accelerations, and rotation rates. Figure 35, shows the vehicle that was used and highlights the specialized sensors. The specialized sensor data was collected along with the production vehicle sensors (such as, the wheel rotation rates and the steering wheel angle) system. All of the signals and information about the vehicle were communicated using a CAN-bus that was a part of the normal vehicle messaging system. A dSPACE® MicroAutobox® was installed to provide real-time data logging of these messages and access to the information about the vehicle systems. The particular vehicle was configured for observation only as the production systems that operated the vehicle allowed for the drive operations to function normally.
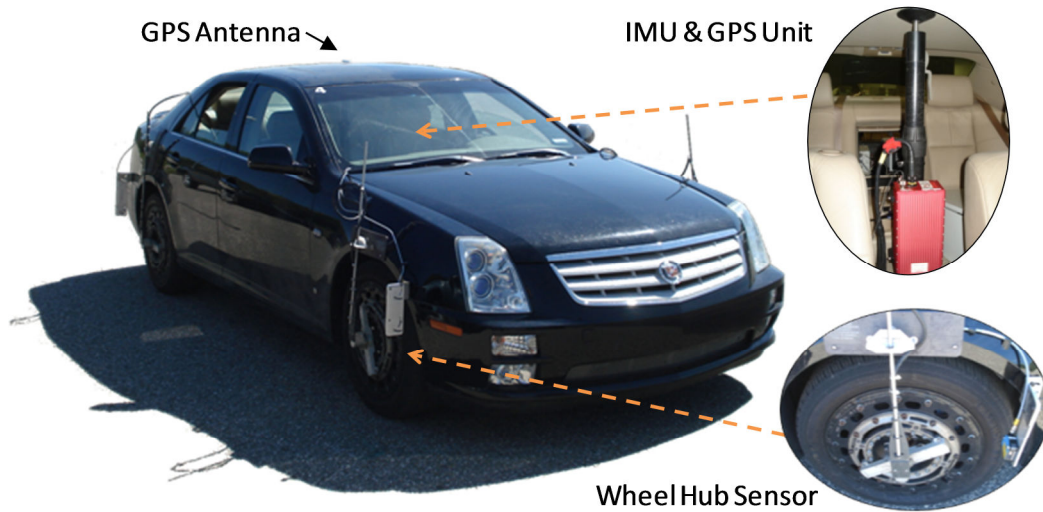
Figure 35: Cadillac STS Fully Instrumented Research Vehicle

In order to work with the research vehicle, several baseline parameters were required. These included: the location of the center of mass, the wheel base length, the front and rear track widths, the steering ratio (the hand wheel angle to the tire road angle), and inertial estimates for the wheels and sprung mass. Using a combination of information provided by GM though documentation, CarSim® models, and measurements taken in the lab, the vehicle's general parameters were identified.

4.1.2 Data Collection

Once the information from the wheel hub sensors is obtained, the data needs to be processed and converted into a form that is viable for comparing force information. Figure 36 shows the progress of the processed signal information. The information obtained from the sensor is "…applied by the spindle to the tire per positive SAE coordinate directions…" [29].
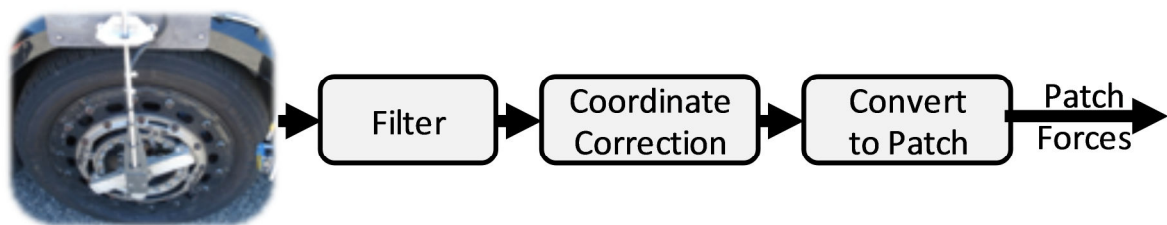
Figure 36: Wheel Hub Force and Moment Transducer to Tire Patch Forces

This results in the forces and moments being measured in a different location than the desired contact patch location. Consequently, the information is transferred from the measured point, O, to the desired point, P, as shown in the wheel's right side, provided in Figure 37.
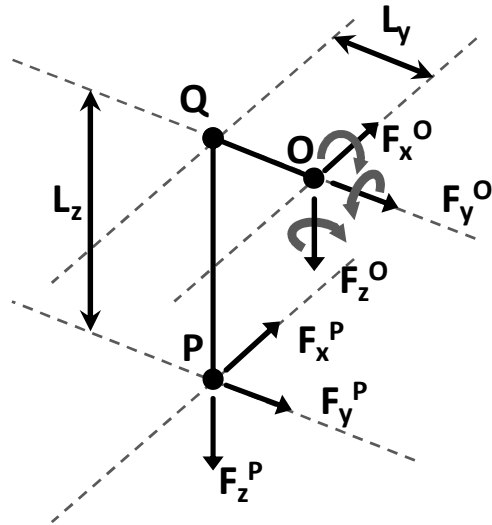
Figure 37: Wheel Hub Sensor Data Transfer to Contact Point

Additionally, the velocity data from all four individual wheel centers is required as input for the tire model. In order to accommodate this, the planar model kinematic relation is used with the assumption that the wheel centers are reasonably fixed relative to the sprung mass. Figure 38 illustrates the planar model and the velocity data of interest. This approach was possible since the vehicle testing assumed that the road surface was flat and that the effect of the suspension travel had minimal impact on the wheel's velocity calculations. Furthermore, the wheel angle had to be accounted for as the velocity information desired is based on the tire's frame of reference, not the vehicle's frame of reference.
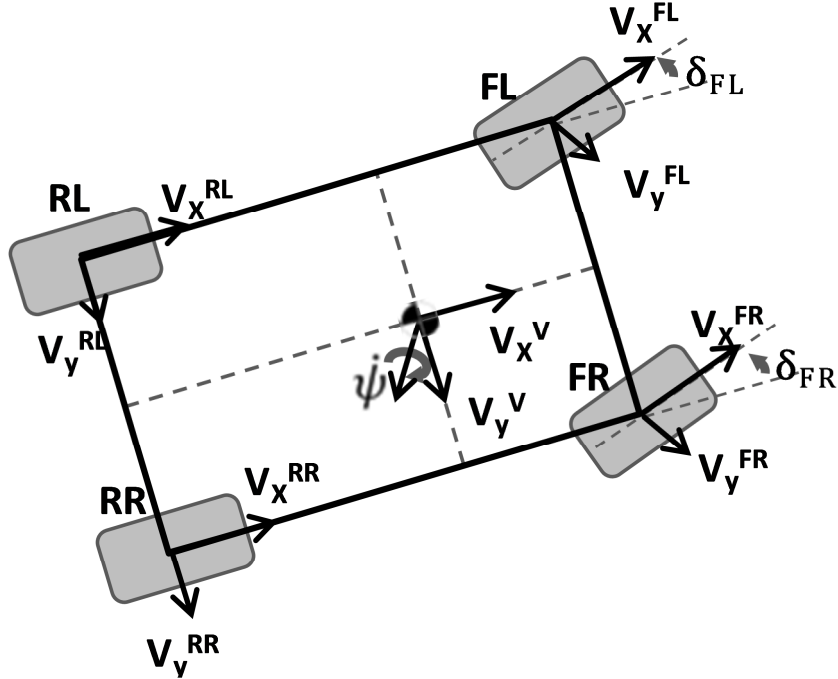
Figure 38: Vehicle and Wheel Velocity Relation, Planar Kinematic Model

Lastly, the wheel rotation rates were available in two forms: firstly, from the production sensor's data and secondly, from the load wheel hub sensors. Hence, the required list of signal information that the tire model estimation needed is realized.

4.2 Vehicle Testing Setup and Initial Configurations

To begin, the tire modeling is first considered with the longitudinal vehicle motion over a relatively flat road surface. The model was adjusted to match the physical response of the real tires as measured by the instrumented vehicle. The initial parameter values were based on the steady-state parameters that fit with the tire data provided for the vehicle. The steady-state parameter matching was performed using the nonlinear least squares function again, as described in Chapter 3. The results provided a starting point for the experimental data collected against parameter matching. Lastly, the vehicle speed selected to match the steady-state tire data was 50km/hr, while using the tire constants $\gamma = 2$, and $\kappa_i = \frac{7}{6}\frac{1}{L_i}$ as before.

4.2.1 Implementation Technique and Kalman Filter

The UKF approach was utilized in a Joint-UKF estimation approach, such that the tire states z_i were estimated; while simultaneously estimating the Θ parameter that described the tire's performance by accounting for variations in road conditions. The remaining parameters were assumed to have minimal time variation from the values approximated by prior offline estimation. One exception was the effective radius; this value was adjusted slightly based on the vertical loading characteristics of the wheel. By assuming a linear spring model and adjusting for large variation in the vertical forces, during cases such as hard braking, the effective radius was calculated at each time step using:

$$R_e(t) = R_e^N + \frac{(|F_z^N| - |F_z(t)|)}{K_z}, \quad where \quad R_e(t) \in [R_e^{min}, R_e^{max}] \tag{4.1}$$

Equation (4.1) uses the free rolling effective radius and the related vertical load as the nominal terms, R_e^N and F_z^N, respectively. The remaining vertical load $F_z(t)$ is the instantaneous vertical load on the tire. Lastly, the term K_z is the tire linear spring stiffness that allows the radius to vary based on the vertical load between the limits defined by R_e^{min} and R_e^{max}, as the measured loaded and unloaded tire radii, respectively. Figure 39, shows the parameter matched response that compares the relation between the measured and estimated tire longitudinal forces obtained during a straight line acceleration then brake to stop maneuver.
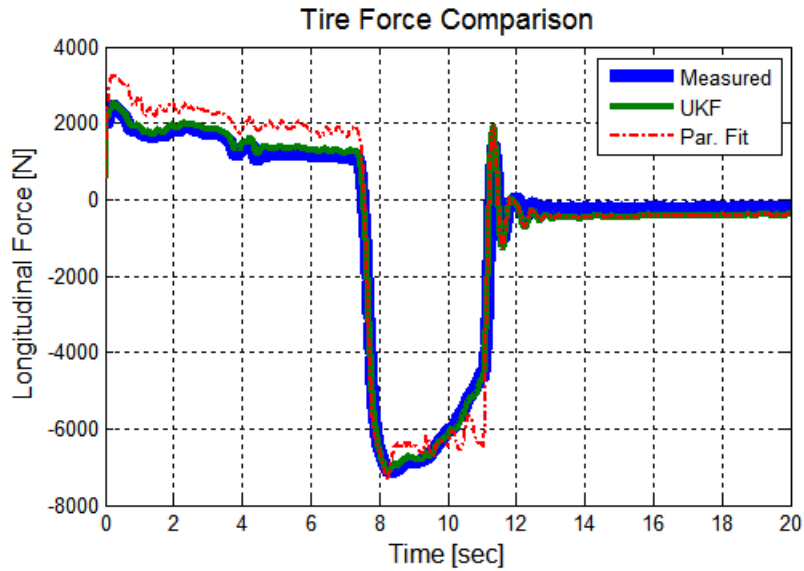
Figure 39: Experimental Longitudinal Force Estimation

Figure 39, is the longitudinal force from the front left wheel measured and estimated using the tire model. The response shown has three data sets, the first being the patch force as measured by the vehicle instrumentation. The second is the UKF estimated value using the LuGre tire model estimation with the UKF adjusting the tire state and parameter θ. Meanwhile, the other utilized parameters were obtained from the parameters found by the LuGre parameter fit response, Par. Fit. This data employed an adaptive Kalman gain such that the UKF was enabled to adjust the state when the velocity was below 0.3m/sec. The remainder of the data was obtained by allowing the tire model to produce an open loop estimation that was fit using a nonlinear least squares method. The purpose of implementing the adaptive UKF based on the velocity is to enable the LuGre model to provide a smooth state transition into and out of the normal operating range of the tire. This is required due to the fact that the velocity noise becomes an issue at very low velocities and the LuGre model becomes highly inaccurate when the relative velocity, V_r, is calculated predominantly with noise. Figure 40, has been provided to observe the velocity profile of the experiment run during the results presented in Figure 39.
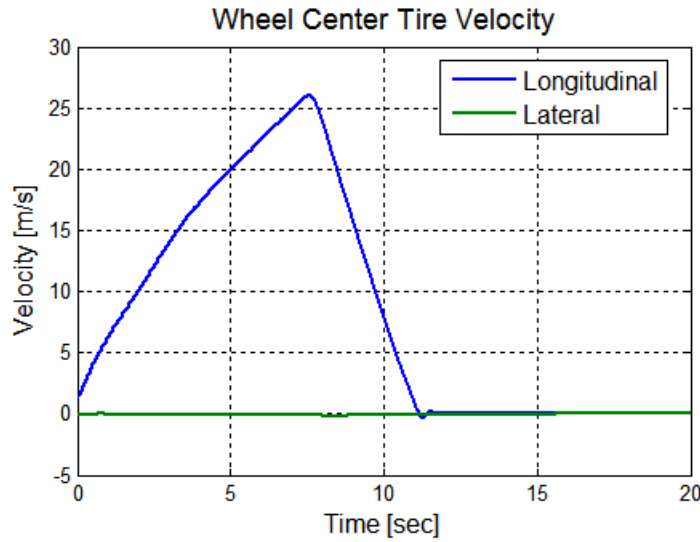
Figure 40: Wheel Center Velocity

4.2.2 Parameter Identification

The process of identifying the parameters was an iterative one and made use of insights from the simulation test cases. Initially, the parameters selected were defined by using the curve fitting method with the steady-state model obtained from the CarSim® tire model in much the same way as described in Chapter 3. The first estimated parameter was the effective radius, which was based on the approach noted by the simulations. This was possible by using a test scenario that experienced very minimal slip and was in the linear region of the expected tire response behaviour; as close to the free rolling motion as possible. The nonlinear least squares function was reutilized to obtained the effective radius for each tire with the described scenario. The same algorithm was later used to improve estimates of σ_0, σ_1 and μ_s during acceleration and braking manoeuvres similar to that shown in Figure 39 previously. Lastly, considering the higher slip test cases allowed for the adjustment of the V_s, μ_k, and σ_2 parameters, as they are more associated with the response beyond the steady-state peak value. The parameter estimation and verification was repeated for each of the tires. The parameters were then refined using a combination of the nonlinear least squares estimator and the UKF with an adaptive law. Figure 41, provides the general structure with the adaptive UKF estimator that is encapsulated by the least squares parameter identification.

58
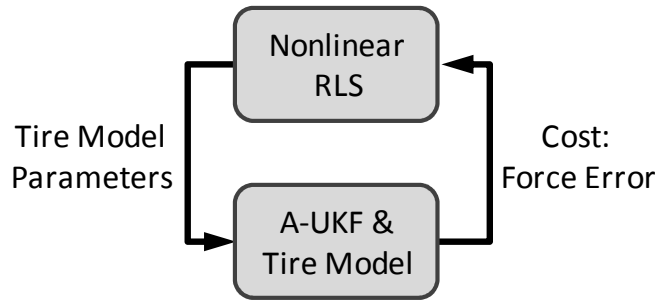
Figure 41: Dynamic Tire Model Parameter Tuning

This allowed the UKF to provide excellent tracking with the tire state at lower velocities, ensuring better lead-in conditions when compared to the tire response estimated without the use of the Kalman gain. This approach was used instead of the nonlinear curve fitting discussed by Canudas-de-Wit, [7], who used steady-state estimation. The tire had often resulted in highly transient characteristics while braking leading to rapid changes in the tire deflection. Hence, the dynamic from of the tire model was used instead.

4.2.3 Longitudinal Test Results

The tire models, with the estimation of the terms z and θ as a function of time, provided the force response as shown within the testing results in Figure 42 to Figure 45. The testing condition was a straight-line acceleration and braking maneuver that was performed. Figure 43, indicates the force comparison between the measured patch forces and the estimated tire forces. The estimated force data was accompanied by the capacity estimation for the individual tires and normalized as shown in Figure 45. The capacity estimation was performed by determining the peak steady-state friction response of the tire models with the estimated parameters, including the time updated θ parameter and the tire's normal force. The steady-state capacity limit was able to provide a reasonable approximation that can enable the information to be used in conjunction with control strategies for friction capacity.

Figure 42: Path Traveled During Longitudinal Test with Google® Satellite Image [30]

Figure 43, contains the measured and estimated longitudinal tire friction forces exerted between the vehicle and the ground. The four graphs are presented such that the upper two are the front tires and the lower two the rear. Similarly, the left and right graphs correspond to the left and right side of the vehicle from the driver's perspective. This is the standard layout that will be used here onward when presenting the four tires.

The UKF based estimated process was able to reproduce the results quite well for the entire time. Some inaccuracies observed are at the very end of the test when the velocity and forces are close to zero. This low velocity region is often a problematic condition for the tire model as this kinematics that define the relative velocity used in the model become noises since the sensors are not able to accurately provide vehicle speed and wheel rotation data close to a stopped vehicle state.
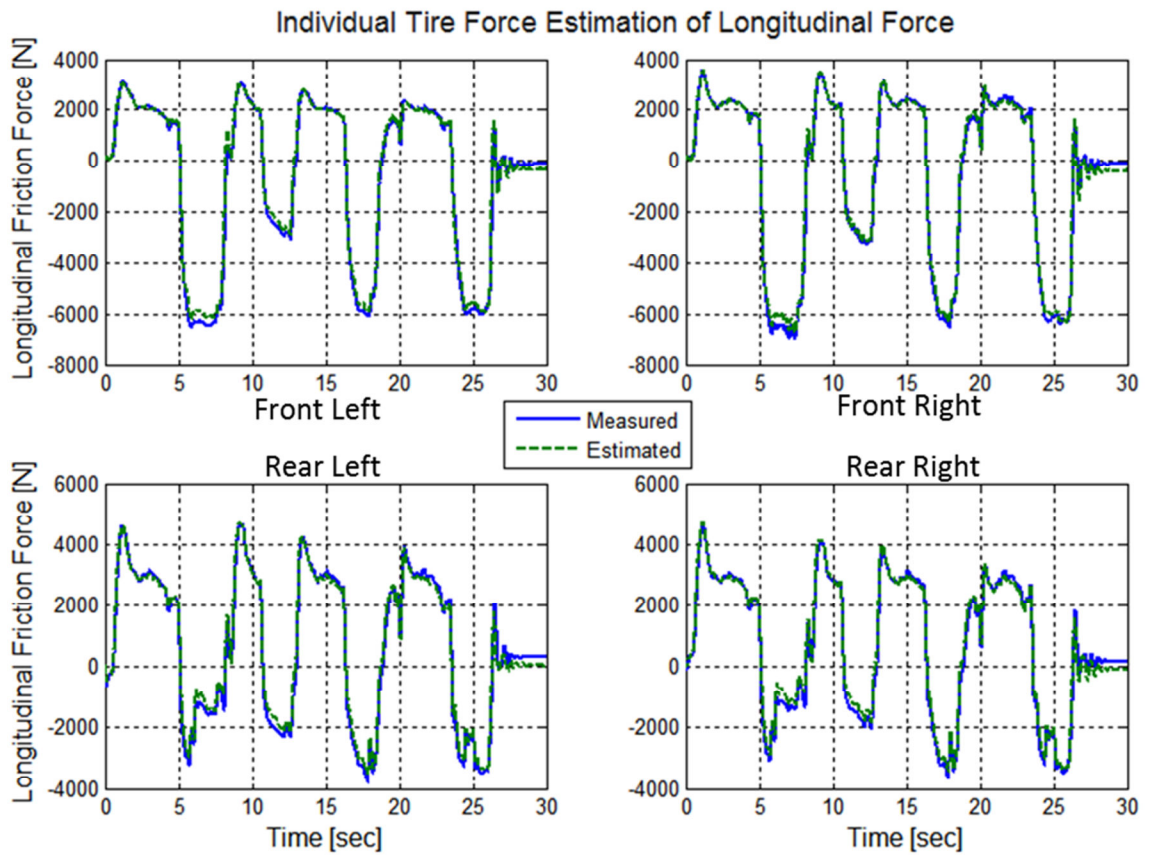
Figure 43: Four Wheel Longitudinal Force

The aggressive braking performed during the experiment caused excessive vertical load transfer. This can be observed in Figure 44. The importance of this is that the large pitching motion and vertical load change in the tires causes significant radius changes. As a result the tire model needs to be considered with the linear spring compensation that is proportional to the vertical tire load.
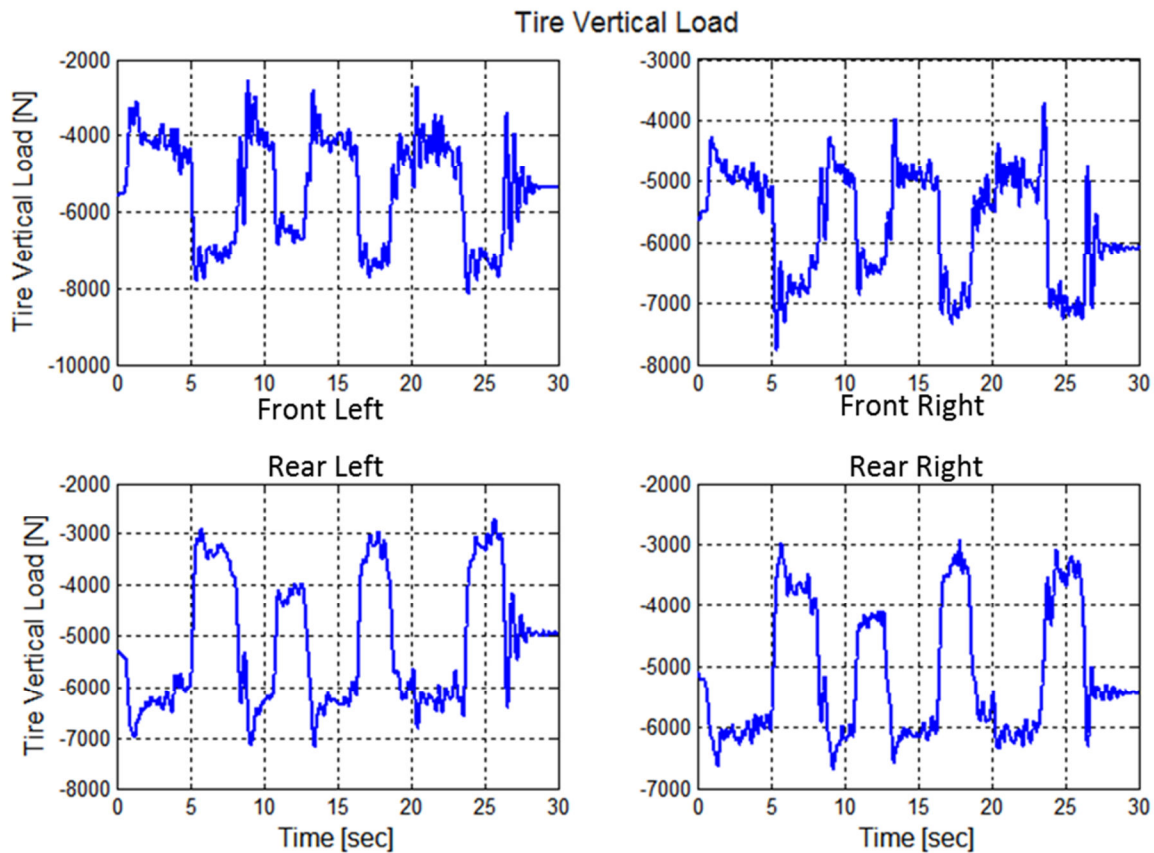
Figure 44: Four Wheel Vertical Tire Load

Lastly, the tire capacity information that is based on the normalized tire forces has been provided in Figure 45. The measured normalized data was obtained by dividing the instantaneous longitudinal force by the corresponding instantaneous vertical force for each tire. The normalized comparison allows the capacity estimation to be made without the consideration of the vertical tire load. As a result, the capacity estimates are calculated without the consideration of the loading that is affected by the maneuver being performed. This enables a more stable and consistent capacity limited as showing in Figure 45 as the green and red lines. The capacity has been estimated with the steady-state longitudinal parameters fit for the tires, and using the tire varying instantaneous estimate of Θ.

Figure 45, has been provided to show the tire capacity data. The figure shows that the capacity data reasonably represent what the expected performance was as the vehicle was braking nearly at the limits that the dry road surface would allow. Additionally, the forces response contains sharp spikes

62

that approach and exceeded the estimated capacity limit. This indicated that the tire was not able to sustain levels of braking force in excess of the steady-state capacity estimated. This would suggest that the tire capacity estimated was reasonable accurate.
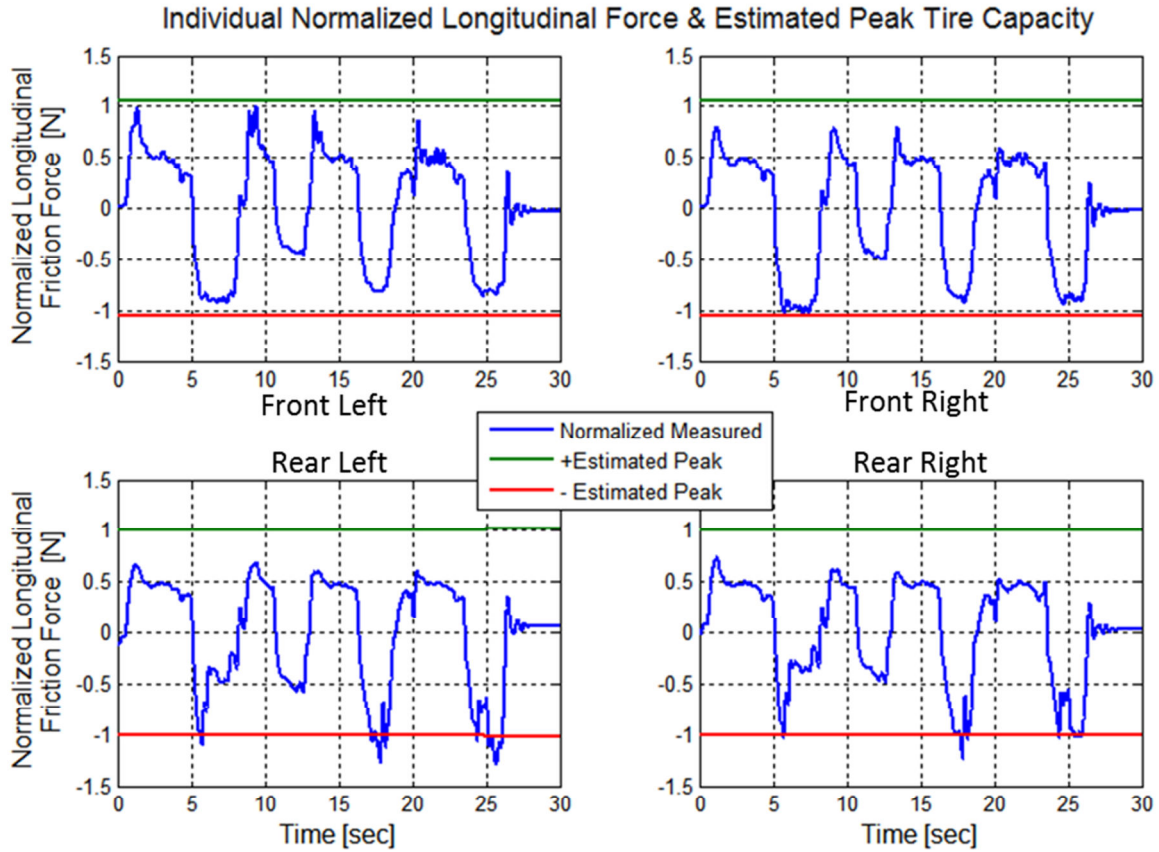
Figure 45: Four Wheel Normalized Longitudinal Friction Force and Tire Capacity Estimation

The longitudinal estimation approach had provided reasonable force estimation based on parameters found in previous testing. Additionally, it has provided a means to estimate the capacity limits of the tire friction force. The condition is best considered by having the effective radius estimate augmented with the vertical load, especially when there is significant variation in the tire vertical load. Based on the results from the tire model and the UKF approach provided, an extension to include the lateral direction is the next logical step.

4.3 2D Average Lumped LuGre Friction Model

The two dimensional Average Lumped LuGre Friction Model is a continuation of the ideas developed in the one dimensional version. Here, the orthogonal components F_x and F_y forces are captured both in the longitudinal and lateral directions, respectively. However, there is a coupling component between the two directions and the elliptical constraint can be included as developed in [10] by Velenis et al. This constraint can also be observed in the development described by Pacejka in [3]. Utilizing the approach described in the works of [10] and [11], along with the concepts previously described, the following approach can be used. Refer to (4.2) to (4.5) for the general model that has been extended to include the lateral direction.

The two dimensional average Lumped LuGre Tire Friction model equations are:

$$
\begin{bmatrix} \dot{z}_x \\ \dot{z}_y \end{bmatrix} = \begin{bmatrix} V_{rx} \\ V_{ry} \end{bmatrix} - \left(\frac{\left\| M_k^2 \vec{V}_r \right\|}{\theta g(\vec{V}_r)} \begin{bmatrix} \dfrac{\sigma_{ox}}{\mu_{kx}^2} & 0 \\ 0 & \dfrac{\sigma_{oy}}{\mu_{ky}^2} \end{bmatrix} + |\omega| R_e \begin{bmatrix} \kappa_x & 0 \\ 0 & \kappa_y \end{bmatrix} \right) \begin{bmatrix} z_x \\ z_y \end{bmatrix}
\tag{4.2}
$$

$$
g(\vec{V}_r) = \frac{\left\| M_k^2 \vec{V}_r \right\|}{\left\| M_k \vec{V}_r \right\|} + \left(\frac{\left\| M_s^2 \vec{V}_r \right\|}{\left\| M_s \vec{V}_r \right\|} - \frac{\left\| M_k^2 \vec{V}_r \right\|}{\left\| M_k \vec{V}_r \right\|} \right) e^{-\left(\frac{\| \vec{V}_r \|}{V_s} \right)^\gamma}
\tag{4.3}
$$

$$
\begin{bmatrix} \mu_x \\ \mu_y \end{bmatrix} = - \begin{bmatrix} \sigma_{0x} & 0 \\ 0 & \sigma_{0y} \end{bmatrix} \begin{bmatrix} z_x \\ z_y \end{bmatrix} - \begin{bmatrix} \sigma_{1x} & 0 \\ 0 & \sigma_{1y} \end{bmatrix} \begin{bmatrix} \dot{z}_x \\ \dot{z}_y \end{bmatrix} - \begin{bmatrix} \sigma_{2x} & 0 \\ 0 & \sigma_{2y} \end{bmatrix} \begin{bmatrix} V_{rx} \\ V_{ry} \end{bmatrix}
\tag{4.4}
$$

$$
\begin{bmatrix} F_x \\ F_y \end{bmatrix} = F_n \begin{bmatrix} \mu_x \\ \mu_y \end{bmatrix}
\tag{4.5}
$$

Effectively, the results from equations (4.2) to (4.5) describe two independent states that are governed by the friction ellipse behavior as constrained in equation (4.2) and (4.3). These independent states are to be tracked as the tire experiences excitation and the results dictate the final performance of the model. Figure 46 provides a viewable interpretation of the two tire states and how they can be perceived as the average material deflection. That being, the average material deflection for the particular tire at the contact patch. The diagram shows how the lumped material can be

64

considered with the x and y components that comprise the lumped estimated tire state (Z_x and Z_y deflection).
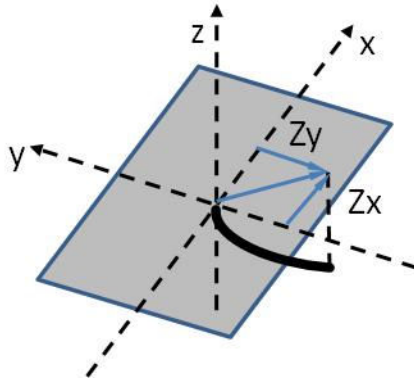
Figure 46: 2D Average Lumped LuGre State Diagram Encompassing Combined Deflection

The ground condition, as previously described, is applied to both directions simultaneously in the two dimensional model. Meanwhile, each direction's state can be independently determined. The result is two distinct equations that are only linked with the internal friction coefficient terms, where one can observe the relation that defines the elliptical connection contained within the two dimensional extension of the LuGre model. From the described model approach, the coupling that comes from the elliptical limitation is implemented by using non-dimensional parameters, μ_s and μ_k. Figure 47 provides a visual understanding of the elliptical assumption with the parameters based on the diagram shown in [11].
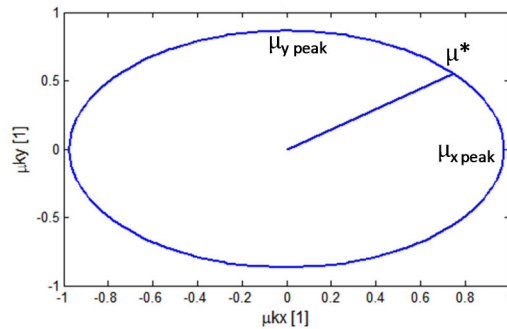
Figure 47: Friction Ellipse Concept Integrated in 2D LuGre Model

65

Further consideration with the two dimensional plainer motion of the vehicle requires the inclusion of correcting for a wheel that is no longer in line with the velocity of the wheel nor the direction of the vehicle body axis. As a result Figure 48, and equations (4.6) (4.7) have been provide to illustrate the relation between the vehicle sprung mass velocity, the wheel angle with respect to the sprung mass, and accounting for the relative velocity similar to the previous relative velocity.
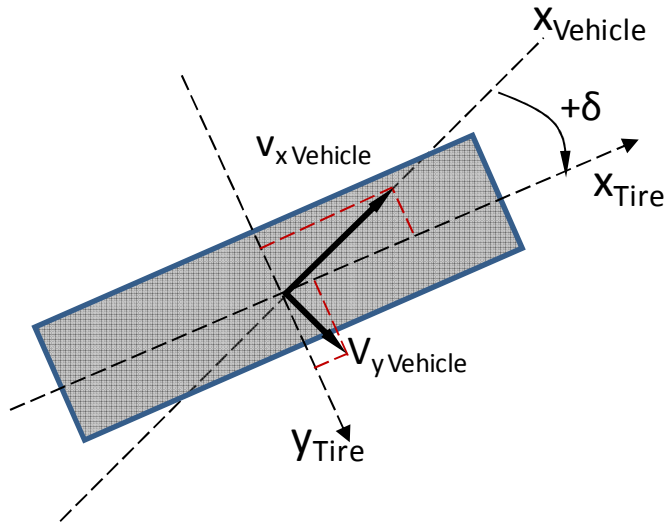
Figure 48: Relating Vehicle Frame Velocity at Wheel Center to Tire Frame

$$v_{rx} = \omega R_e - (v_x \cos \delta + v_y \sin \delta) \tag{4.6}$$

$$v_{ry} = v_x \sin \delta - v_y \cos \delta \tag{4.7}$$

At this point, the relation between the hand-wheel angle and the tire angle becomes important and is obtained though documentation provided by GM. The individual wheel angle, δ, is required per wheel. To acquire δ, the wheel toe angle and the angle resulting from the driver's steering wheel, need to be combined.

4.4 Implementation with 2D LuGre Tire Model and UKF

The lateral parameter identification was performed in the same manner as the longitudinal parameter set. Initially, the parameters were curve fit using steady-state data as previously described. This was further refined using the lateral excitation from the experimental results. The lateral testing was

executed in such a way as to minimize the amount of longitudinal force changes, seeing as this would introduce coupling effects that would then increase the difficulty of lateral parameter identification. This was accomplished by performing experiments at near constant velocity.

After the lateral parameters had been determined, the purposed two-dimensional estimation was then applied to two test cases presented within using the joint UKF method to estimate the two direction states and the road condition parameter. The first case was a double lane change where the vehicle abruptly moves from the current lane to an adjacent lane and back. The vehicle path can be seen in Figure 49. The second case was a braking in a turn maneuver where the vehicle applies the brakes while performing a turning maneuver. The vehicle path for this maneuver can be observed in Figure 55. In both cases, the vehicle has been driven to nearly the maximum limit that the maneuver can be accomplished. The purpose of such an aggressive experiment was to present the limits of the estimation and what the vehicle is capable of performing.

4.4.1 Lateral Test Results Double Lane Change

The results of the maneuver and the related estimations can be observed in the experimental results shown in Figure 49 to Figure 54. These results show the tire model estimation performance during a double lane change maneuver on a flat, dry road surface. Figure 49, shows how the vehicle approach and exited relatively straight and how the path veered from one lane to another and back again. The speed was maintained between 48 and 50 km/hr during the double lane change maneuver.

Figure 49: Double Lane Change Path Driven with Google® Satellite Image [30]

The first set of in plot information is the longitudinal tire force estimation. The four wheels where able to estimate the longitudinal force generally quite well. The exception, being when the vertical load on the front tires varied significantly, the estimation deviated for the front tires. The force estimated by the tire model with UKF is in both each case was smaller than the measured value. This can be seen within Figure 50 at 10 seconds for the front left tire and at 8 and 12 seconds for the front right tire.
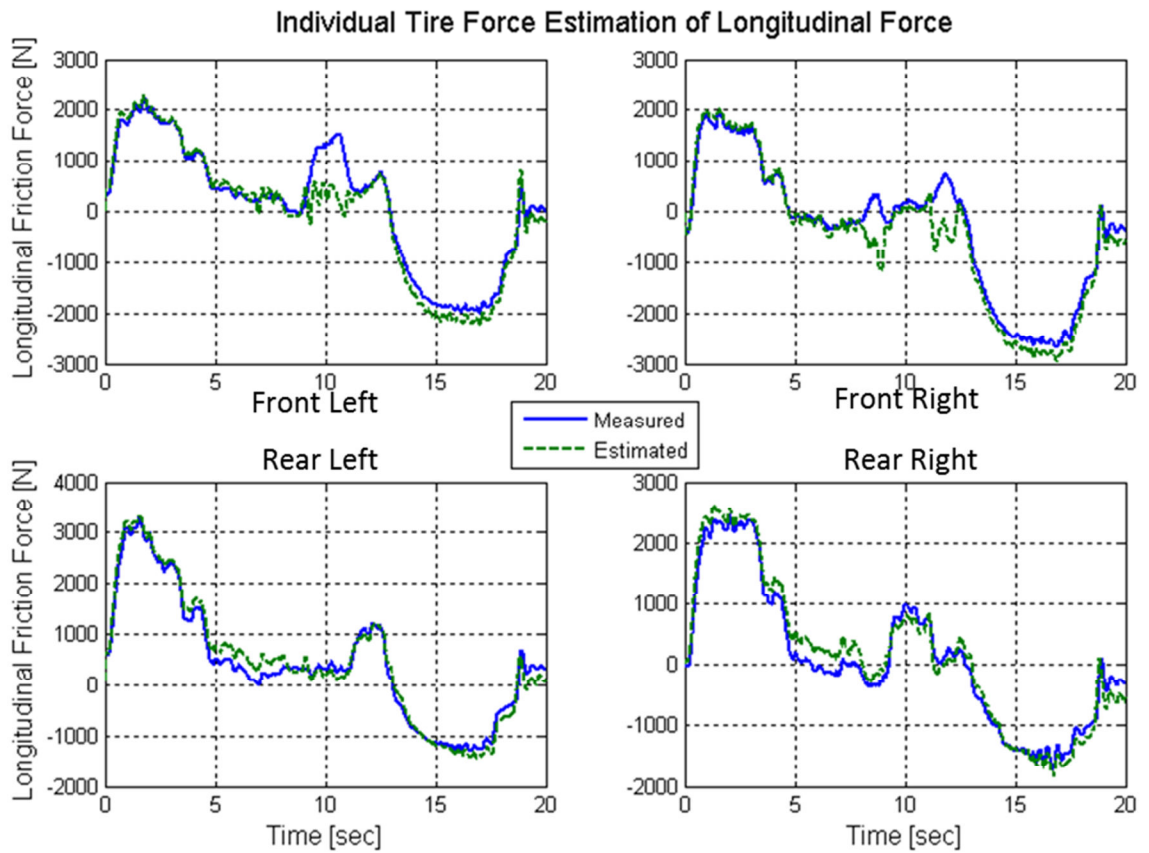
Figure 50: Double Lane Change Longitudinal Tire Forces

Figure 51 has been provided to illustrate how high the vertical tire forces became for the front tires. During the times that the tire models decreased in longitudinal accuracy, the tires experienced a vertical load in excess of 8000 N momentarily. This significantly high loading would have resulted in deforming the tire physically more than was has been accounted for by a linear relationship that is linearized around the operation vertical load of 5500N as corrected for by the effective radiuses.

69
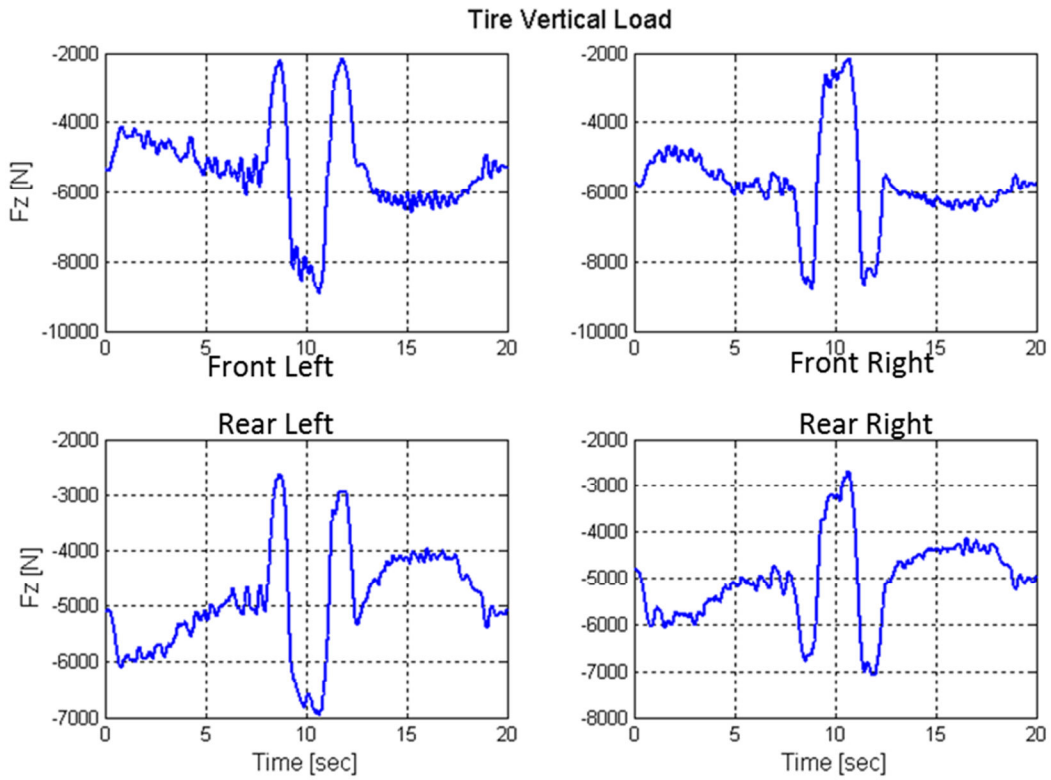
Figure 51: Double Lane Change Vertical Tire Forces

Nonetheless, the tire capacity has been provided once again for the longitudinal direction. The results shown Figure 52 are not surprising as the longitudinal force was minimally changed during this maneuver. As a result the longitudinal load was well within the estimated capacity limits.
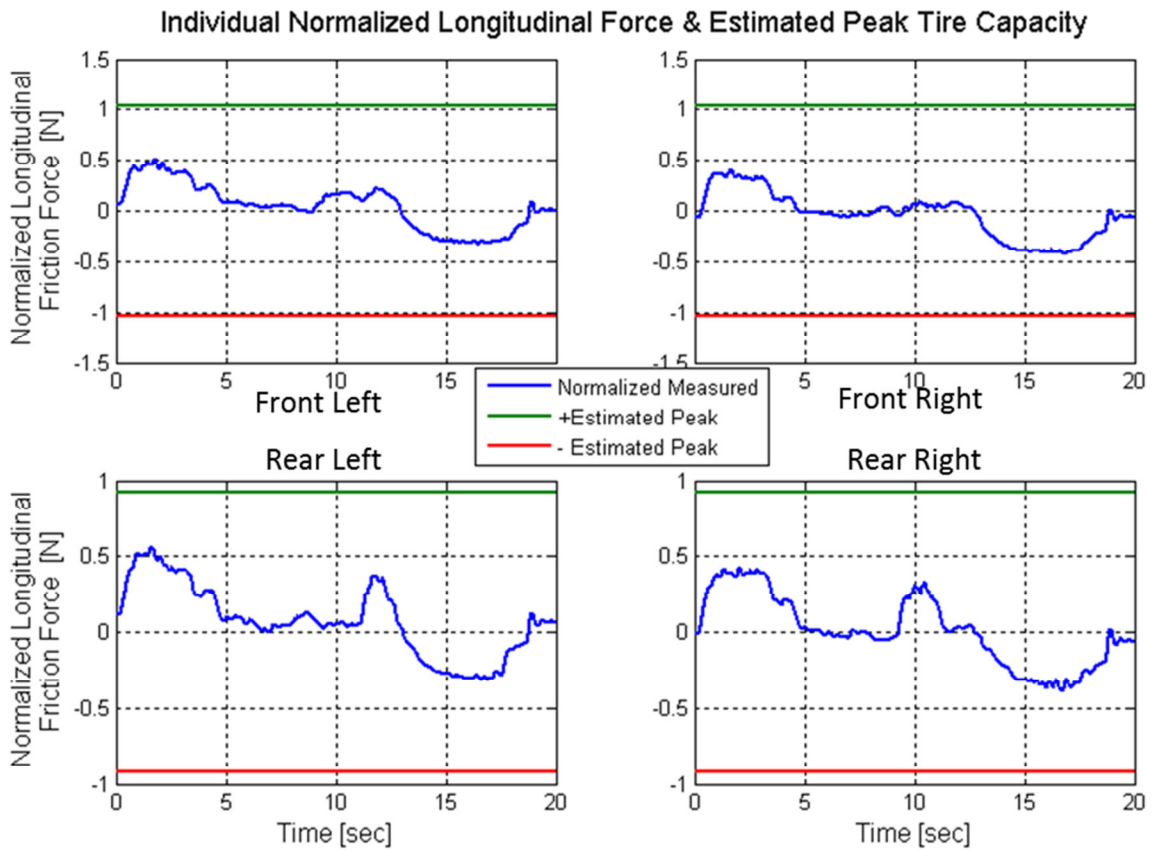
Figure 52: Double Lane Change Normalized Longitudinal Forces and Tire Capacity Estimation

The next sets of figures pertain to the lateral force information and estimations. Figure 53, contains the lateral estimation of the forces during the double lane change maneuver. The general trend has excellent agreement with all of the tires. The exception being that the rear tires slightly over estimate the peak friction load by not significantly.
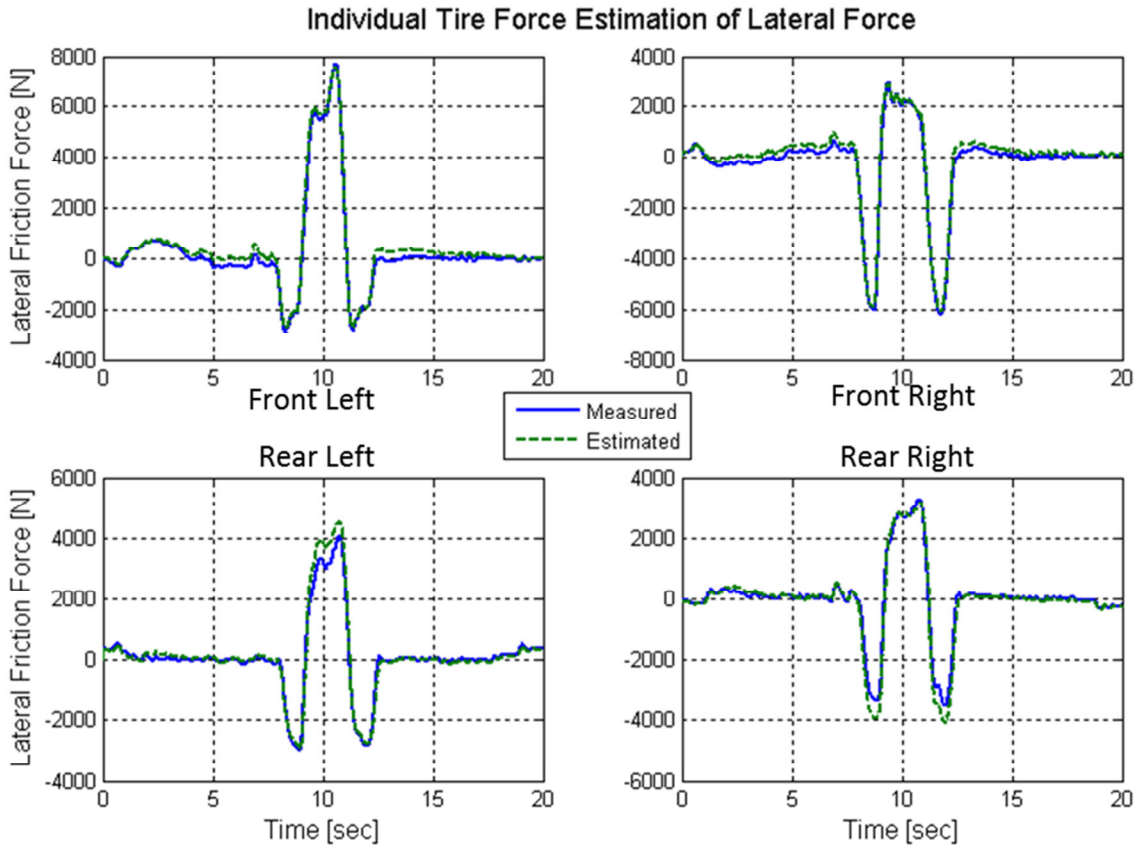
Figure 53: Double Lane Change Lateral Force Estimation

Lastly, the lateral tire capacity information has been estimated for each of the tires. Since the maneuver was performed at such an aggressive level the capacity limited estimated had indicated that the lateral forces the tires can provided have been fully utilized. And just as was seen with the longitudinal force before, the lateral force peaks at the expected capacity limit of the tire since the maneuver is performed as aggressive as possible. This would suggest that the vehicle could not perform the maneuver much more aggressively if one tried. The tire capacity can be seen to be momentary exceeded. However, this is likely due to the highly transient behavior of the tire at the time. And when compared with the steady-state capacity estimate, the momentary excessive load is quite reasonable to expect.
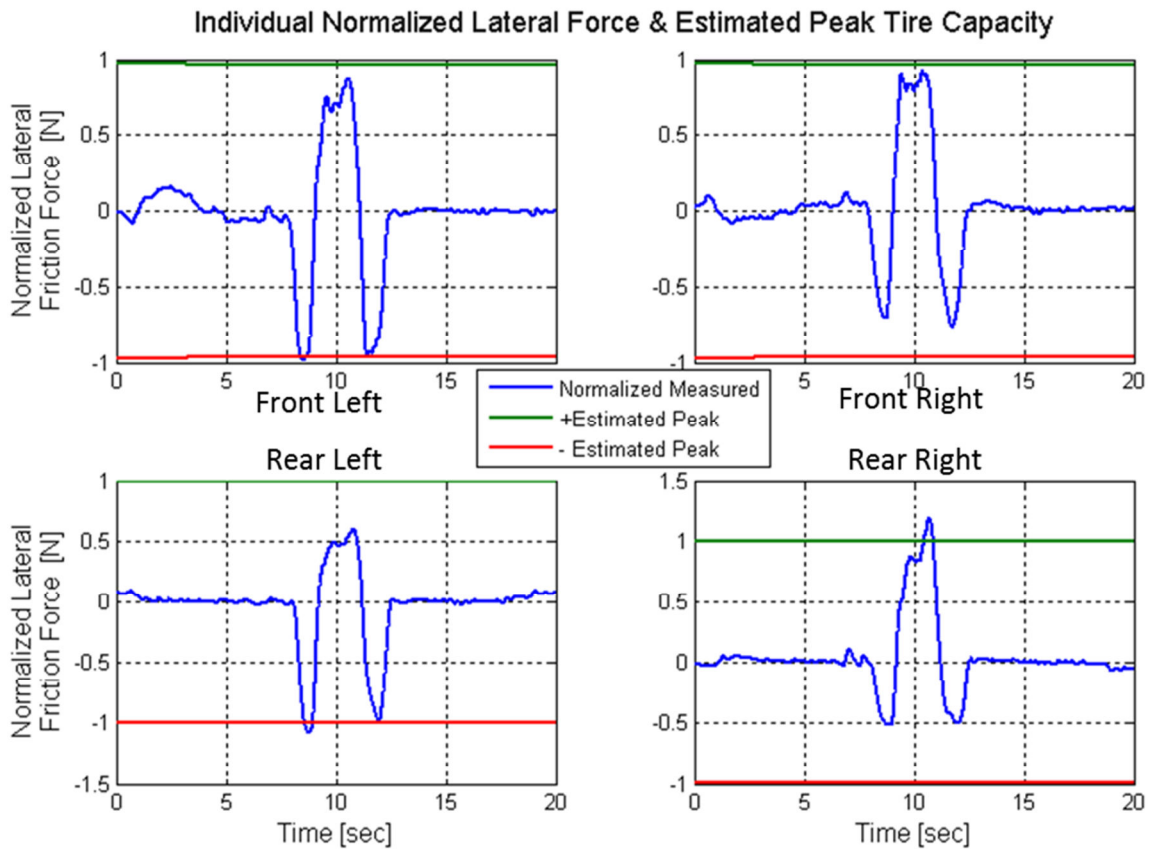
Figure 54: Double Lane Change Normalized Lateral and Estimated Tire Capacity

The double lane change maneuver with aggressive driving characteristics has been estimated reasonably well by the tire model using the UKF and force feedback. The two-directional approach has been able to provide reasonable estimations for both directions simultaneously and the capacity estimations that were based on the steady-state estimates of the tire performance, were logical and reasonably agree with the limits that the tire has been performing with.

4.4.2 Lateral Test Results Braking in a Turn

The following experimental case was performed with the combined estimation in a braking in a turn test case for the tire model. This test scenario will help illustrate the limitation of the model approach and why the assumptions applied affect the capabilities of the tire model. Figure 55, has been provided to visualize the path taken during the experiment.

Figure 55: Braking in a Turn, Path Driven with Google® Satellite Image [30]

The velocity profile information has been provided within Figure 56, where the longitudinal velocity decrease from 15m/s to a full stop in less than 8 second meanwhile, the vehicle experienced a significant change in trajectory. Lastly, the lateral velocity, of the vehicle's center of mass experienced approximately 0.6 m/s during the braking phase of the maneuver.
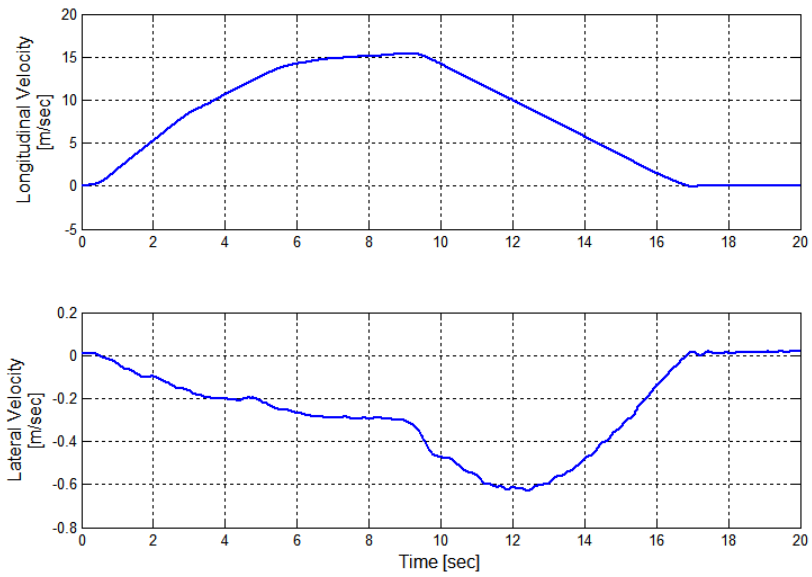
Figure 56: Braking in a Turn, Longitudinal Velocity Profile

During this maneuver the vehicle experienced significant body motion that resulted in large variation in the normal load distribution to the four wheels. Figure 57, shows how the front right wheel was loaded the most significantly with a vertical load reaching 9000N for a brief moment in time. While in contrast the rear left wheel had a very significant decrease in vertical load nearly reduced to 2000N.
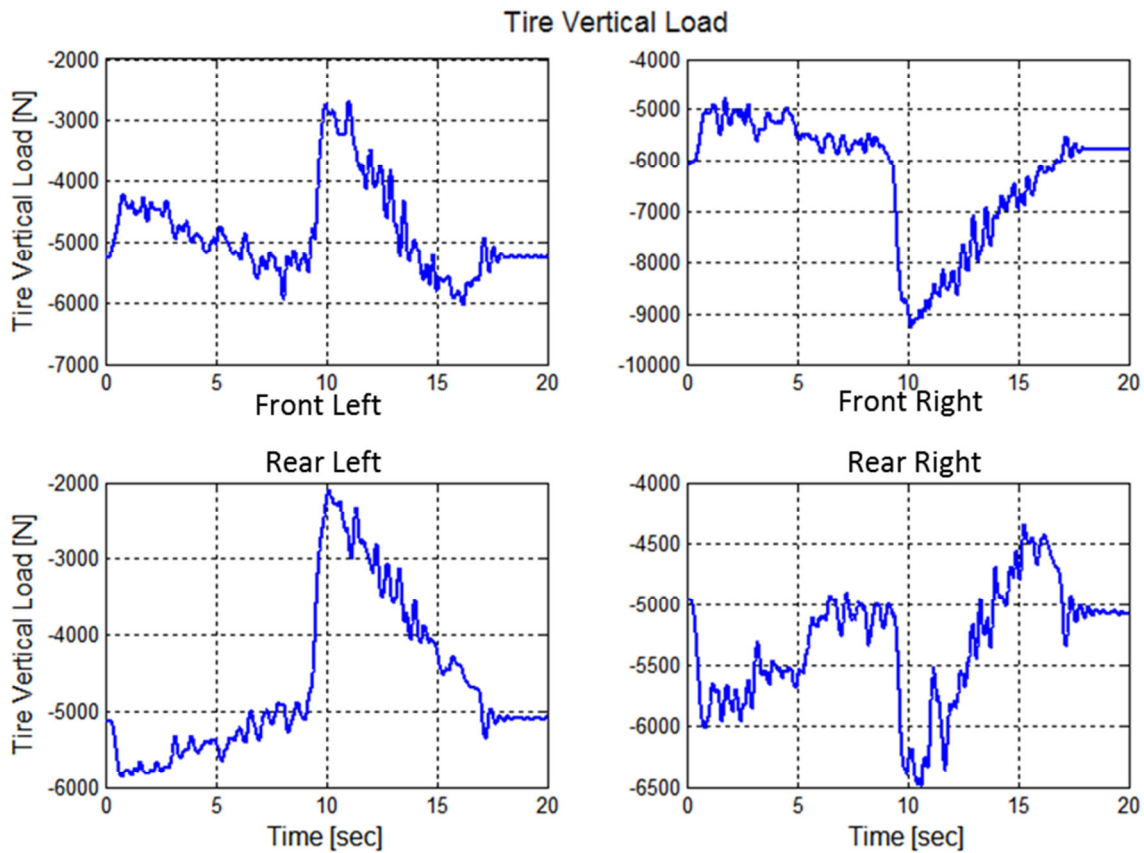
Figure 57: Braking in a Turn Vertical Tire Forces

Based on the experimental results previously discussed, the conditions that experience significant vertical load changes have shown that the tire model approach provided the least accurate results. One would expect that the two tires noted would undergo lease favorable estimation performance. While in contrast, the other two tires are likely to produce reasonable estimation results. However, for the longitudinal direction, as shown in Figure 58, the two left side wheels produce the most accurate estimation results. While, the front right wheel, was estimated with noticeably incorrect results during the extreme loading, as expected. Nevertheless, the rear right tire was unfortunately inaccurate during the braking phase of the maneuver.
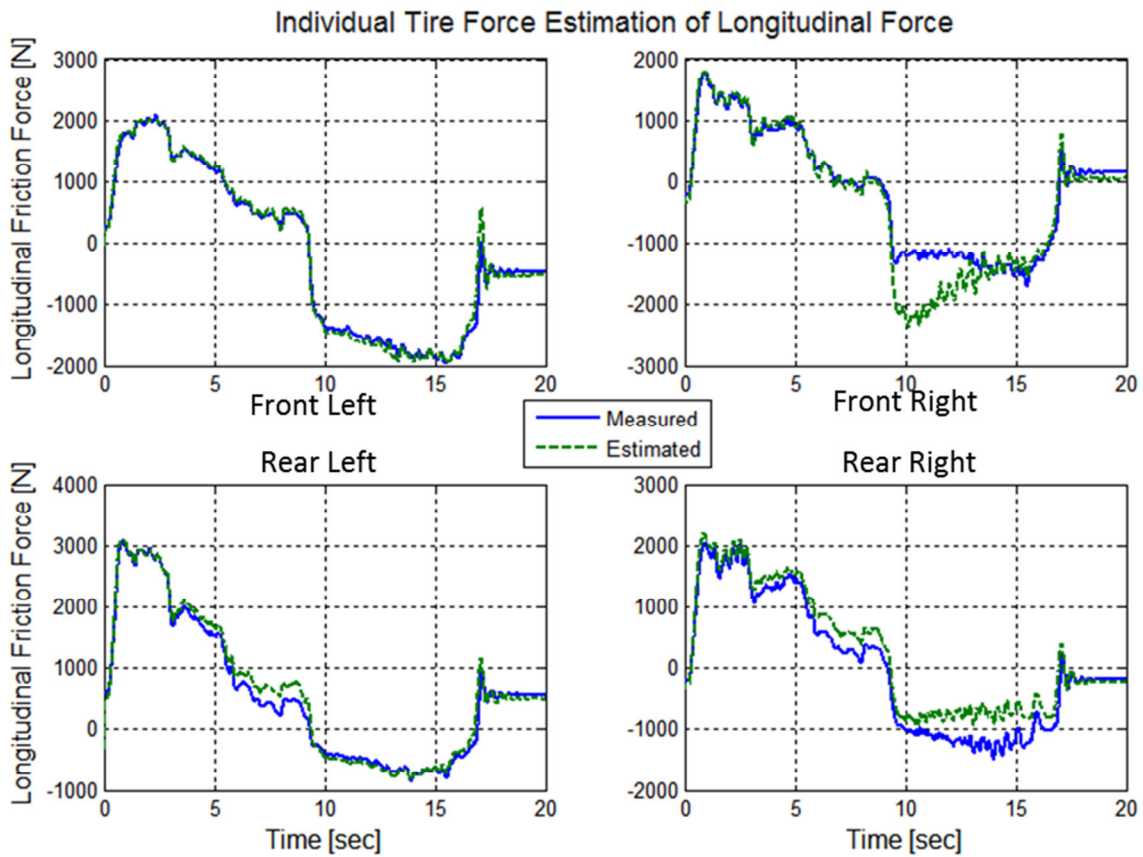
Figure 58: Braking in a Turn Longitudinal Friction Force

The capacity estimation for each of the tire's longitudinal characteristics suggested that the tire model had more stopping performance available. This can be seen in Figure 59, as the peak values marginally reach 50% of the capabilities expected from the tire. This would suggest that the estimation issue for the rear right tire is something other than the longitudinal tire limits being reached.
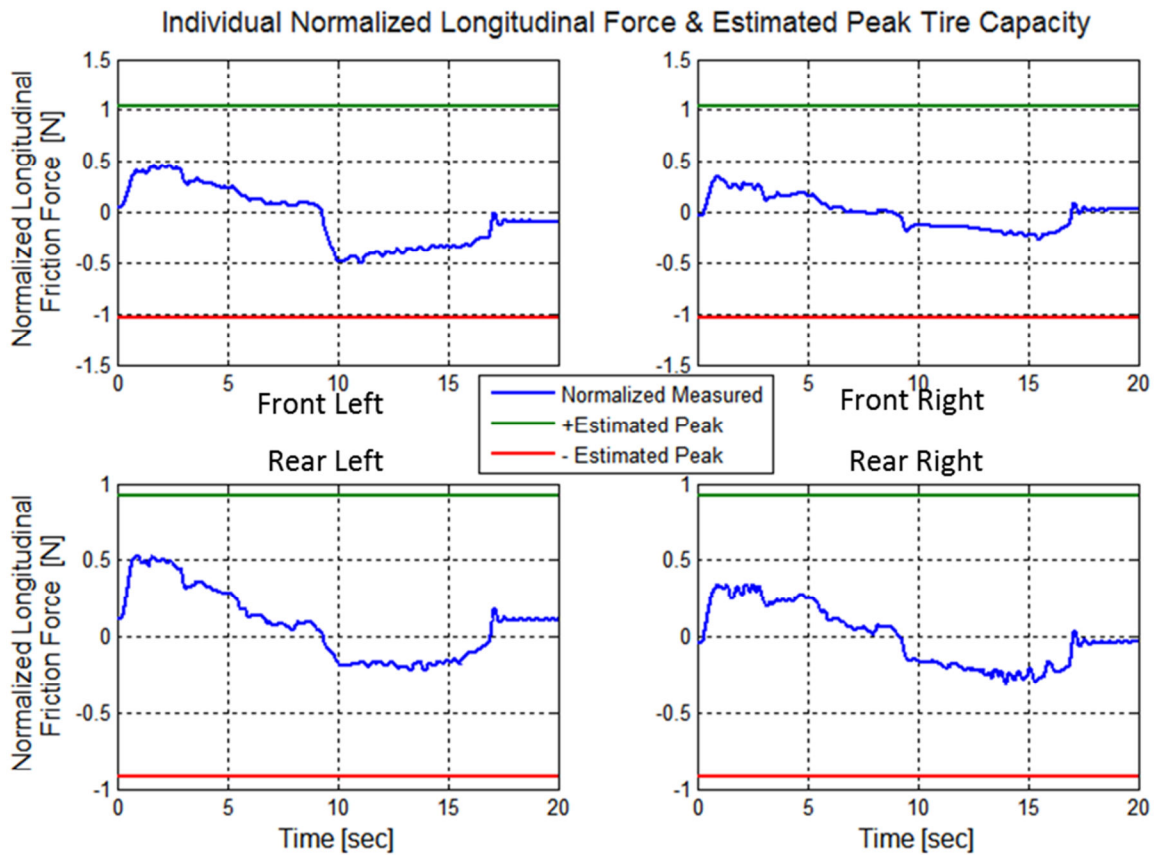
Figure 59: Braking in a Turn Normalized Longitudinal Forces and Tire Capacity Estimation

Continuing with the analysis, the lateral force estimation has been provided within Figure 60. The figure illustrates that the rear tires are not estimated as accurately as possible, since the forces are slightly over estimated during the maneuver. In contrast, the lateral forces for the front tires appear to be quite accurate.
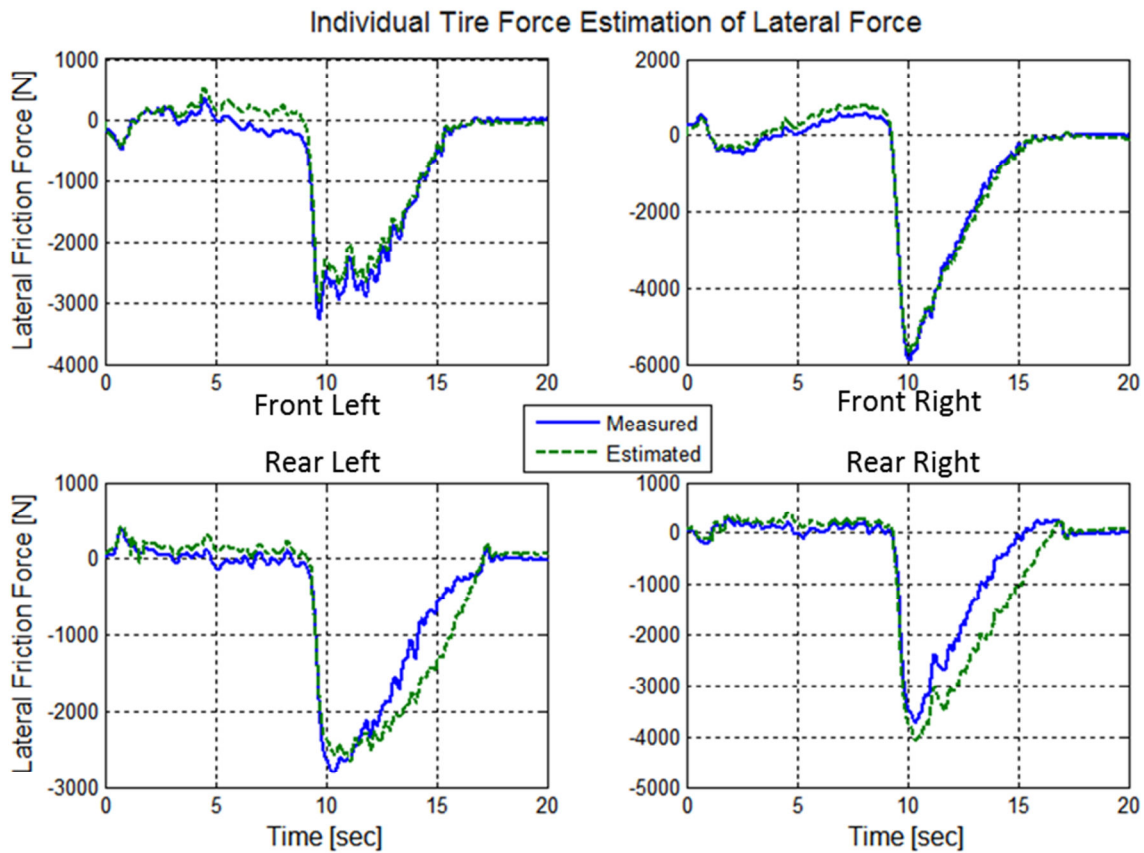
Figure 60: Braking in a Turn Lateral Force Estimation

At this point the estimation has only been able to properly account for the front left tire during this maneuver. This can be reasonably understood by the fact that several factors have influenced the tire force load characteristics. Firstly, the very extreme load transfer has forced the tire radius along with the physical shape of the tire out of the normal operating conditions expected with the assumed model approach. Secondly, the vehicle suspension had contributed significantly to how the tire and sprung mass exert forces on one another. Since, the suspension and tire camber angles are not accounted for within this model the information has been omitted and the tire model cannot account for this error. Instead, the UKF has tried to do so by adjusting the state of the tire, however, this has its limits and as theses estimation condition are exceeded the approach accuracy decreases. However, the estimated result is not entire incorrect, and the general trend has been retained. This would suggest that, if one had additional model information, than this difficult maneuver could be estimated more accurately.

79

Finally, Figure 61 provides the final component to consider with this maneuver. As the tire load in the rear left becomes exceedingly low, the capacity for this tire decreases. As a result, the estimated limit for the tire has remained at the normalized value, but the vertical load has decreased so significantly that the normalized force exceeds the expected range of the tire. Furthermore, the opposite is visibly true with the front right tire. As the vertical load increased so significantly, that even with the large lateral load on the tire, the normalized value barely exceeded half the calculated capacity. Meanwhile, the remaining two tires have capacity estimation, as would be expected, with the conditions of the vertical load change previously described for the tires. Here both tires provide comparable lateral load, however, the rear right has noticeably more vertical load to assist in the capacity of the tire.
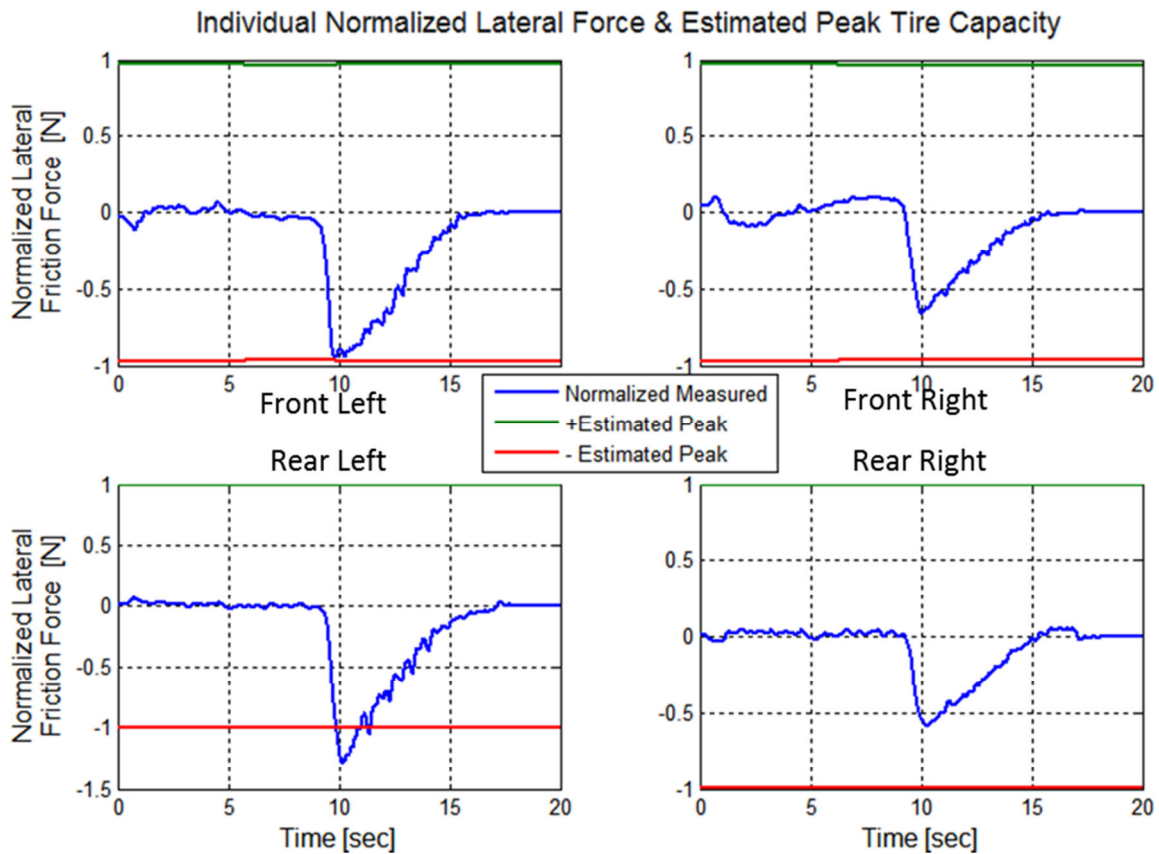
Figure 61: Braking in a Turn Normalized Lateral Forces and Tire Capacity Estimation

4.5 Conclusion

The tire model approach was able to provide reasonably accurate results for each of the test cases considered. The application of the UKF to simultaneously estimate the states and parameters of the LuGre tire model was able to work successfully on a function full scale test vehicle. The results were then passed into a steady-state estimate of the tire models for both the longitudinal and lateral directions to obtain capacity estimates. The tire model's steady-state response was exploited to resolve the estimated peak capacity values that were provided in the estimates presented.

However, this approach is limited to the level of accuracy due to assumptions made, such as the exclusion of the camber angle and its effect on tire performance and the limits of large vertical load change. Fortunately, the model has shown a level of robustness against these effects based on the flat road surface test cases. This may not be the case when allowing for banked road conditions test cases. Considering that the scope of this investigation does not include such an extensive set of road scenarios, one can conclude that the results thus far have been favorable and merit further development.

Chapter 5
Full Estimation Experimentation

5.1 Introduction

The major limitation of the experimental work done hence far is that the information required is obtained by using costly wheel hub sensors, making this approach unreasonable to apply to current mass market vehicles. However, by estimating the forces instead of measuring them, one could apply the entire process without the costly instrumentation. To that end, the next discussion will examine the combined efforts of the Full Vehicle Estimation (FVE) that estimates wheel forces provided by Reza Zarringhalam and Ayyoub Rezaeeian as part of a combined vehicle research investigation. Their approach provides force information that replicates the necessary inputs normally acquired from the wheel hub sensors. Importantly, the FVE does not utilize a tire model and allows the feedback to be used to adjust the LuGre model approach in just the same way that has been used hence far. Additionally, the FVE approach currently only accounts for the observable transient/vehicle excitation that affects the forces during maneuvers, and has limited observation of road bank or gradient angles. However, this is highly desirable as a feedback signal for the LuGre model as the nature of the force information provided by the model tire model currently has the same limitations.
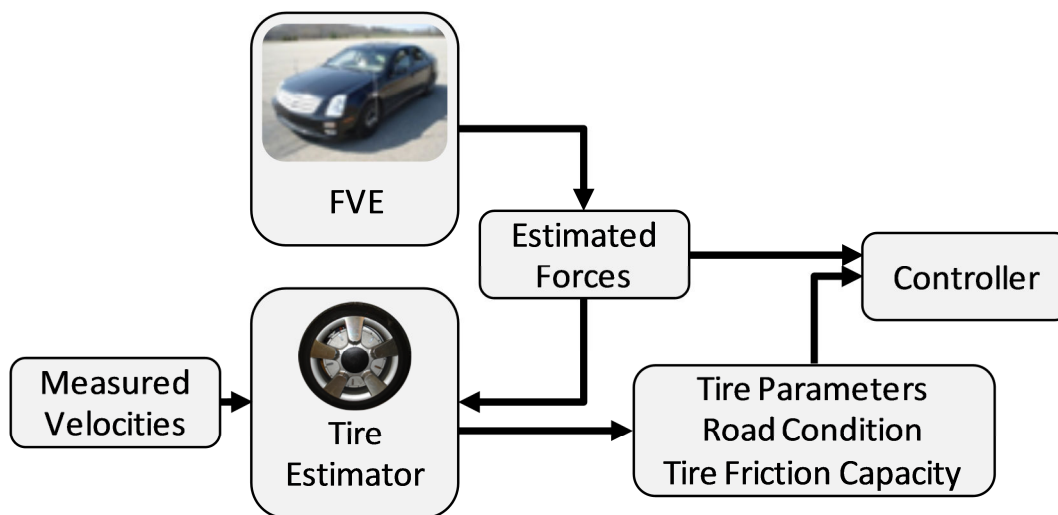
Figure 62: Tire Estimator Using Full Vehicle Estimation for Force Data

For the purposes of the results discussed the FVE was configured to only provide force data to the tire estimation technique. As shown in Figure 62. Part of the future work will be to include the velocity information provided by the FVE. This would enable the complete vehicle estimation using the FVE in conjunction with the adaptive tire model as the full estimation technique.

5.2 Full Estimation with Instrumented Vehicle

Continuing to use the instrumented vehicle, the tire model was next provided with force information that was obtained by the FVE. The force data was once again accompanied by the rest of the production sensors, along with the velocity from the IMU plus GPS unit, in the same manner as previously implemented.

The noticeable advantage of performing the experiments with the FVE is that the force data can be estimated without the vehicle lateral loading due to suspension design and road bank angle. All of the results provided next were performed with the tire model utilizing the FVE force estimation data.

5.2.1 Evaluation and Findings Acceleration and Brake Test

The first test case to consider with the fully estimated approach is an acceleration and braking maneuver. Much like the test previously performed with the wheel-hub sensors as feedback, the vehicle was driven aggressively to provide an excellent range of excitation in the data presented.

Figure 63 provides the path taken and Figure 64 the longitudinal velocity profile, both showing that the vehicle traveled in a very straight line over the flat dry surface with significant variation in the longitudinal velocity.

Figure 63: Path Traveled During Longitudinal Test with Google® Satellite Image [30]
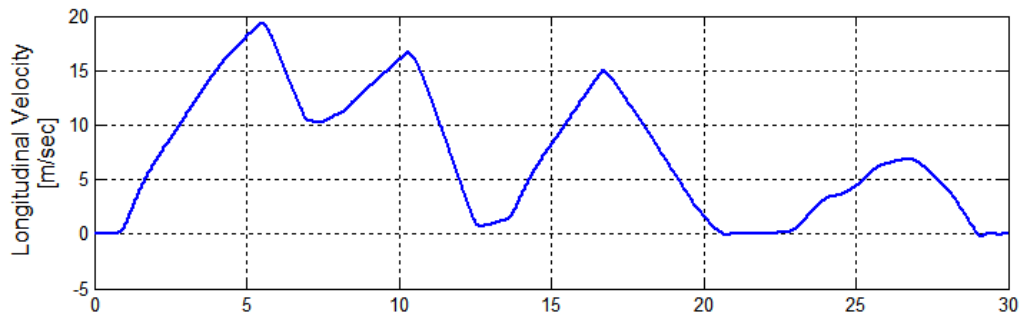
Figure 64: Longitudinal Velocity Profile

The estimated vertical force in Figure 65 has been provided by the FVE approach and clearly shows how each wheel experiences a significant shift in the vertical load. This is to be expected as the vehicle experiences pitching motion forward and backward with significant acceleration and braking during the maneuver.
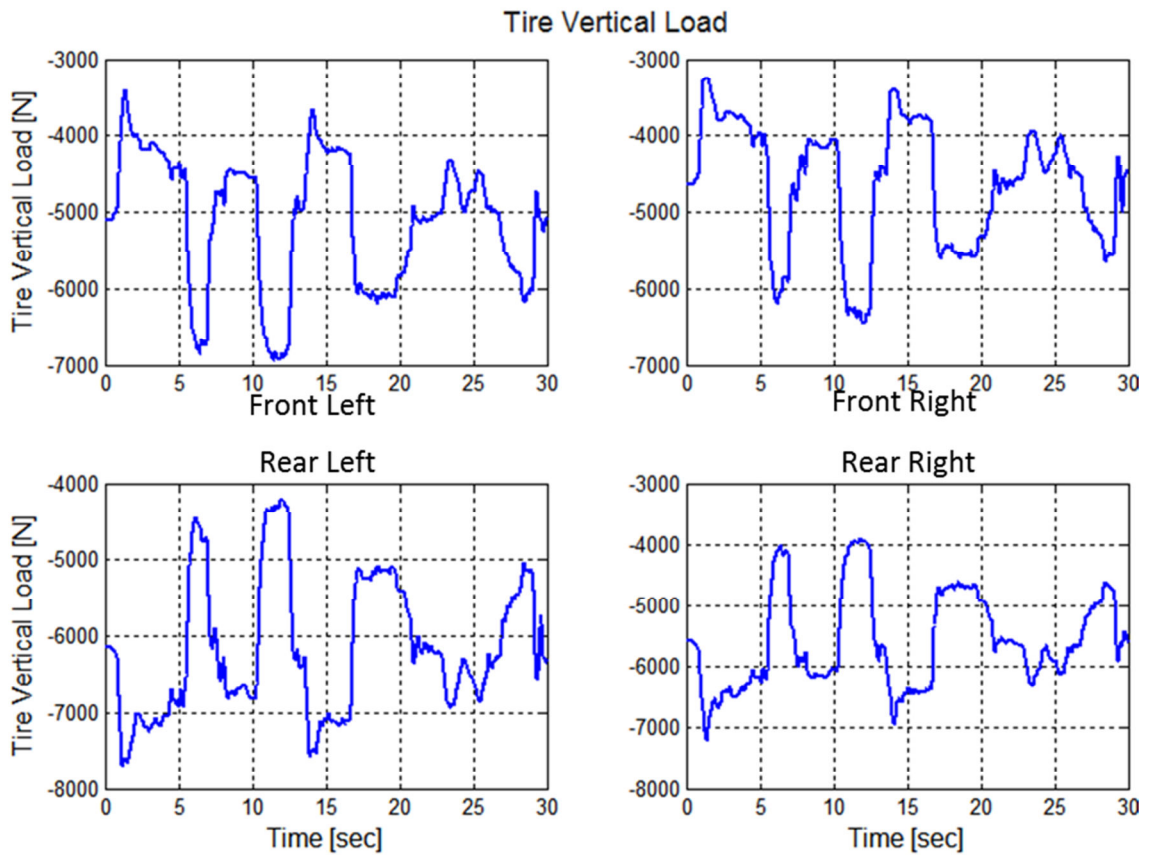
Figure 65: FVE: Four Wheel Vertical Tire Load

Meanwhile, the longitudinal force and estimated response have resulted in a very strong agreement, as shown in Figure 66. During the entire maneuver the two techniques nearly perfectly replicate the same data. All of the tire model estimates show a slight variant to the presented force data from the FVE. However, when one examines the velocity data in Figure 64, the observation that the vehicle stopped can be found. As noted previously, the result of such a condition is that the tire model is excited with only noise, either by the vehicle velocity or the wheel rotation rates. This would cause the tire model to slightly deviate from the real force estimation.
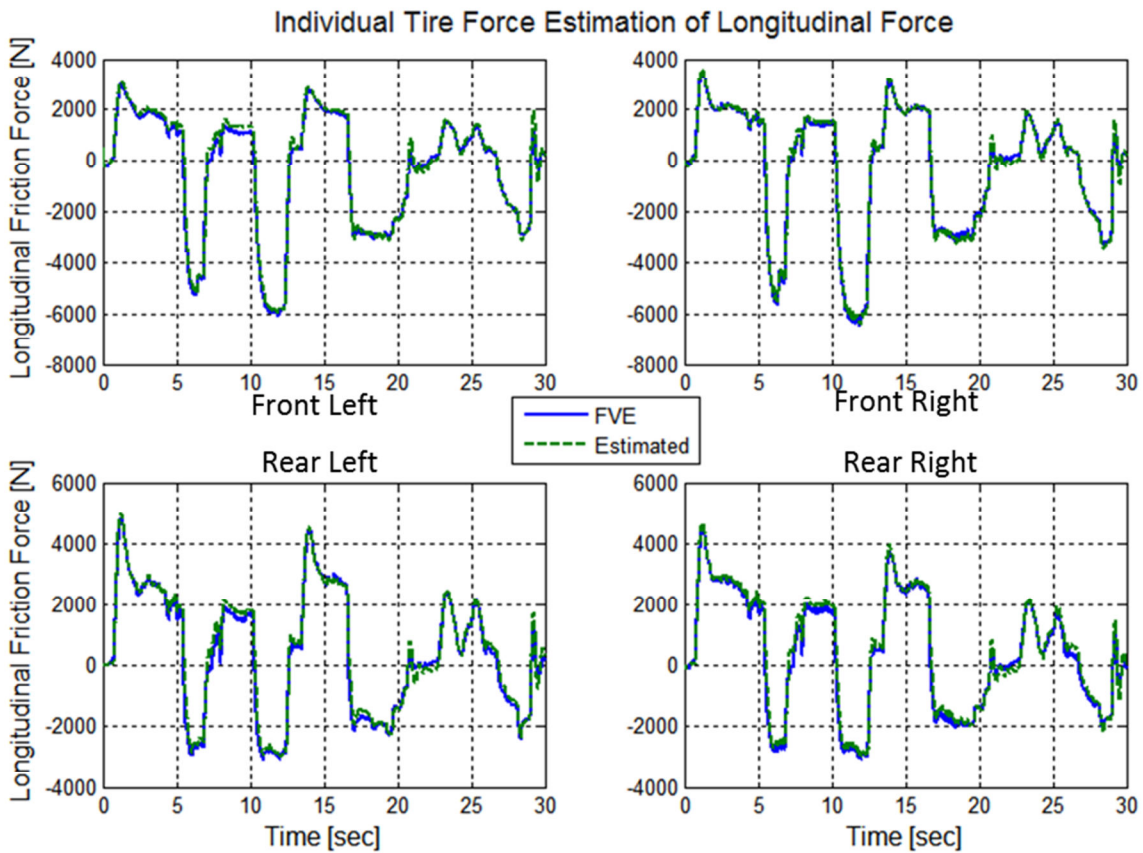
Figure 66: FVE: Four Wheel Longitudinal Force

The last result to note with this particular test is the tire capacity result. As this test was an aggressive longitudinally excited scenario, with little to no lateral data provided. However, during the more aggressive maneuvers, one would expect that the capacity limits are approached, or even the possibility of spikes at or around the capacity limits. Figure 67, has been provided to illustrate the results of the capacity estimation.
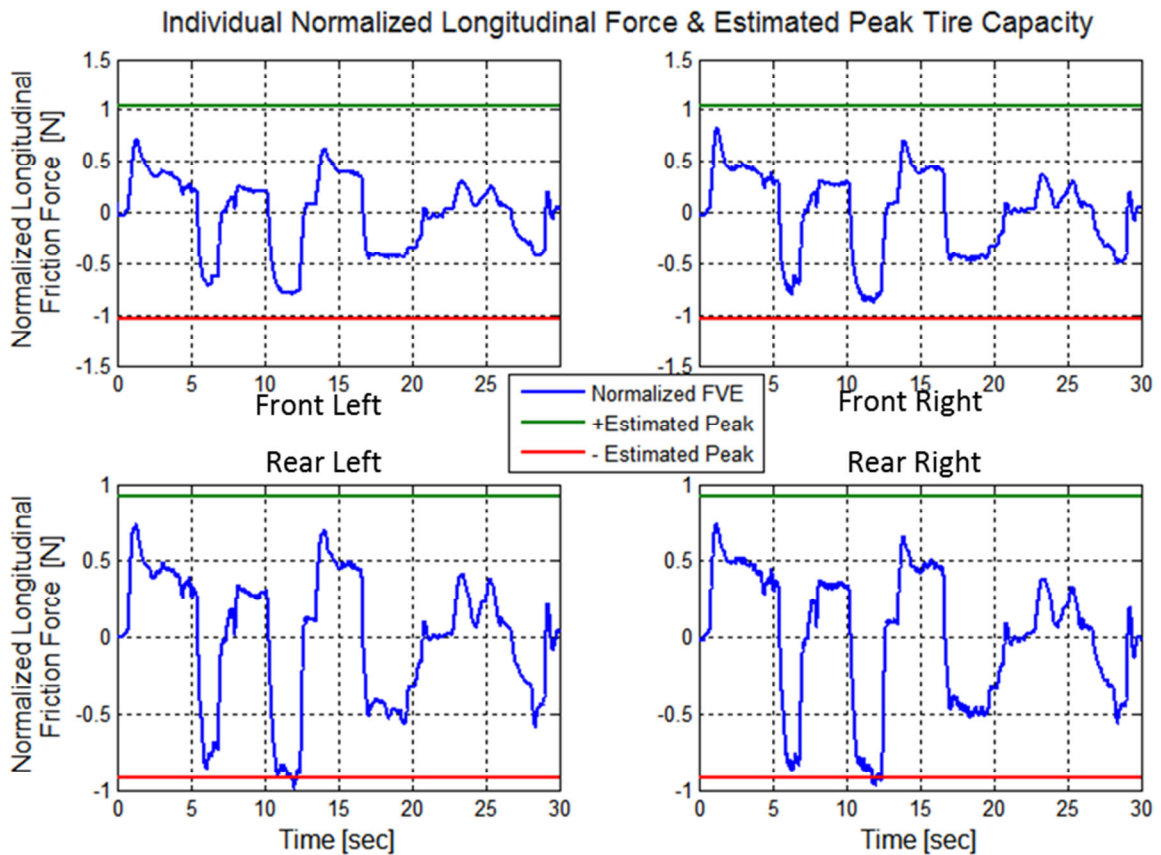
Figure 67: FVE: Four Wheel Normalized Longitudinal Friction Force and Tire Capacity Estimation

The presented results confirm one's expectations as Figure 67 shows how the tires were driven, on occasion, at the limits. Most notably, in this case, the rear tires are operating at the estimated steady-state limit with significant variations just after 10 seconds.

Collectively, this would suggest that the two approaches, the FVE and the tire model approach purposed, can, at least in the longitudinal direction, perform effectively together.

5.2.2 Evaluation and Findings Slalom Maneuver

The last test scenario to be presented with this vehicle, while using the FVE for feedback, is the slalom maneuver. This test has the vehicle swerving around multiple cones that have been placed in a

straight line 20m apart along the track. The vehicle undergoes continual lateral excitation as the vehicle swings around the cones. In order to perform this maneuver at higher speeds, a great deal of driver focus is required. Even still, oftentimes, the longitudinal velocity does not remain constant. Figure 68, shows the path taken as the vehicle veered around the cones. Meanwhile, Figure 69 shows the velocity at the vehicle's center of mass during the maneuver. In this particular test case, the vehicle's speed increases during the maneuver from the 8th to the 16th second when exiting the cones.
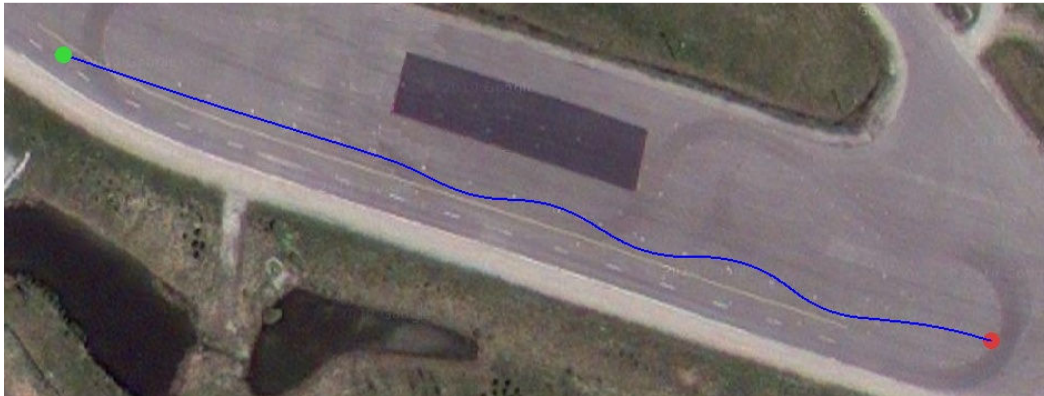
Figure 68: Path Traveled During Slalom Maneuver with Google® Satellite Image [30]
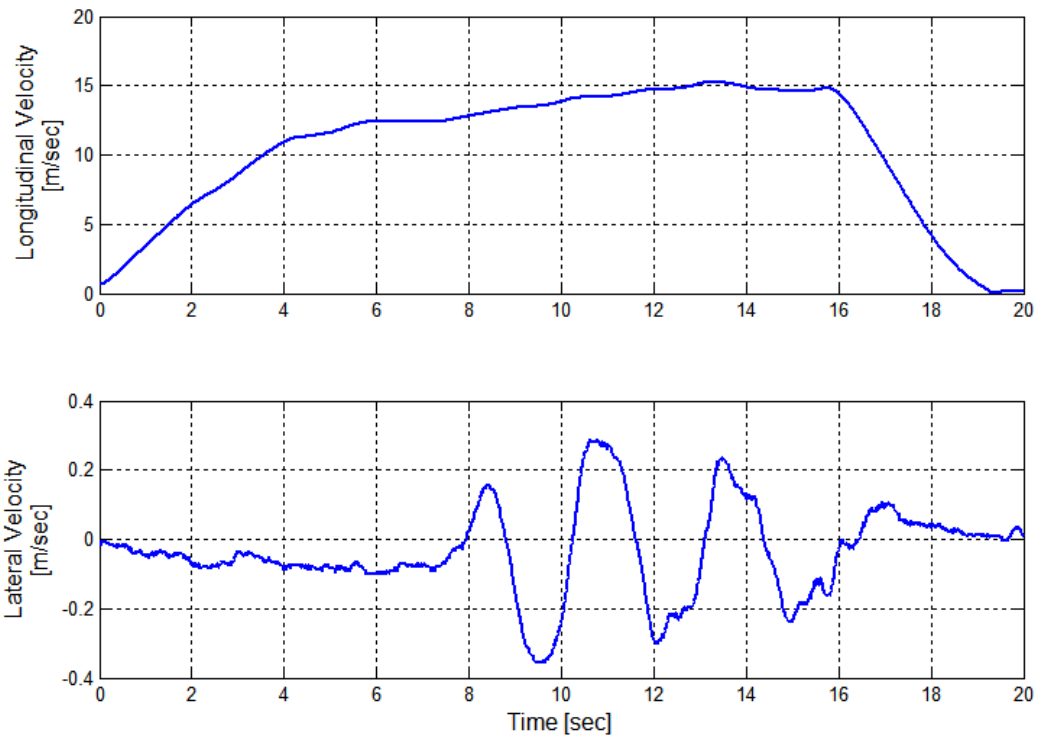
Figure 69: Slalom Maneuver Velocity Profile

Figure 70, shows the response of the FVE longitudinal force, along with the estimated force. The results are mainly in agreement in the regions where the longitudinal motion is changing more significantly; specifically, during the initial acceleration and braking after the maneuver. However, the tire model did not always agree with the FVE in the middle of the maneuver. The longitudinal force is relatively small, but unfortunately, the tire model estimates are out of phase with the FVE. The difference could be the result of the vehicle planer model assumption. By not accounting for the pitch and roll dynamics and how they would contribute to the velocity at the wheel centers, the tire model will be less accurate. Two components of vehicle motion have been omitted and can slightly change the velocity calculated at each wheel considering that the forces are relatively small compared to the rest of the vehicle motion. This would suggest that the corrections might be as simple as the inclusion of the two measurements.
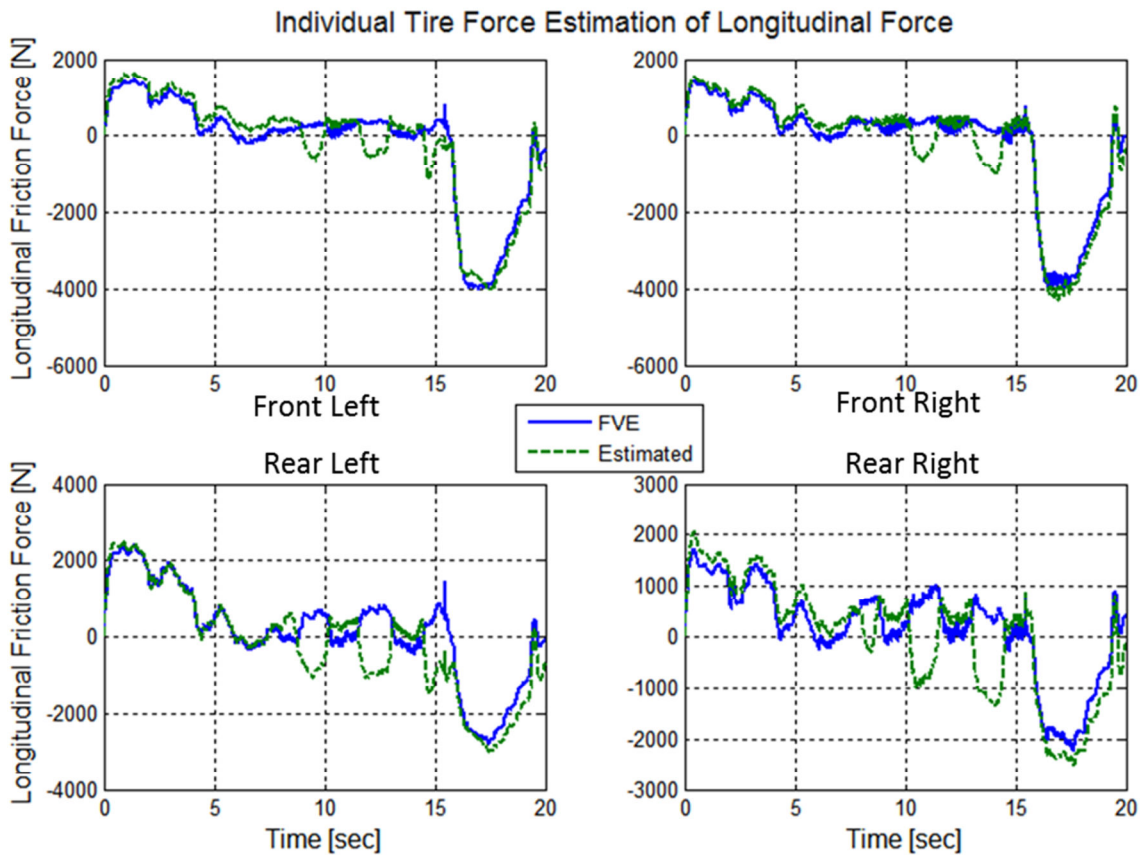
Figure 70: FVE: Slalom Four Wheel Longitudinal Force Estimation

Figure 71 has been provided to indicated the detailed analysis of the front right tire during this slalom maneuver in the region where the force estimation no longer agreeing with the FVE data. This discrepancy, which also relates to the other tires, is the result of the kinematic excitation that the tire is heavily based on. As noted in Chapter 2, tire models that rely heavily on the slip information, as this model does, often have discrepancy issue when the slip is very low. This is because the real world measured errors and estimation errors can significantly dominate the slip response in very low slip excitation cases. Figure 71 shows how the two regions where the estimated force significantly diverges from the FVE estimated response is momentarily after the $R_{eff}\omega$ velocity data drops below the V_x curve. Clearly the force is still positive with the wheel providing forward thrust as the FVE indicates. However, the tire model is provided data that relates the modeled vertically fixed wheel to be rotation such that the slip ratio is in the braking region. As a result the tire model predicts braking behavior. It is worth noting that the FVE force has been confirmed to be accurate by referencing the

90

data from the in-wheel hub sensors for this case. The estimation conditions can be improved by accounting for factors that contribute to changes in the effective radius. In this particular case, the camber angle with the tall tire wall can result in R_{eff} discrepancies from a centerline radius. Only a small radius change is required to contribute a large enough difference that the calculated slip will differ noticeably in this sensitive region and can correct the predicted braking conditions currently estimated.
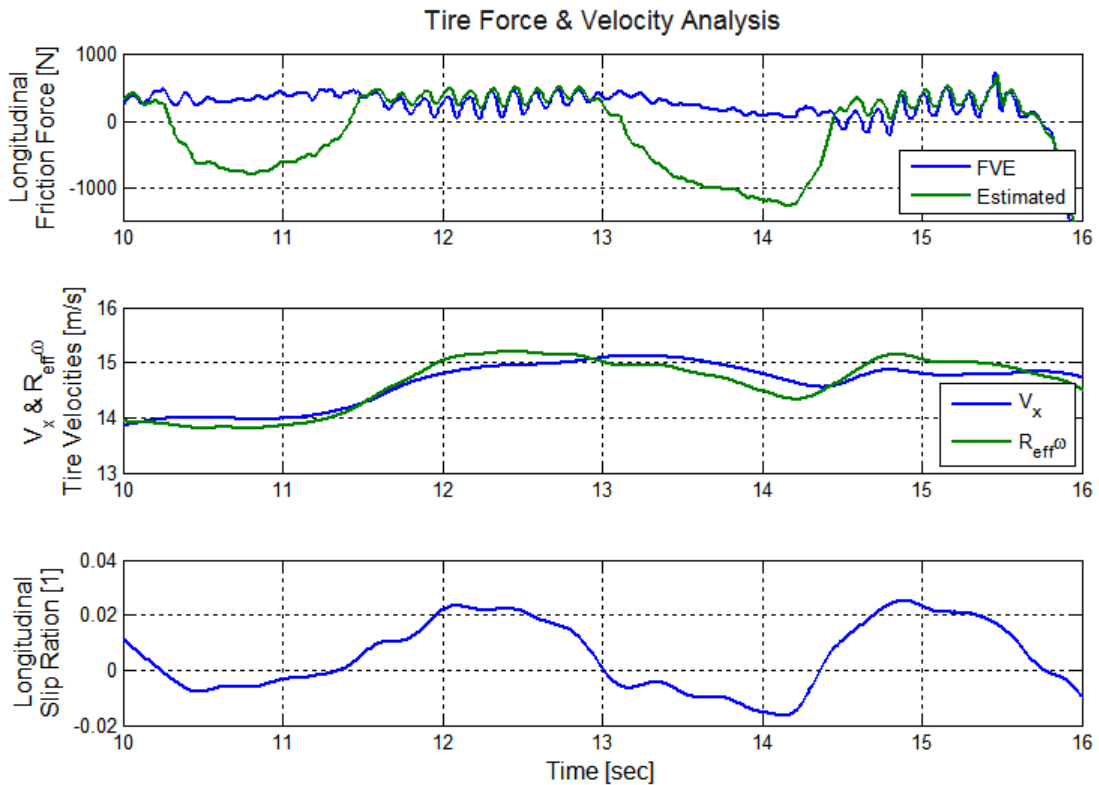
Figure 71: Detailed View of Front Right Force and Velocity Data

The lateral forces, as shown in Figure 72, have been well matched by the tire estimation. The significant lateral loading during the maneuver has provided repeatedly large forces that relate well with the side to side motion as the vehicle swerves through the cones. This maneuver provided an excellent set of data with lateral load characteristics that are repeated each time the vehicle swung around a cone. By matching the peak estimated on the lateral force shows that the entire estimation

process is working well with the FVE and relating the characteristic of the tire to what was physically happening to the vehicle during the maneuver.
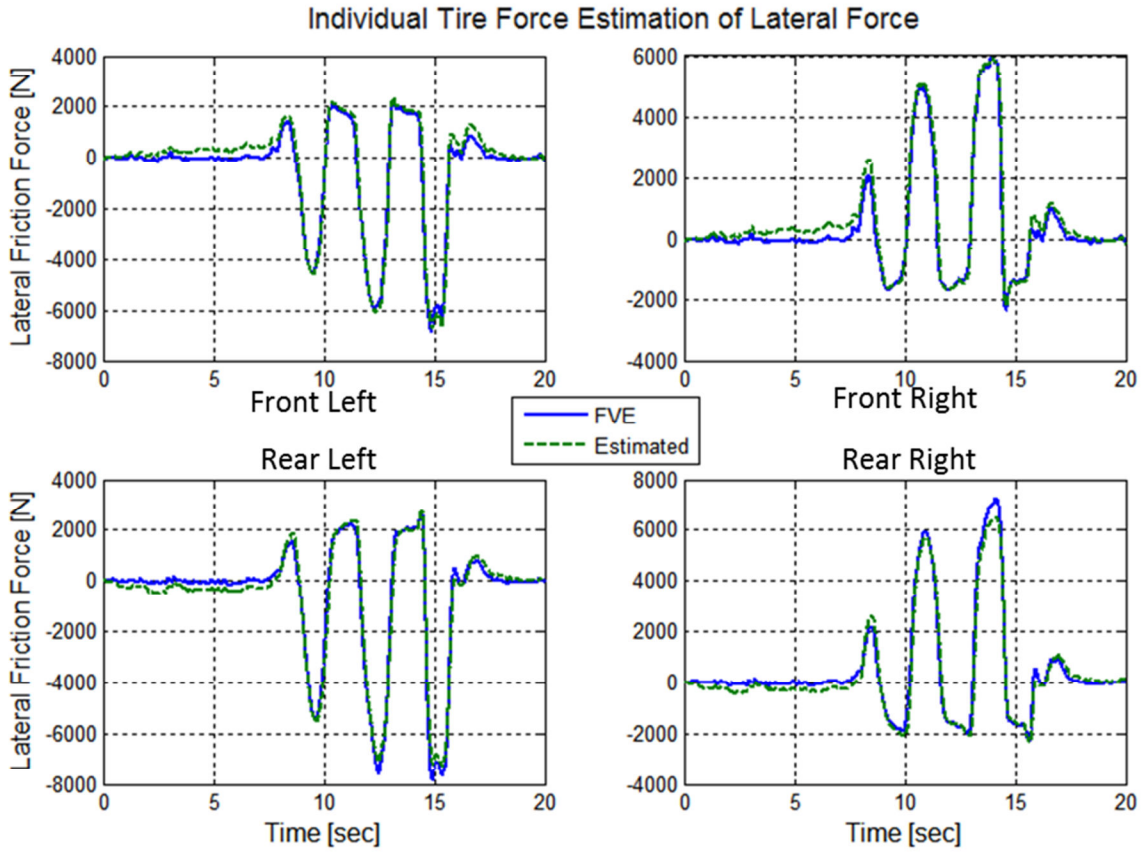
Figure 72: FVE: Slalom Four Wheel Lateral Force Estimation

By examining Figure 73 and Figure 74, one can observe the capacity estimation data that pertains to this test case. As would be expected, the longitudinal loading is well within the limits for each of the tires. Even the smooth acceleration and braking at the start and end of the test are only using about half the estimated available force.
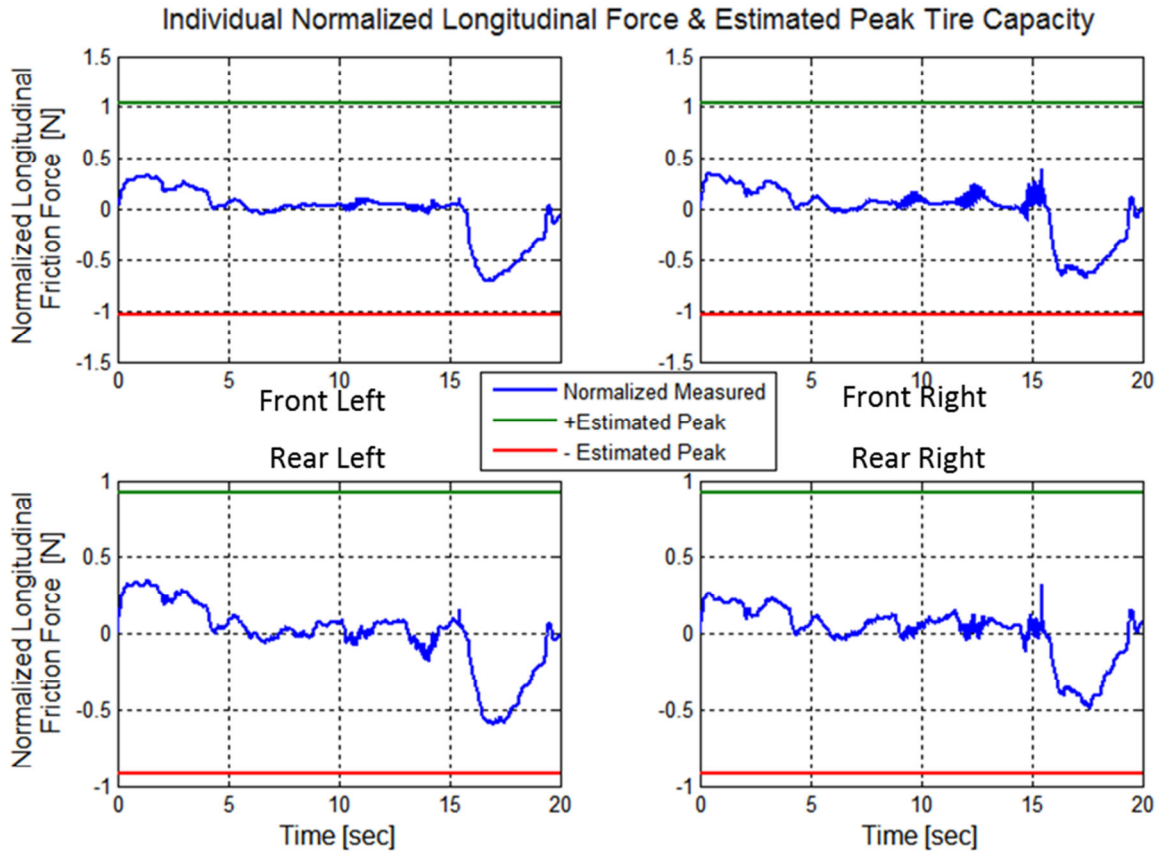
Figure 73: FVE: Slalom Four Wheel Normalized Longitudinal Friction Force

and Tire Capacity Estimation

However, with such a large lateral force, reaching in excess of 6000N, the lateral force would normally be very close to the limit or even exceeding it. Fortunately, the capacity for each tire was not exceeded by virtue of the vertical load transfer, as shown in Figure 74. The extreme load transfer that the vehicle underwent from side to side can be observed in Figure 75. This figure shows how the left side loading is opposite to the right side loading as the vehicle would have experienced significant roll motion during the maneuver. Additionally, when the tires applied the greatest lateral force, the vehicle loading due to the roll, would help by vertically loading the desired tires. This process can be observed by examining the peak loading in Figure 74 and comparing the timing with the large magnitude in Figure 75.
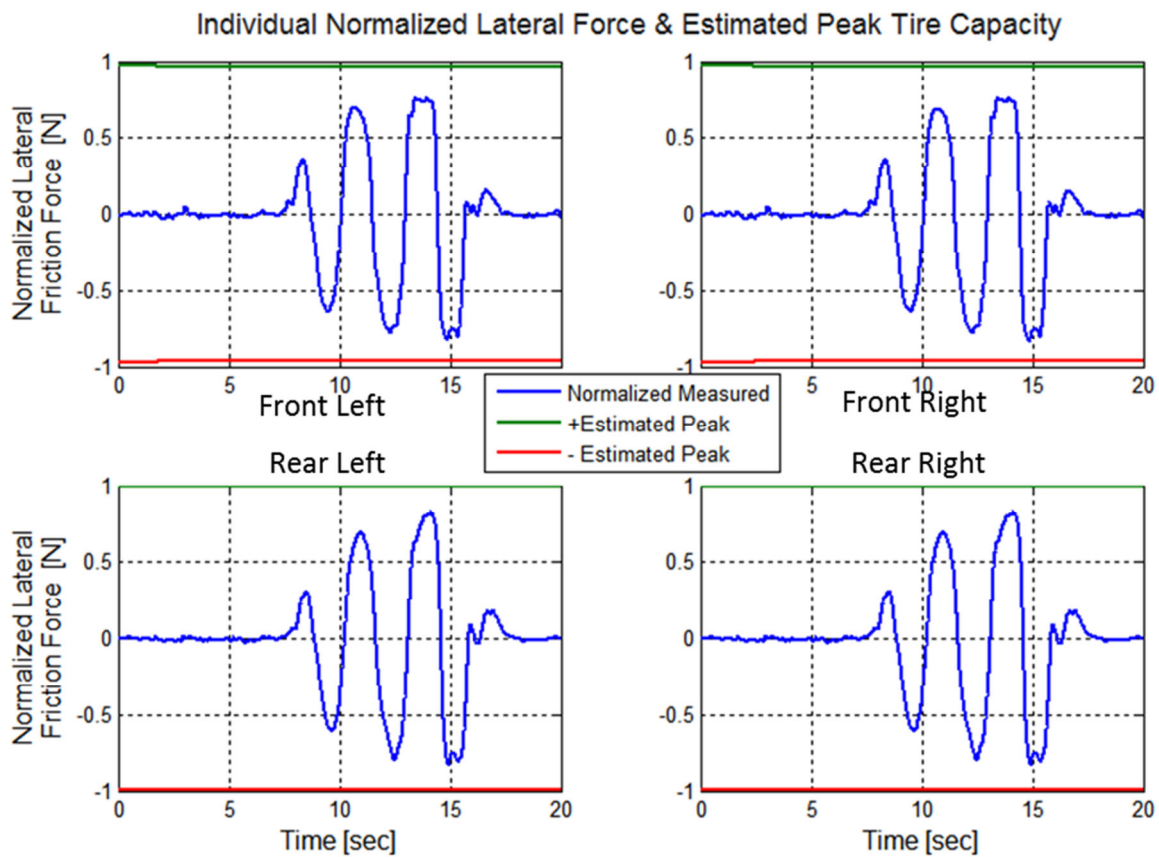
Figure 74: FVE: Slalom Four Wheel Normalized Lateral Friction Force

and Tire Capacity Estimation
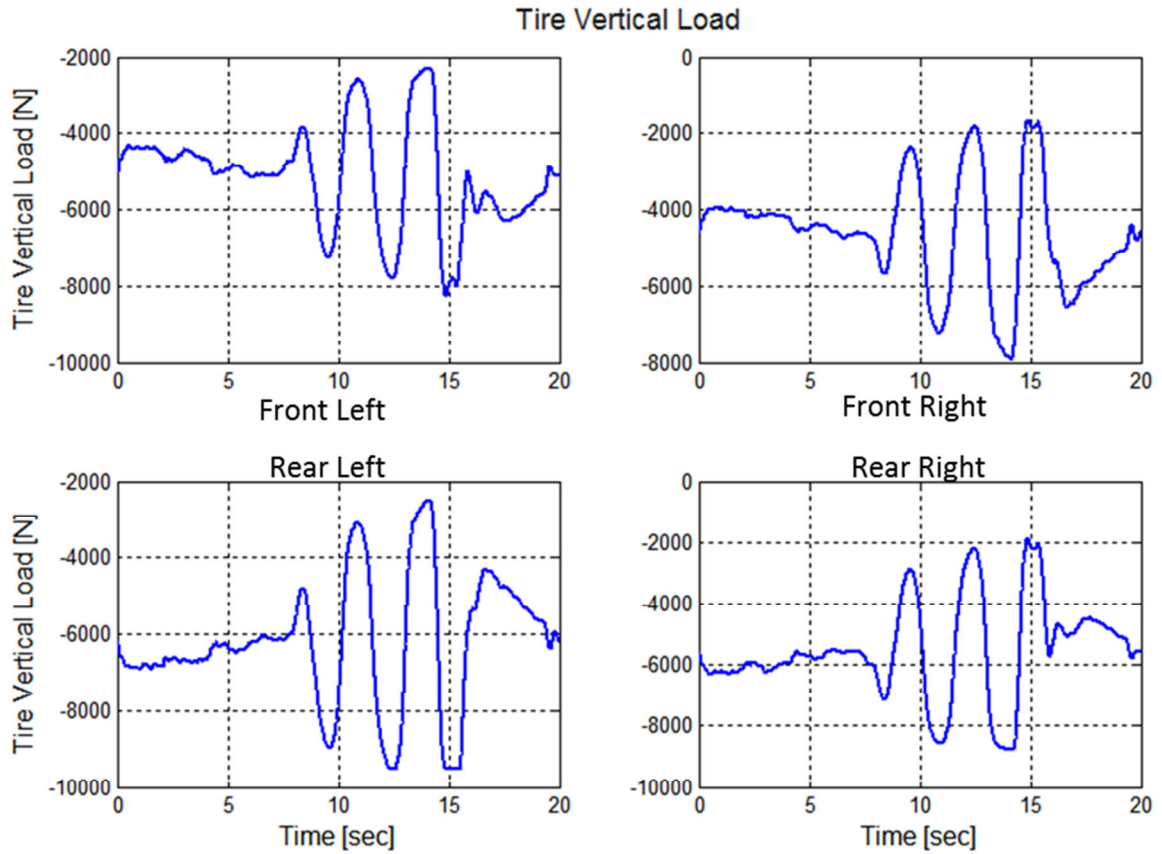
Figure 75: FVE: Four Wheel Vertical Tire Load

5.2.3 Full Vehicle Estimation and Tire Model Instrumented Vehicle Application

The UKF application with the tire model can be observed to perform adequately well once again with the instrumented vehicle, even while using the FVE instead of the wheel hub sensors. The next major task with the tire model application was to apply this same approach with a vehicle that does not have wheel hub sensors. The entire process would need to be repeated and developed for an electric vehicle that will use the FVE and then utilize the tire model with the UKF. This would require doing the entire parameter identification process with just the information that the FVE provides for feedback.

5.3 Full Estimation with Fully Electric Concept Vehicle

As part of the fundamental overall project goal, the objective would be to allow the FVE and tire model approach to be transferred reasonably easily to other vehicles without the full instrumentation required in the Cadillac® previously. In order to examine this possibility, a fully electric vehicle was selected.

5.3.1 Fully Electric Concept Vehicle

This vehicle was also loaned to the University of Waterloo from General Motors® as part of the research work being performed. The vehicle is an Opel Corsa® with four in-wheel electric motors, thus making the entire test platform fully electric. Much like the previous vehicle discussed, the six-axis IMU with GPS is reused in this test vehicle. Additional sensors on the Corsa® include: the hand wheel angle, four wheel rotation rates, and individual torque data. The torque information were provided by electric motors and their controllers. Figure 76, provides a view of the vehicle and the in-wheel motors.

Although this vehicle is not capable of directly measuring the forces applied at each wheel, the results of the FVE can be inferred based on the sensors available to validate that the results are reasonably accurate. The FVE approach is the same as previously applied on the fully instrumented Cadillac® as it passes the force estimates to the tire friction model estimations. The validation approach selected for the tire friction estimation, is however, based on determining parameters from one set of test data and validating it with another test data set. Provided that the second set of testing is able to perform adequately, then the modeling will be considered for further investigation. The parameter identification approach is applied in much the same way as previously described, with the difference being that the estimation forces from the FVE are to be used as the reference forces in the identification process.
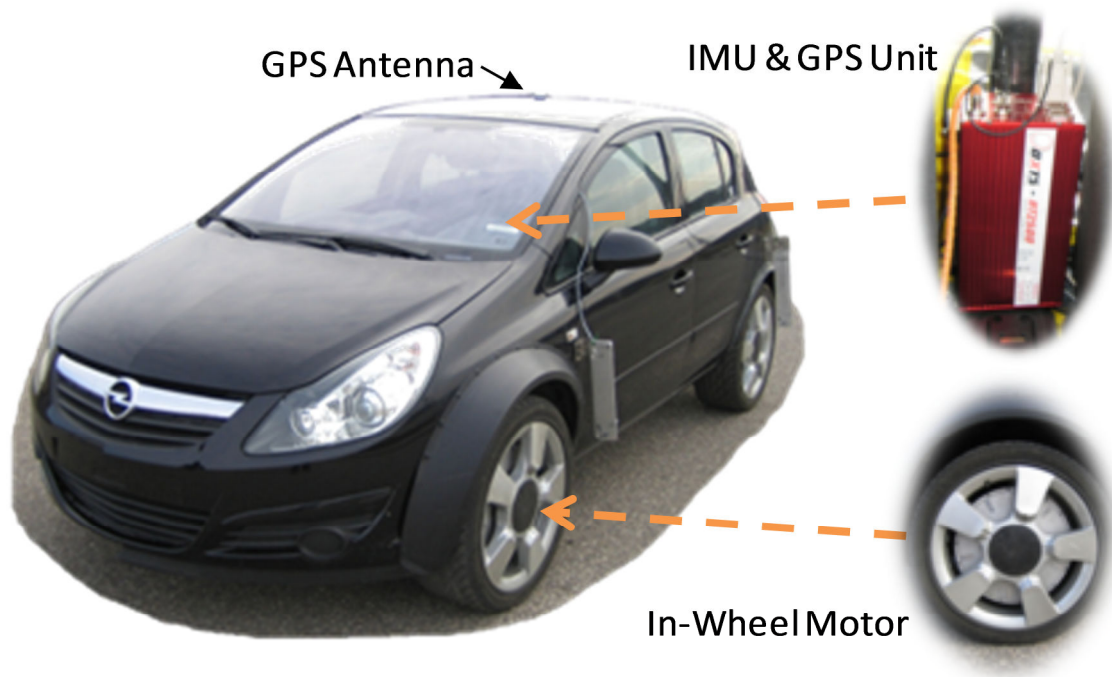
Figure 76: Fully Electric Opel Corsa® with In-Wheel Electric Motors

After the parameter configuration was complete the Opel®'s two test cases had then been selected to present. The first test case was a variation on the slalom maneuver. This time the cones where placed with a 1m offset from the straight-line. This maneuver was referred to as the wide slalom, and forced the vehicle to swerve more dramatically around cone arrangement. This test case often yielded slower speeds but much greater lateral excretion and lateral slip. The second test case provided was a straight line acceleration and brake. Only this was performed at a high constant torque as commanded by the vehicle. Both of which are discussed in the subsequent section. Figure 77 has been provided to illustrate how the testing was performed by having the vehicle travel through predefined paths for each of the test cases.

Figure 77: Panorama of Opel® Research Vehicle Performing a Maneuver

5.4 Electric Vehicle: Evaluation and Findings Wide Slalom Maneuver

This particular test case examined shows the vehicle's response with both the wide slalom and a smooth acceleration and brake in one example. The wide slalom maneuver used a 1m offset for the cones so that the vehicle went wider around the track resulting in a greater lateral demand on the vehicle. This enabled a great deal of lateral excitation, while the lead in and lead out of this test allowed the capture of the longitudinal motion. This test provided an excellent opportunity to illustrate the main tire estimation components. Figure 78 shows the path taken by the vehicle during the maneuver. Additionally, the related velocity information, shown in Figure 79, indicates how the speed was maintained between 8 and 10 m/sec (28.8 and 36 km/hr) during the slalom stage of the maneuver. The figure also provided details regarding the smooth change in longitudinal velocity both before and after the slalom phase.
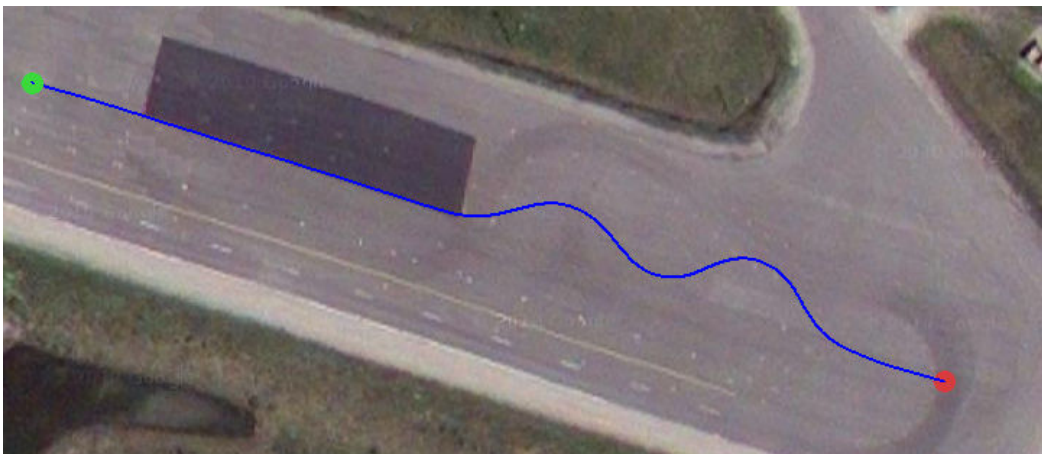
Figure 78: Electric Vehicle Path Traveled During Wide Slalom Maneuver with Google® Satellite Image [30]
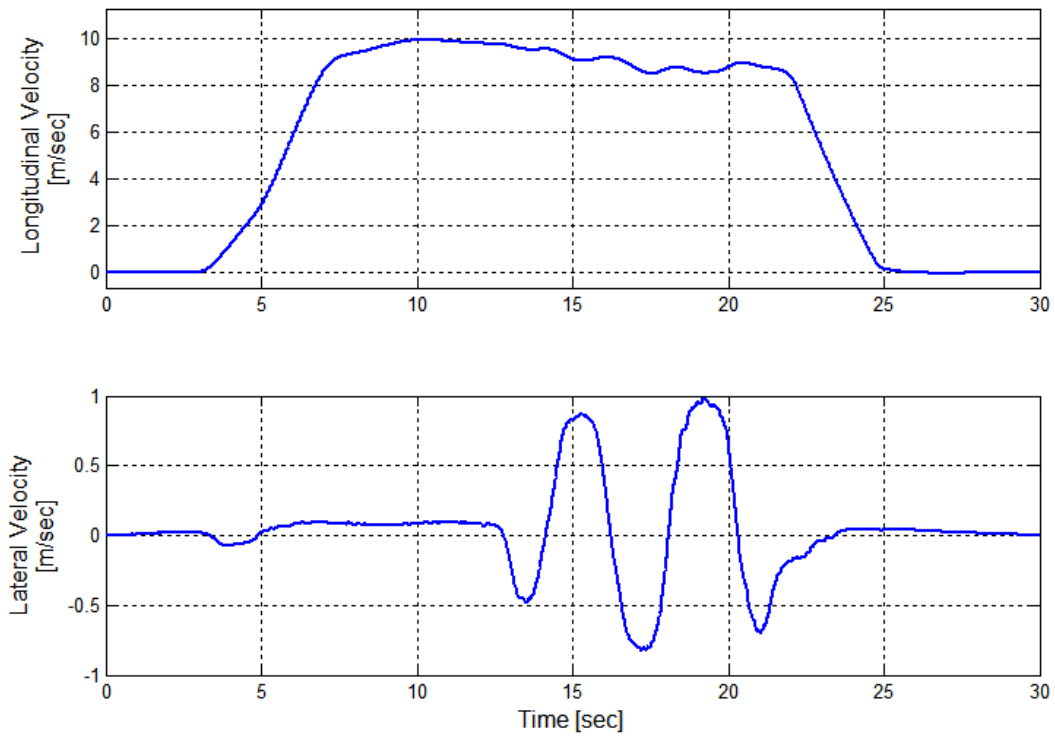
Figure 79: Electric Vehicle Path Wide Slalom Maneuver Velocity Profile

This is followed by the vertical forces as estimated by the FVE in Figure 80. Much like the normal slalom maneuver, the results shown in Figure 80 illustrates the load change from side to side. Again, the slalom maneuver has the advantage of providing increased vertical loading to the outside wheels as needed to direct the vehicle around the course.
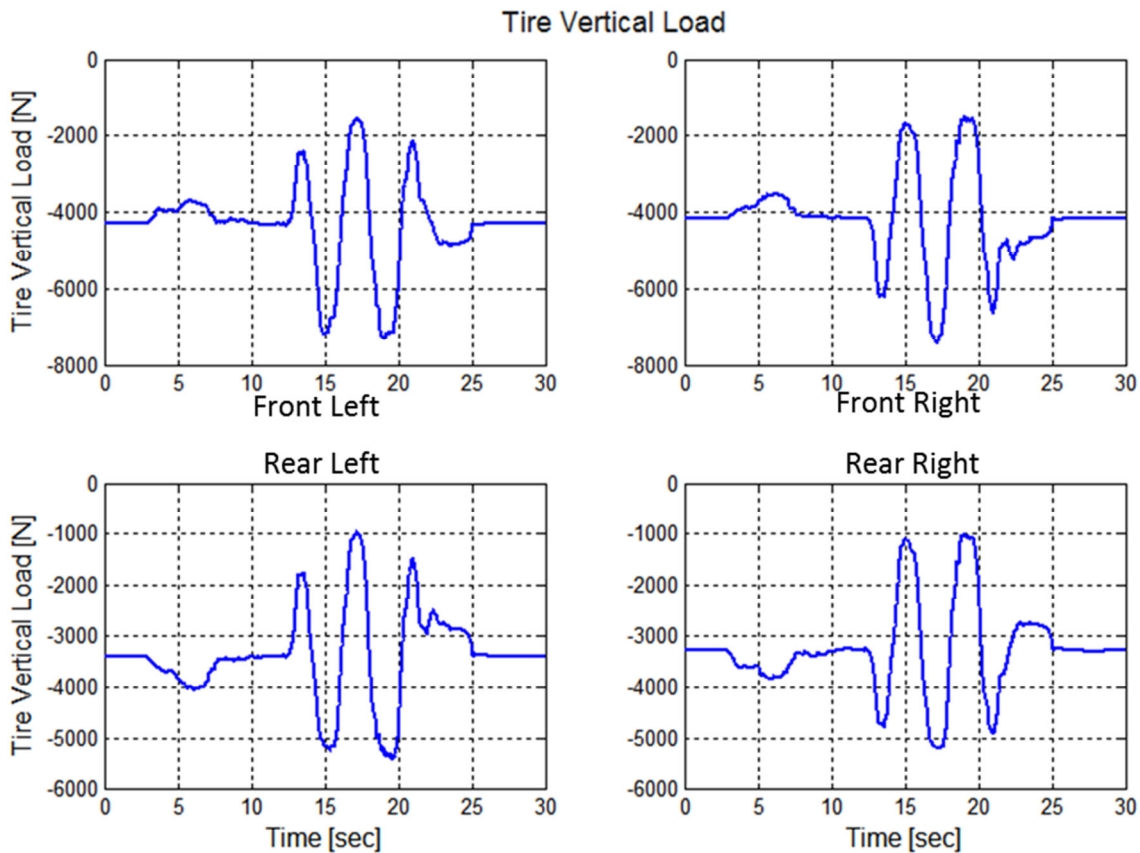
Figure 80: Electric Vehicle Wide Slalom Maneuver FVE Vertical Tire Load

Meanwhile, Figure 81 and Figure 82 contain the longitudinal and lateral force estimations respectively. The longitudinal force can be seen to estimate the results quite accurately during the acceleration and braking phase of the maneuver. The force estimate during the slalom portion was maintained reasonably well however some improvement can be made. This would likely be accomplished though the same consideration noted previously regarding the slalom testing with the instrumented vehicle. Fortunately, the accuracy was better in this vehicle. However, the test was slower, the vehicle's sprung mass was notably lighter by using in-wheel motors instead of an internal combustion engine, and the tire walls were much shorter minimizing tire deformation from wheel camber angles that would affect R_{eff} values. These considerations reduced the vehicles sprung-mass pitch and roll motion during the maneuver and minimize tire changes that are not accounted for. As a result, this allows the velocity relation that is based on the planar kinematics to be more accurate.
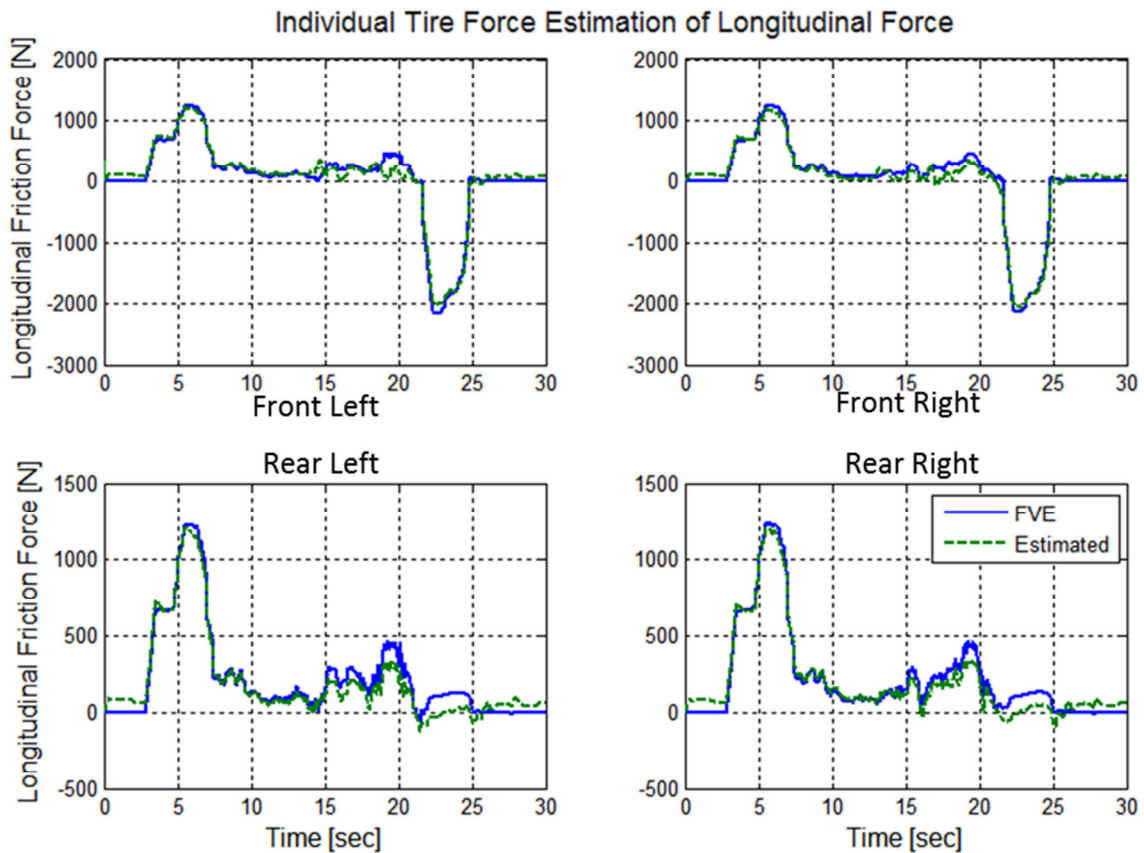
Figure 81: Electric Vehicle Wide Slalom Maneuver FVE Longitudinal Forces

As for the lateral forces, the rear tires performed excellently. The entire response was nearly identical to the FVE. Particularly, the peak estimates that indicated the accurate characteristics for this maneuver, where very well estimated. The front tires nearly performed as well however, after some investigation the reason the peak force estimates were not fully realized was the result of the steering relationship to the individual wheels. Since the vehicle steering was modified, by the accommodations made for the large in-wheel motors, the relationship between the hand wheel and the tires was no longer as linear of a relation. At the time the best approximation was considered and some of the nonlinear response was accounted for. Putting aside that shortcoming, the general response was quite well estimated throughout the maneuver.
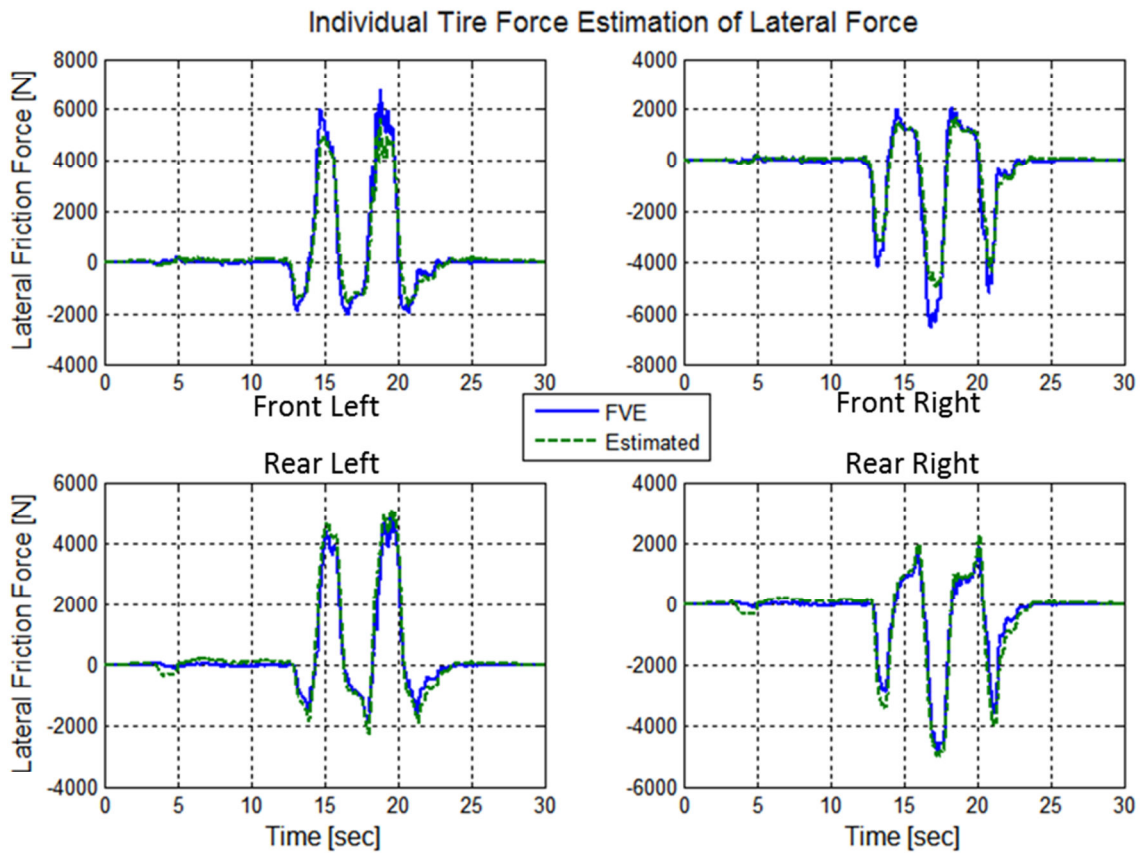
Figure 82: Electric Vehicle Wide Slalom Maneuver FVE Lateral Forces

Lastly, the capacity estimates for this maneuver have been provided in Figure 83 for the longitudinal direction and Figure 84 for the lateral. The longitudinal limits were not approached as this maneuver was not intended to overly excite the longitudinal components. Although, the tire capacity estimates in Figure 83 do provide an interesting insight into the vehicle motion control. That insight being, the vehicle was configured to have uniform acceleration from each of the wheels but, during braking only the front wheels where involved. In fact, the rear wheels provided a slight forward force as each of the motors where configured to provide a slight forward creeping force nominally. This creeping force was to replicate the slight creep experienced by conventional vehicles when the vehicle is stopped with the engine running and gear engaged. The creep force is generally very small but can be noticed in the figure below.

102
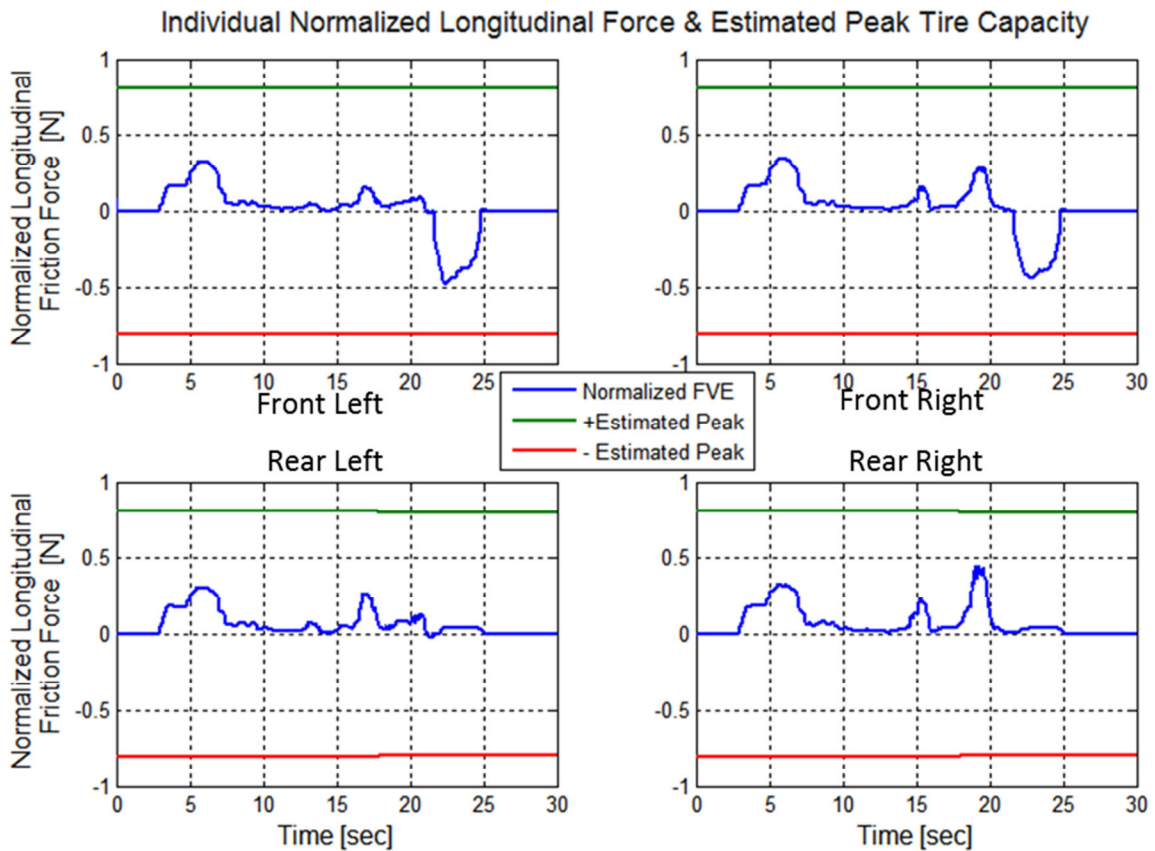
Figure 83: Electric Vehicle Wide Slalom Maneuver Normalized Longitudinal Forces and Tire Capacity Estimation

Unlike the longitudinal response, the lateral capacity estimates are approach by the lateral forces experienced during the maneuver. This was the reason why this test was performed at a much lower speed compared with the normal slalom maneuver. In this case the vehicle was nearly at the lateral limits and in fact this was the purpose of the wide slalom, to get such a high lateral excitation. This test case was able to accomplish this high lateral excitation goal exceedingly well. As observed previously, the normalized forces start to become very noisy as the tire capacity limits are approach. This can be seen to some extent in the lateral results provided in Figure 84. However, the limits were not exceeded and the driver was able to navigate the course.
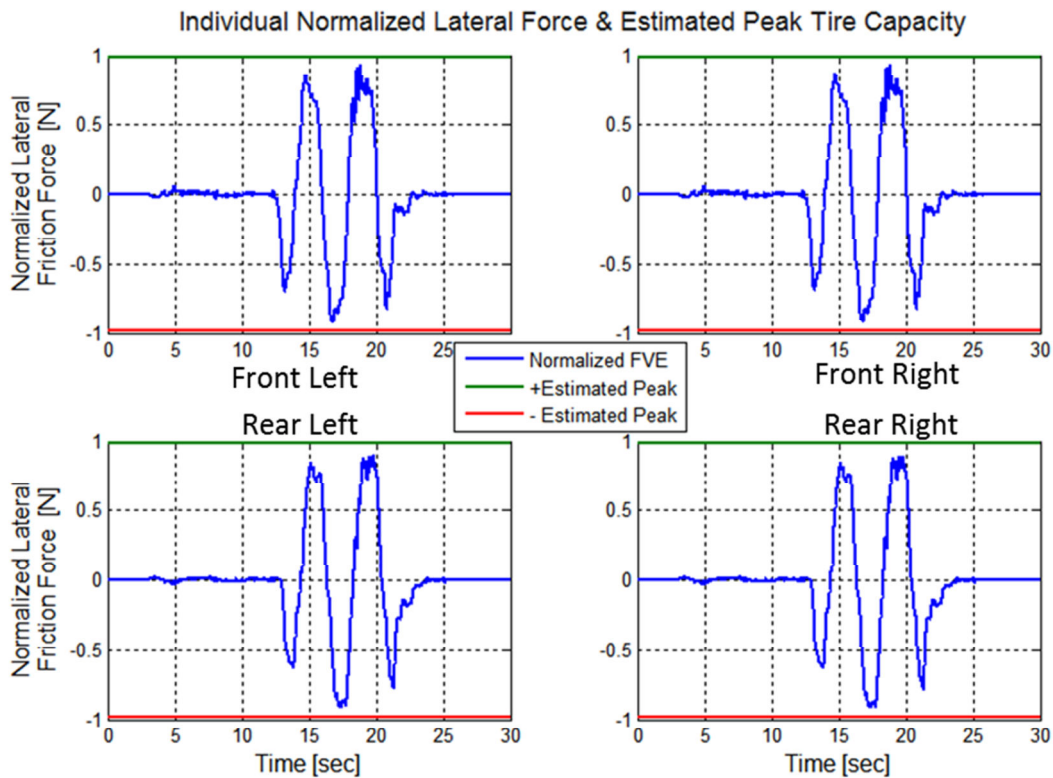
Figure 84: Electric Vehicle Wide Slalom Maneuver Normalized Lateral Forces and Tire Capacity Estimation

5.5 Electric Vehicle: Evaluation and Findings Acceleration and Braking Test

This acceleration and brake test has been provided to show the current limit of how the FVE and the tire estimation perform together. This straight line test case can be observed in Figure 85 with the related velocity profile in Figure 86 below.
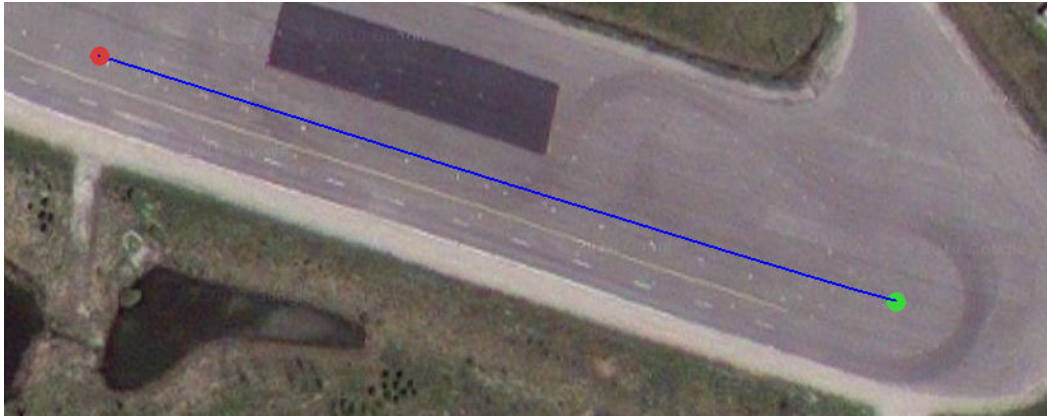
**Figure 85: Electric Vehicle Path Traveled During Acceleration and Brake with Google®
Satellite Image [30]**
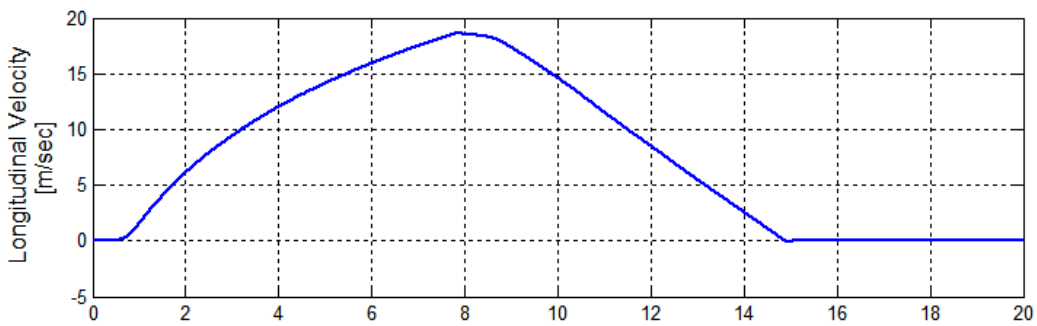
Figure 86: Electric Vehicle Path Traveled During Acceleration and Brake Velocity Profile

The longitudinal force estimates can be observed in Figure 87. The estimated longitudinal forces were approximated less than the FVE data during the very aggressive acceleration. All four wheels show this response and suspiciously all of the forces converge to a value of approximately 2250N. Then the front brakes were applied and the tire estimate converged back to results that agreed with the FVE before the vehicle fully stops.
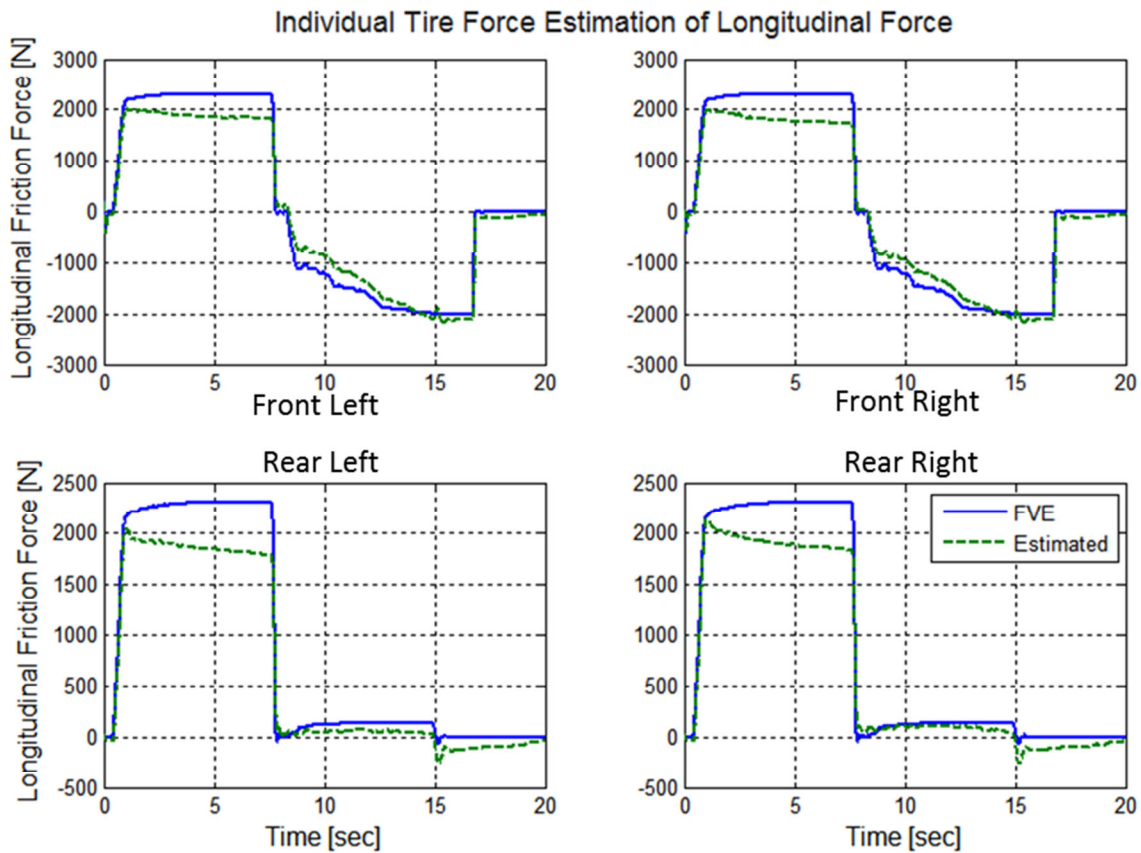
Figure 87: Electric Vehicle Path Traveled During Acceleration and Brake Longitudinal Forces

The force profile is highly aggressive and unusually smooth for such an aggressive acceleration. When one considers the vertical force that are estimated, the vertical load clearly shifts to the back wheels quickly then tapers back to an equilibrium before abruptly shifting the load to the front wheels during braking. Figure 88 shows the behavior as expected of the vertical load transfer as described. Therefore, despite being highly abrupt in transferring the vertical load results do not indicated any significant contribution to the longitudinal force discrepancy.
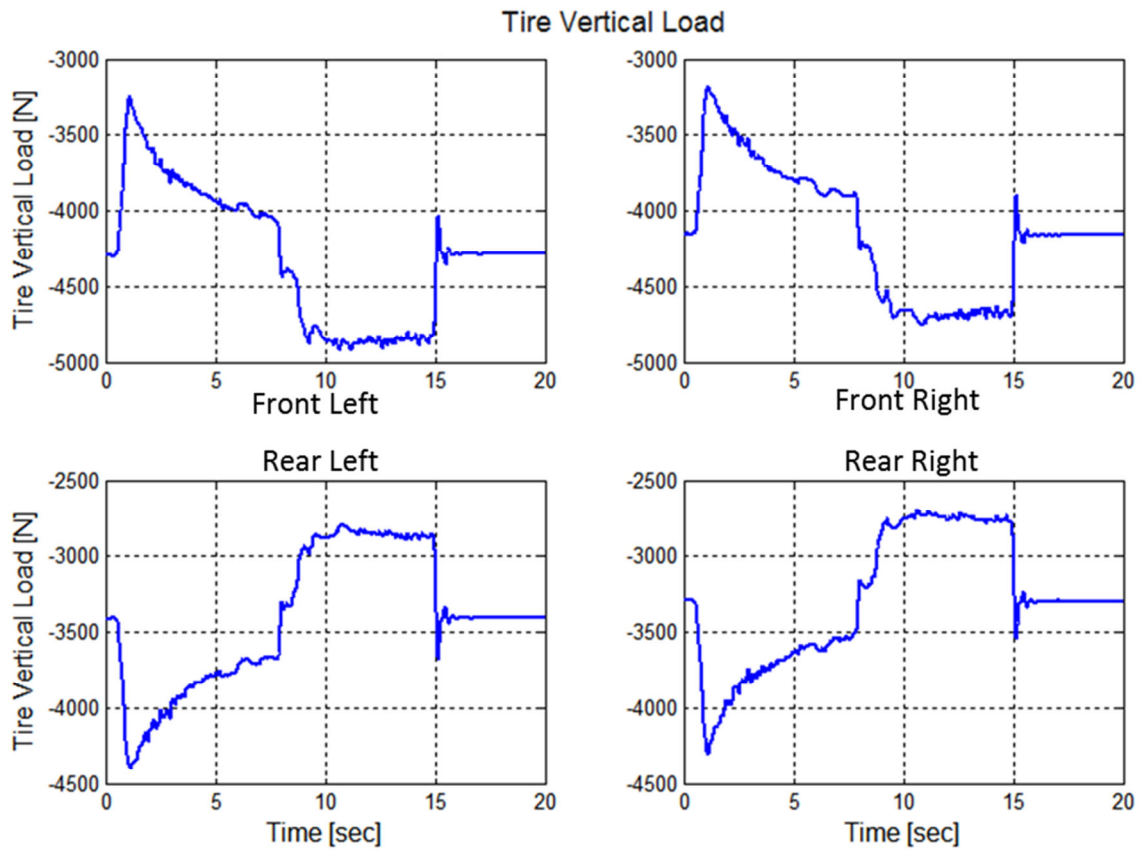
Figure 88: Electric Vehicle Path Traveled During Acceleration and Brake Vertical Tire Load

Similarly, the capacity limits were approached but not exceeded as shown in Figure 89. Rather, the expected longitudinal results can be found with all wheels providing the large driving force, then the front wheels braking, and rear wheels show the slight creep force.
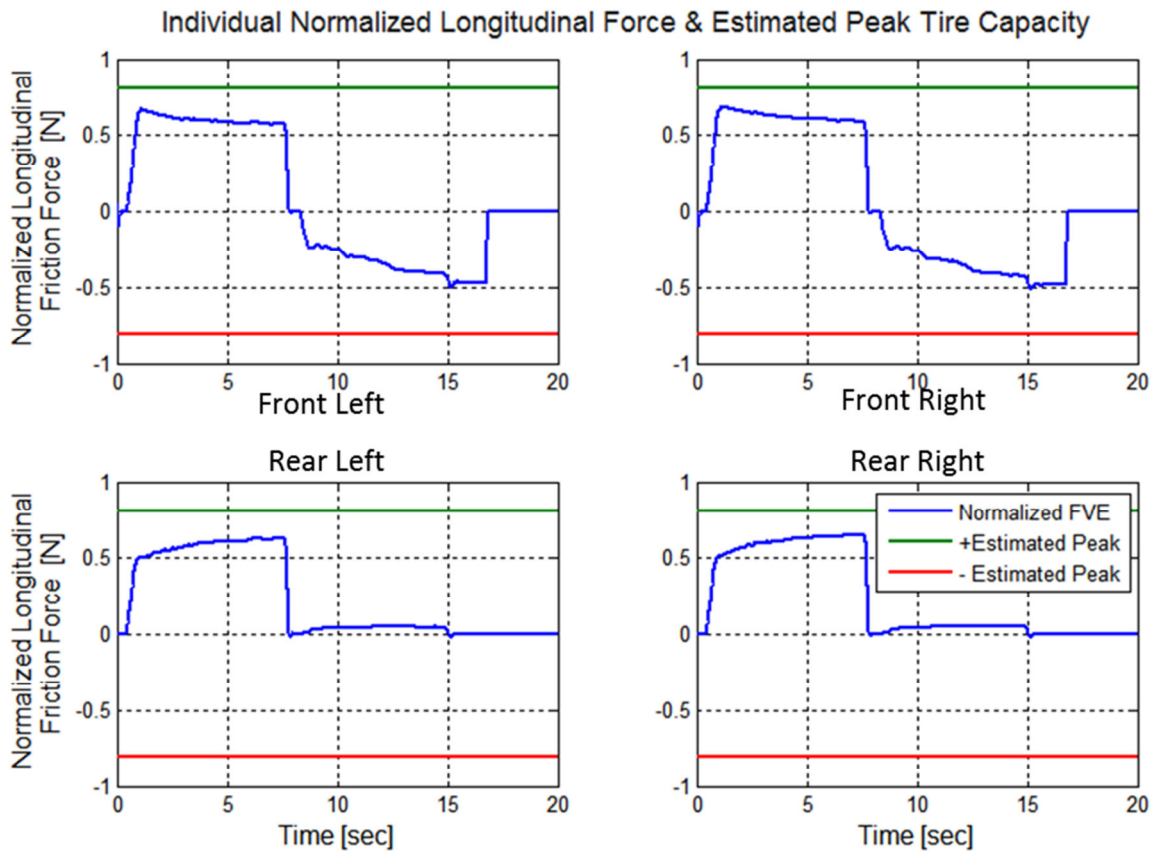
Figure 89: Electric Vehicle Path Traveled During Acceleration and Brake Normalized Longitudinal Forces and Tire Capacity Estimation

Instead, this discrepancy was the limitation of how the current FVE and the tire model approach work together. The FVE was provided with very large torque data that was commanded by the in-wheel motor controllers but not guaranteed to be applied. This discrepancy was only present during very large torque loading. Unfortunately, without directly measuring the torque the FVE was mislead by the high torque signals suggested by the motor controllers, and as a result indicated that the force was actually achieved. Since, the tire model approach relies on the force feedback that the FVE provided, subsequently, higher forces were estimated. However, the tire model did not agree with the sustained force exerted. Lastly, the tire model would not be able to adjust for this condition as the road condition was nearly ideal and the tire model's parameters are limited to roads with conditions slightly less than ideal. Thereby, not allowing the model to exceed a physical limitation imposed on the parameters that do not allow for road conditions that are better than ideal.

This experimental short coming would ideally be addressed though the inclusion of a torque sensor or a more accurate torque input to the FVE. However, this did provide the opportunity to consider an extreme case that might make the tire model and capacity estimates produce unstable results. Fortunately, the capacity estimated was very stable as the parameters where limited by the physical restrictions imposed. As a result, if a controller was relying on the capacity estimated output, the controller would have been provided with stable estimates even when the force estimation was not in agreement.

5.6 Conclusion and Further Considerations

These test have shown that the FVE and the tire model approach can perform quite well even when converted to other vehicles. This freedom to be placed on alternative vehicle platform is one of the great advantages for this approach and has now been shown work with both an electric and a conversional internal combustion engine vehicle. Additionally, the approach has been shown to be reasonably reliable to consider for a controller feedback and initial work has begun to examine an online estimation approach with the FVE and the tire model.

Chapter 6
Conclusions and Recommendations

6.1 Conclusions and Summary

The material presented introduced the concept of an adaptive tire model that utilized a dynamic tire model and can provide valuable insight into the tire friction capacity. The approach was developed by using a nonlinear Kalman filter, the UKF, that enabled joint estimation of tire states and parameters.

The first step was to better understand the model characteristic and performance. The Average Lumped LuGre Friction Tire Model was selected based on the physical representation of the real tire characteristics. Specifically, for its flexibility to define the road conditions within one parameter, and the model's ability to accurately represent past knowledge of tire friction forces. This model provided a form that was based on the past development of tire models that accounted for peak friction performance, tire deflection, and provided a lumped simplified form that could be used in real-time computation.

Once selected, the tire model was evaluated based on the characteristics of each parameter. The steady-state form the model provided insight into the most dominant parameters and reduced the set of variables to consider for parameter estimation. This was further refined as more information was learned about the model's performance and how the observability for the different parameters depended on the type of excitation available. This lead to insights about how to provide an experimentally robust way of finding the relative velocity and limited the parameters evaluated to the tire states and the road adhesion parameter during experiments with limited time windows. The tire model was able to be best integrated with the UKF approach, compared with the EKF, which was alternatively considered. The effective performance of this approached in simulation supported the proceedings to continue with experimentation next.

The experimental results focused on the motion of a vehicle over a flat dry road surface. The first test platform considered was a fully instrumented test vehicle that contained in-wheel hub sensors. These hub sensors provided all four wheels with instantaneous force and moment load information.

The force data along with the vehicle kinematic motion and physical properties, allowed the desired input and feedback conditions necessary to evaluate the estimation technique. The first set of test considered only of longitudinal motion. Due to the level of success obtained from these results, the model was extended to include the lateral direction. This too provided strong agreement with the friction estimation. The tire capacity provided responses that were physically logical. This was observed with either the vertical load transferring limited the model's performance in a lateral motion or along with hard braking, where the peak braking spikes were observed at the estimated capacity limit.

Once the tire estimation approach was established the last step was to perform the entire process using estimated forces instead based on the FVE method. This approach has made the project significantly more feasible to apply to normal production vehicles. The same vehicle was once again evaluated using the FVE force feedback. Here the process can be noted that both estimations were best able to estimate forces that were directly linked with vehicle motion. As a result, this approach to providing feedback to the tire model was more logical than the full sensory data that required the static vehicle loading to be removed from the data as a constant offset.

Lastly, the entire process was repeated with a fully electric vehicle. All of the force information was obtained by an estimation using the full vehicle response with the FVE and feedback was provided just as before. The entire tire model parameters set was identified using techniques developed with limited available information. In the end, the entire method was applied successfully and once the parameters were estimated, the method was able to provide reasonably accurate estimations for several test cases, thereby strengthening the confidence in the approach taken.

Overall, the method prepared has been able to perform up to the desired goals and has made the initial investigation into an adaptive tire model feasible. Further development to extend the capabilities of this approach along with improved model accuracy will enable this method to be employed on future vehicles.

6.2 Future Work

The material presented has been an initial process to obtain insight into the tire model with an adaptive approach. As a result, many areas of interest are open for further investigation. One such example is the inclusion of the wheel camber angle and accounting for the tire vertical loading more accurately. These two considerations can work together to improve the model fidelity. For such an extension to occur, additional information regarding the suspension motion, the tire patch loading, and how both components change during operation is required. Alternatively, if vehicle testing were to be performed on a variety of road surfaces of known characteristics, then the tire model performance and estimation could be more adequately evaluated. This process could then consider wet, icy, or snow covered road surfaces. Lastly, the project direction would ideally allow the tire model a greater parameter flexibility to account for slowly changing tire parameters. The inclusion of parallel parameter estimation for such variables would provide a more complete adaptive tire model approach than what was feasible to include within this scope.

Appendix A
Simulation and LuGre Tire Model

Parameter Analysis:

The process of determining the most dominate parameter utilized an understanding of the impact a parameter has given a realistic dataset and using the steady-state model. The vertical loading was selected to be one quarter of the load that a standard sedan would be with a total mass 1400kg. Furthermore, the velocity range considered was ±100km/hr while the slip region was ±0.7 to account for the four possible cases of driving/braking and forward/backward motion. The results are shown from Figure 90 to Figure 98.
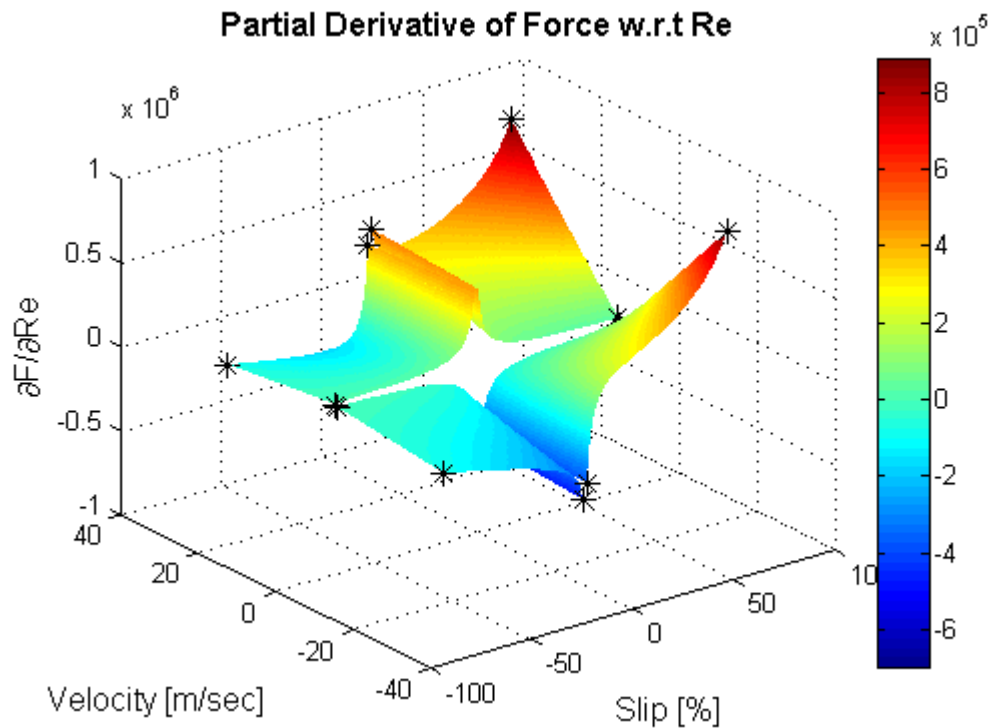
Figure 90: Average Lumped LuGre Steady-State PD for Re

The braking range of Figure 90 becomes unclear as to the magnitude, in order to clarify that the range is still in excess of all other terms Figure 91 was provided to show just the region of braking with the slip is defined from -0.1 to -0.7.
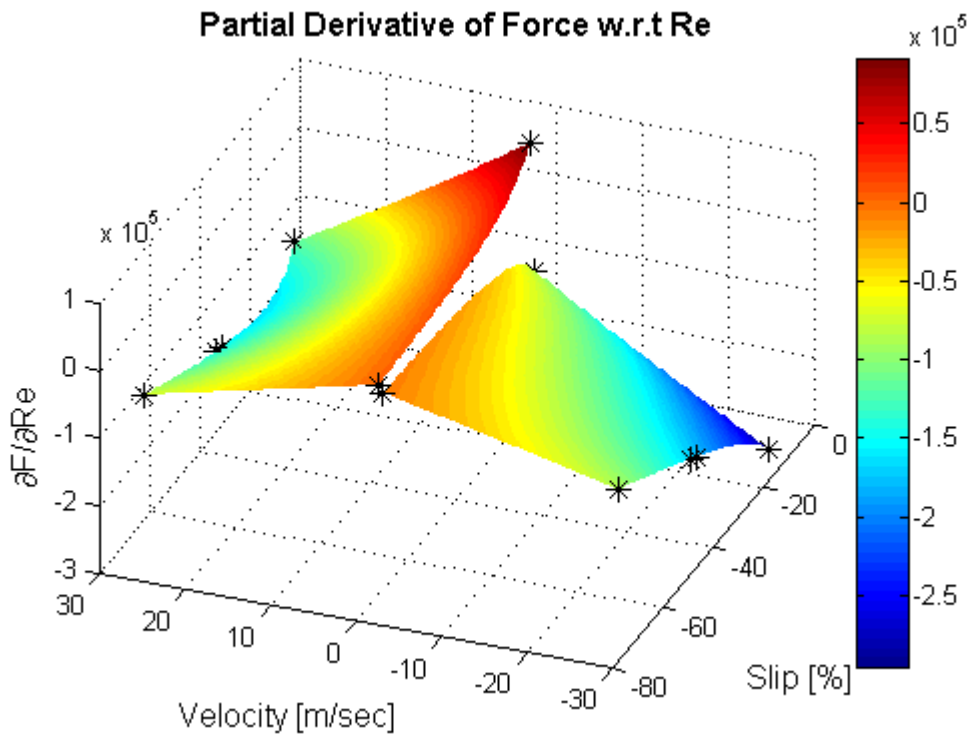
Figure 91: Average Lumped LuGre Steady-State PD for Re Braking Only
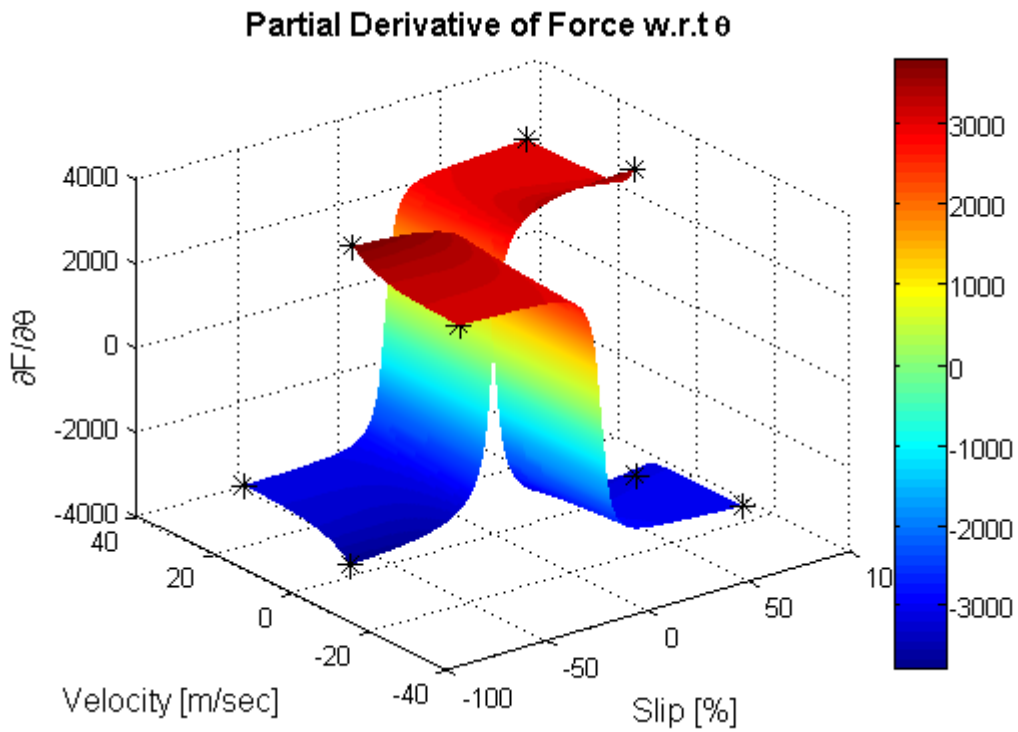
Figure 92: Average Lumped LuGre Steady-State PD for Ɵ
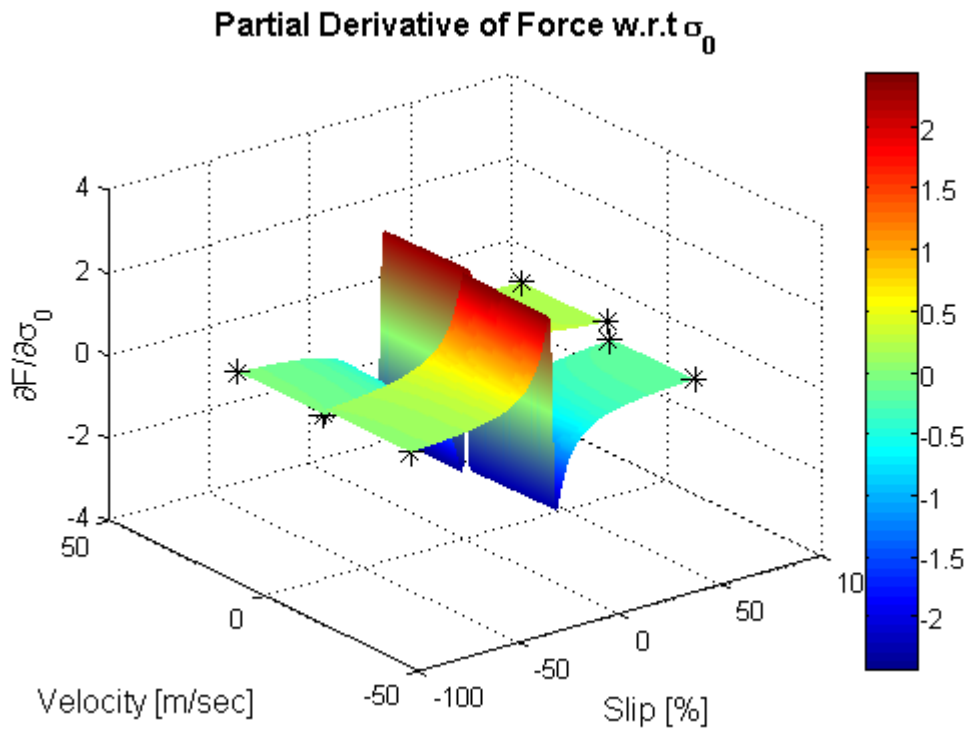
Figure 93: Average Lumped LuGre Steady-State PD for σ_0
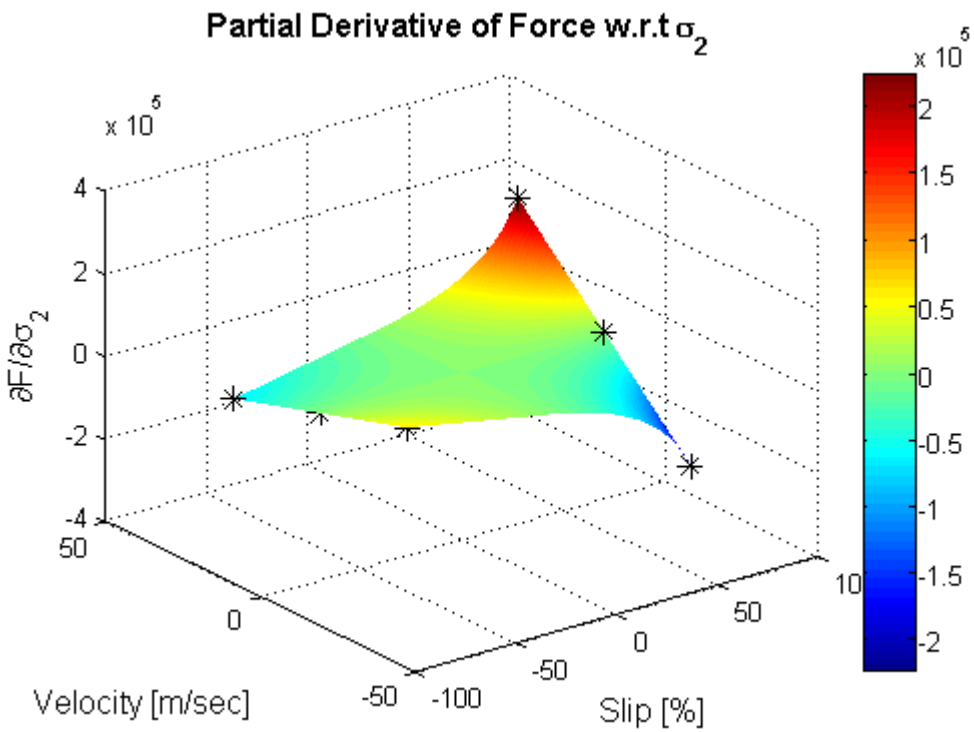
Figure 94: Average Lumped LuGre Steady-State PD for σ_2

115
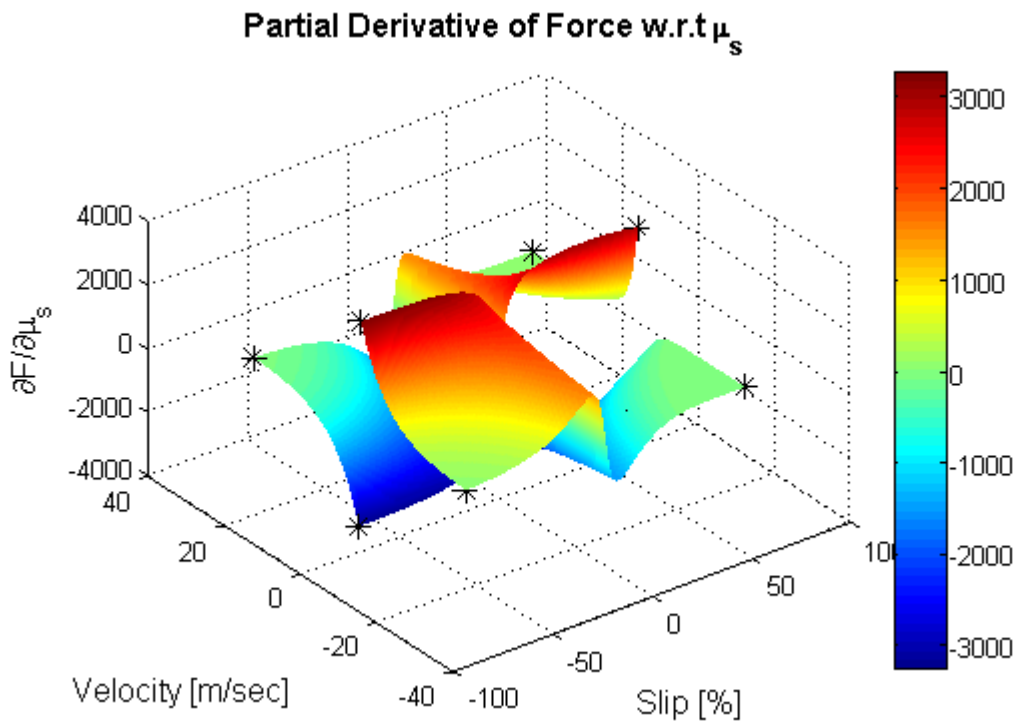
Figure 95: Average Lumped LuGre Steady-State PD for μ$_s$
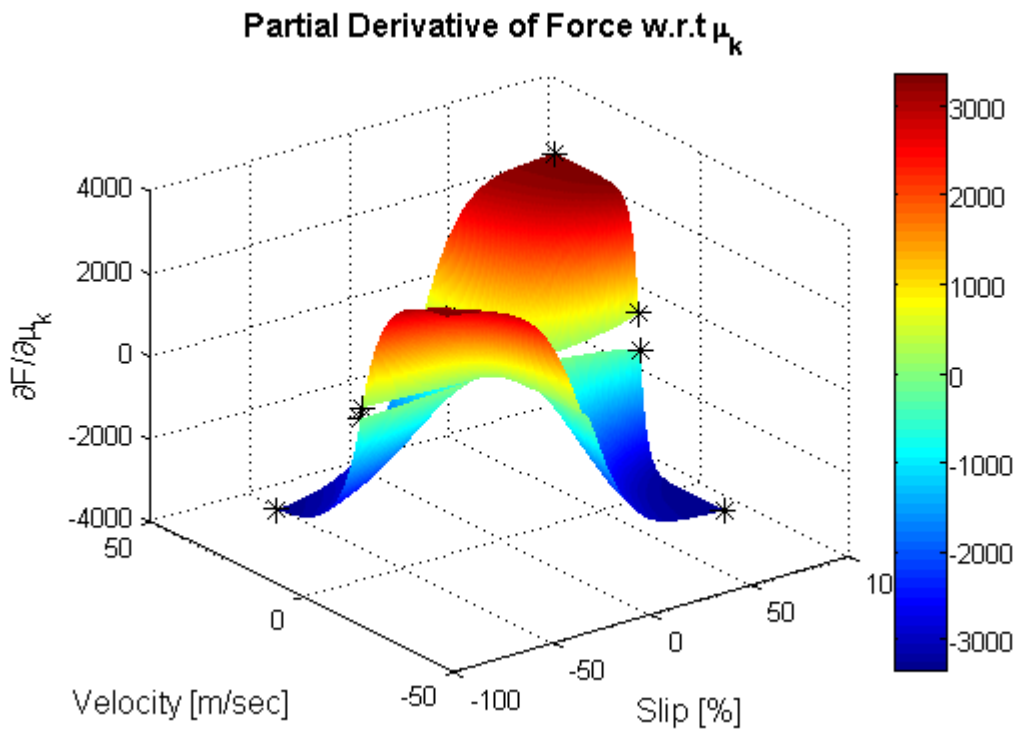
Figure 96: Average Lumped LuGre Steady-State PD for μ$_k$

116
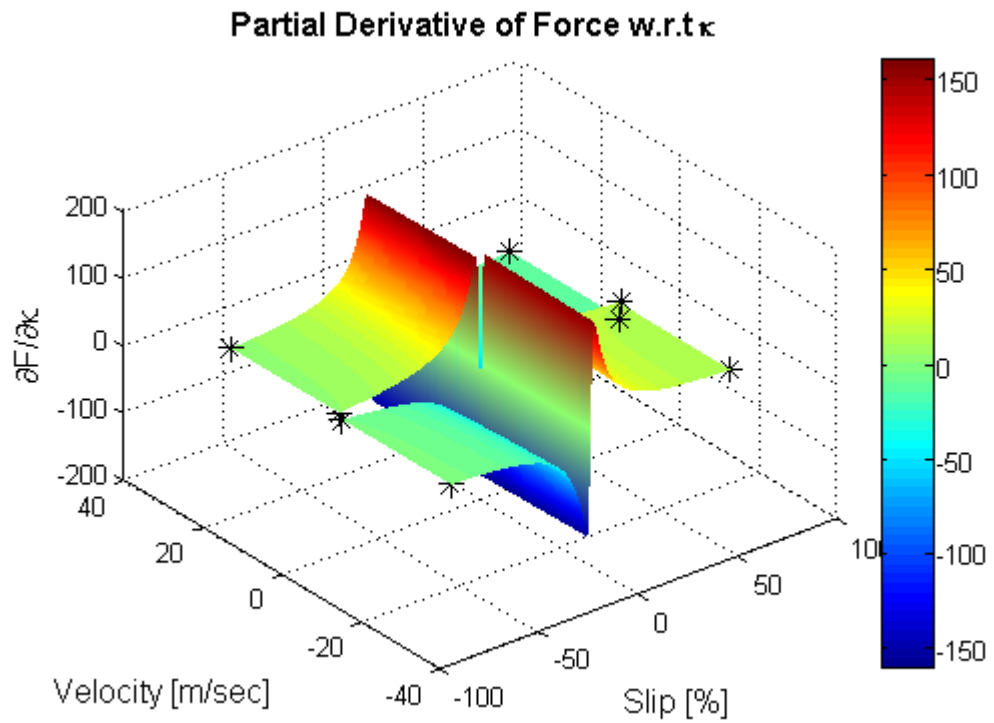
Figure 97: Average Lumped LuGre Steady-State PD for κ
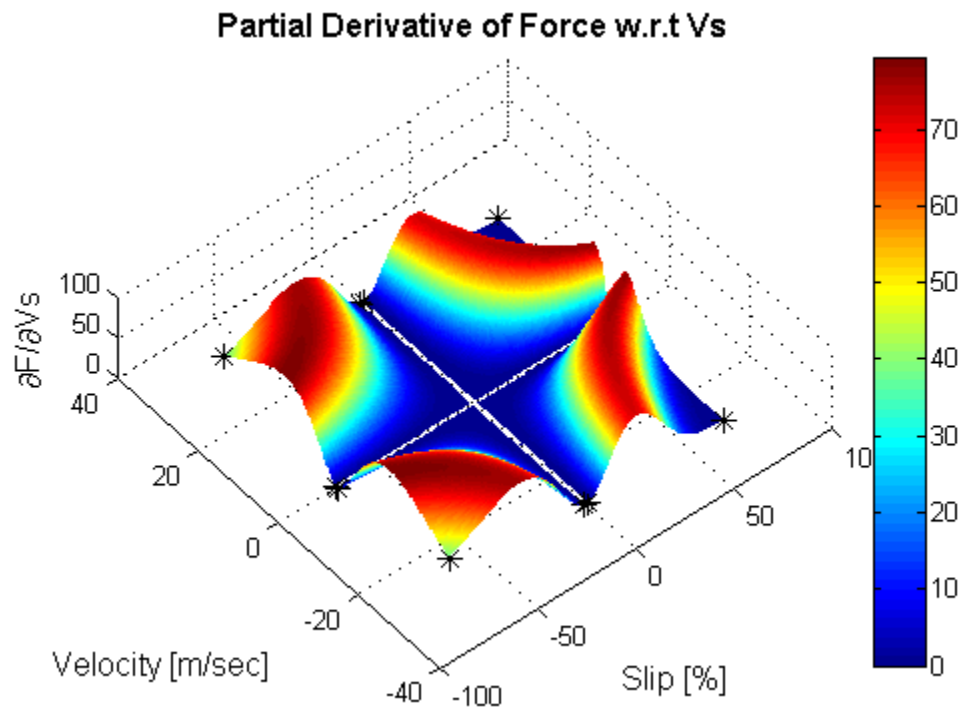
Figure 98: Average Lumped LuGre Steady-State PD for Vs

117

Estimation Analysis:

The tire estimation process was also done considering one less them where the σ_2 was omitted, known as the three term estimation. Additionally, the initial plant state conditions are the three tests as follows: 0.0029m, 0.0029m, and -0.0015919m in the respective order described. The following figures illustrate the results for the three test cases using this reduced estimation set. All of the estimation was performed with the identical configuration from before. The only variations being the testing input and initial state of the plant.

1) Persistent Excitation Test Case:
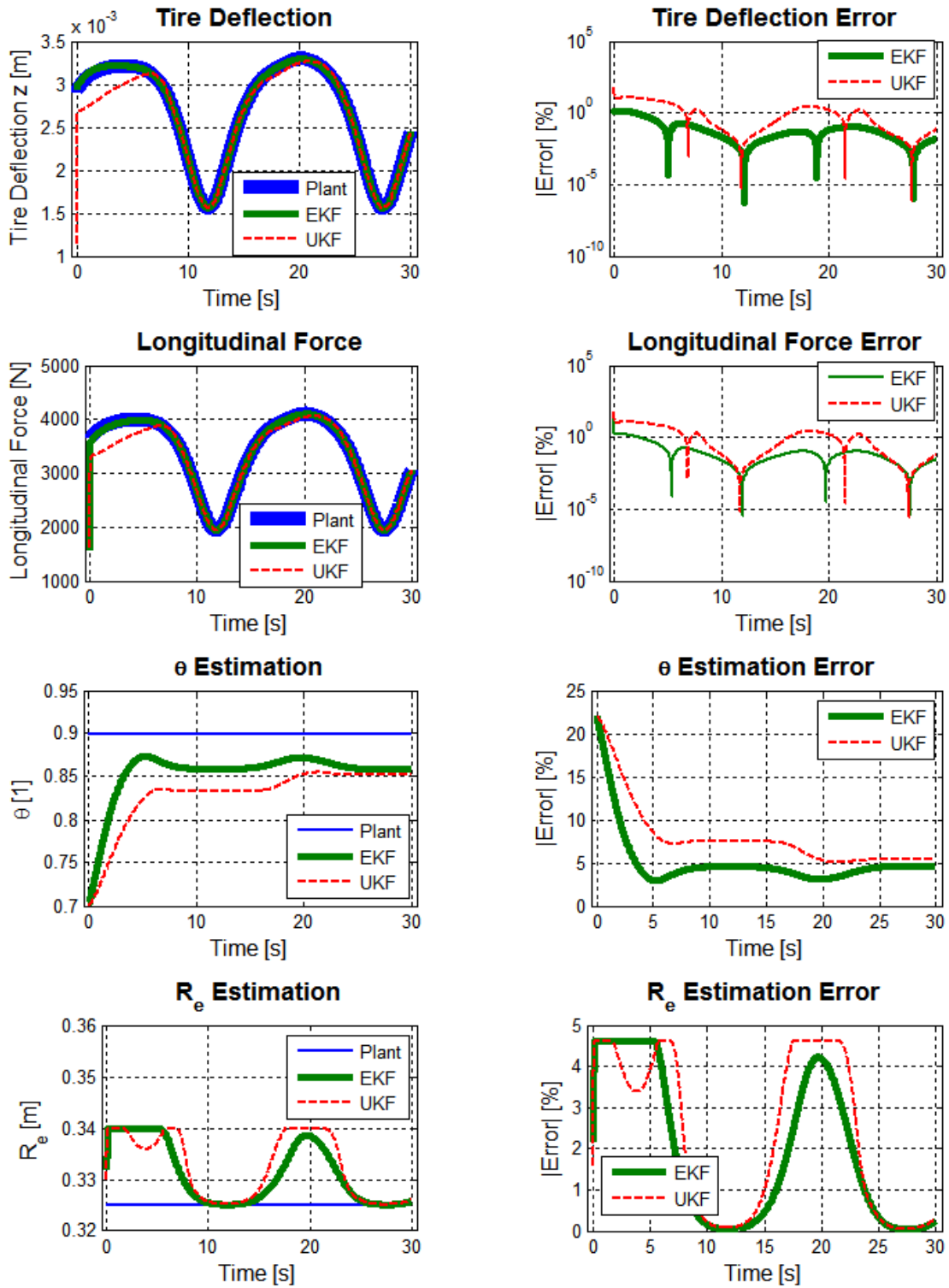
Figure 99: Persistent Excitation 3 Term Estimation

119

2) CarSim® Acceleration and Brake Test Case:
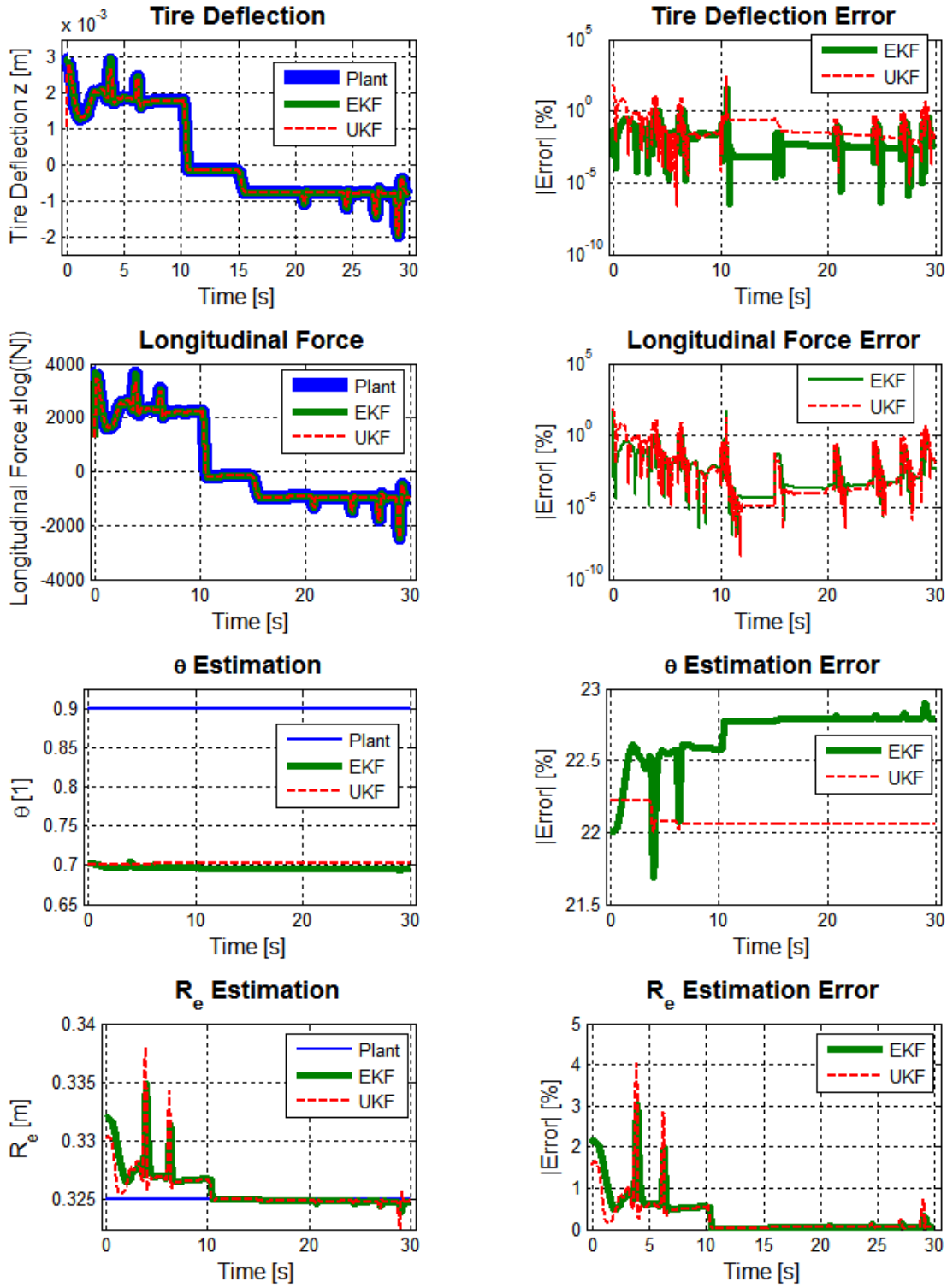
Figure 100: CarSim® Acceleration and Brake Test, 3 Term Estimation

120

3) CarSim® Hard Braking with ABS
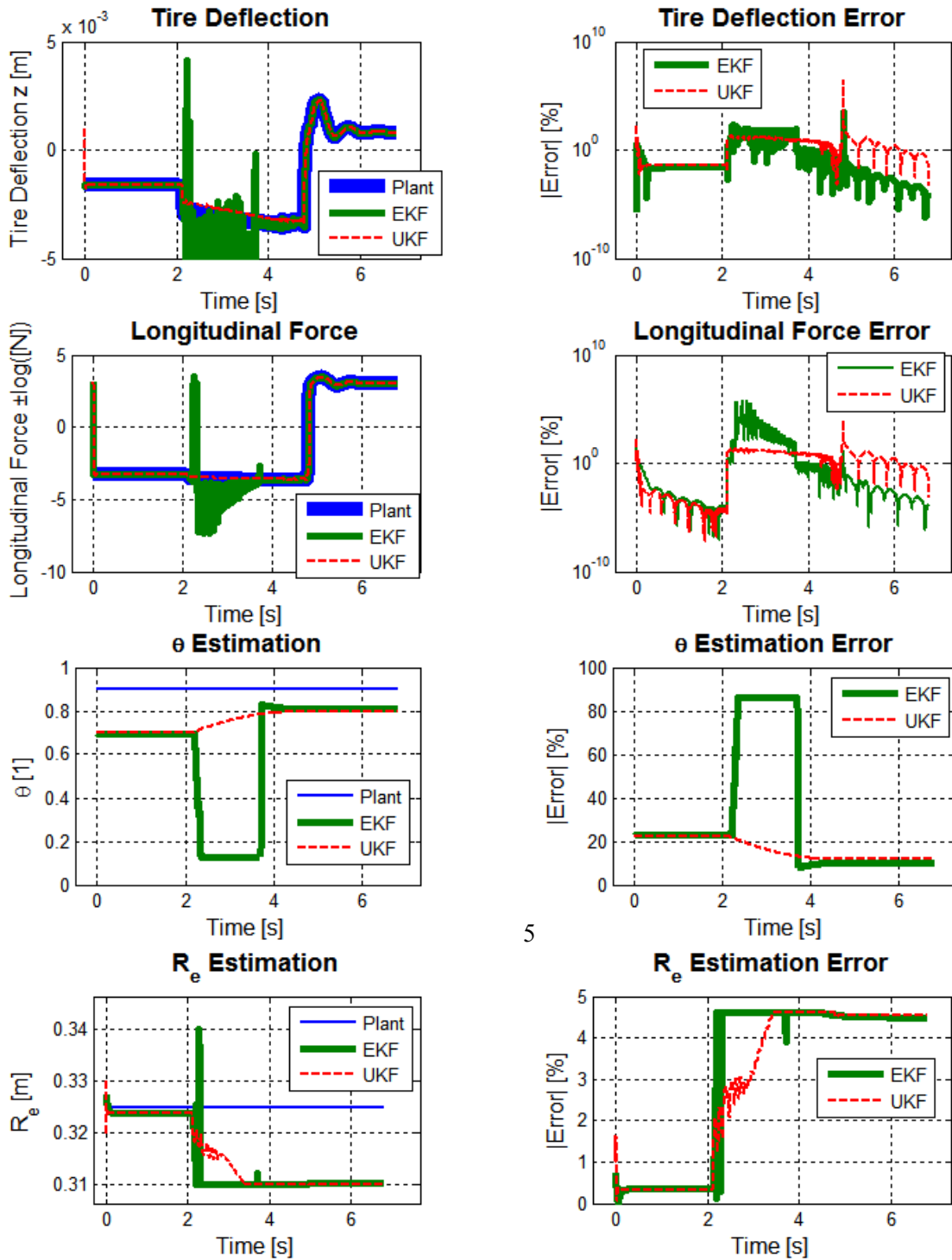
Figure 101: CarSim® Hard Braking with ABS Test, 3 Term Estimation

Appendix B

Details of the GPS and Satellite Graphical Overlay

This section explains how the Global Positioning System (GPS) provided the vehicle's path that was superimposed on top of satellite images to help visualize and understand where the vehicle traveled. Figure 102, is an example of a double lane change completed with notable starting point in green, end point in red, and time data listed as the z-axis at the point being examined.

Figure 102: Vehicle GPS Data Points Superimposed on Google® Satellite Photo [30]

In order to achieve this, a function was written to allow the vector data of the vehicle's GPS data to be displayed over an image representing the terrain that the vehicle traversed. This function takes three inputs: time, the GPS longitudinal vector data, and the corresponding GPS latitude vector data. The function then selects from five possible regions, with the two main areas being the research test track or the University of Waterloo's main campus as shown in Figure 103. The remaining selections are zoomed in subsections of the two main test areas that allowing for a less pixelated image where the vehicle testing normally takes place, such as show in Figure 102.

122

(A) Research Test Facility   (B) University of Waterloo Main Campus

Figure 103: Two Main Test Areas used for Vehicle Research Testing [30]

Once the location is known the most appropriate image is selected. The function then has a simple task of relating the GPS scale to the image scale and superimpose the two atop one another. This relation is done by accounting for the offset and image scale being mirrored vertically compared with the GPS scale. Lastly, the data is plotted with the time information in the z-axis to allow one to review both position and time of the testing. The added markers are provided to clearly indicate the start and end points of the data provided.

The final consideration are that where accounted for, are not performed in the function rather are done in advance. The first being, how to relate two fixed point on the image to two known GPS coordinates. This is achieved by using a webpage resource [31] that relates satellite coverage to GPS data points as illustrated in Figure 104. After that, the process is to ensure that one selects two uniquely identifiable points that are separated vertically and horizontally as much as possible. The large separation is to minimize the effect of error when estimating the specific pixel on the image. Lastly, those same two points are also identified using a photo editing software to reveal the pixel coordinate on the image. The final modification is cosmetic, as the vehicles visible e on the satellite

image can be distracting. The road surface is de-cluttered by editing the photo by overlaying the road surface where the vehicles are captured. The difference can be observed by noting the vehicles in Figure 104 and the absence of vehicles in Figure 102.

Figure 104: Latitude and Longitude Satellite Point [30] and [31]

The detailed code that performs this entire operation is as follows:

```matlab
function GPStoMap (t, pos_lon, pos_lat)

titSize = 13;    % Title  Fontsize 13
lblSize = 12;    % Label  Fontsize 12
legSize = 12;    % Legend Fontsize 12
plotLnw = 2;     % LineWidth 1 or 2

%% Select map
% if (GPSon ==1)

    if (pos_lat (20)> 43.44)
    % UW Campus
        if(min(pos_lat)>43.47625)
            % Lowest point (with padding) to X-lot 43.47625,-80.546619
            map_location = 'X-lot';
        elseif (max(pos_lat>43.474477))
            % North entrence is about lat: 43.474477,long: -80.546329
            map_location = 'Full_Campous';
        else
            map_location = 'Ring_Rd';
        end
    else
    % Test Track
        if ( (min (pos_lon) >-80.5803) && (max(pos_lon) <-80.576295 ) ) %
                    Negative numbers on long set
            map_location = 'Base_Test_Track';
            %Lat: 43.433524 to  43.433571 Long: -80.576295 to -80.5803
        else
            map_location = 'Full_Test_Track';
        end
    end
 % Options for map location are:
        % 'Base_Test_Track'
        % 'Full_Test_Track'
        % 'Full_Campous'
        % 'Ring_Rd'
        % 'X-lot'
%% Image Setup & Definition for Area
    figure;
    % display image of track area
    % From ref: http://itouchmap.com/latlong.html & Google map
    % 'Fire Research Track (zoom).png' or 'Fire Research Track.png'
    switch (map_location)
        case 'Base_Test_Track'
            rgb = imread('..\_Lib Files\map photos\Fire Research Track
                                          (zoom)1200x560.png');
            % Setup used for the image:
            %'Fire Research Track (zoom) 1200x560.png'
            % rgb_width  = 1200; %now simply get from photo!
            % rgb_height =  560;
```

```matlab
        point1_pix = [1183 379];%yvalue = 560 (height) - 181 measured
                                                       from top left
        point2_pix = [ 210 292];%yvalue = 560 (height) - 268 measured
                                                       from top left


        point1_gps = [-80.576493 43.434200]; % Longitude & Latitude
        point2_gps = [-80.579358 43.434023];

    case 'Full_Test_Track'
        rgb = imread('..\_Lib Files\map photos\Fire Research
                                            Track.png');
        % Setup used for the image:
        %'Fire Research Track (zoom) 1200x560.png'
        % rgb_width  = 1046; %now simply get from photo!
        % rgb_height =  884;
        point1_pix = [1034 884-715];%yvalue = 884 (height) - 715
                                          measured from top left
        point2_pix = [ 244 884-219];%yvalue = 884 (height) - 219
                                          measured from top left


        point1_gps = [-80.576493 43.434200]; % Longitude & Latitude
        point2_gps = [-80.580732 43.436123];

    case 'Full_Campous'
        rgb = imread('..\_Lib Files\map
                             photos\campus_drivable_area.jpg');
        % rgb_width  = 1158; %now simply get from photo!
        % rgb_height = 1563;
        point1_pix = [ 852  1563-628]; %yvalue = 1563 (height) -  628
                                          measured from top left
        point2_pix = [ 480  1563-1376]; %yvalue = 1563 (height) - 1376
                                          measured from top left


        point1_gps = [-80.539405 43.473545]; % Longitude & Latitude
        point2_gps = [-80.543399 43.467717];
    case 'Ring_Rd'
        rgb = imread('..\_Lib Files\map
                             photos\ringroad_drivable_area.jpg');
        % rgb_width  =  940; %now simply get from photo!
        % rgb_height = 1116;
        point1_pix = [ 831  1116-187]; %yvalue =  1116(height) - 187
                                          measured from top left
        point2_pix = [ 459  1116-936]; %yvalue =  1116(height) - 936
                                          measured from top left


        point1_gps = [-80.539405 43.473545]; % Longitude & Latitude
        point2_gps = [-80.543399 43.467717];
    case 'X-lot'
        rgb = imread('..\_Lib Files\map
                             photos\x_parking_drivable_area.jpg');
        % rgb_width  =  297; %now simply get from photo!
        % rgb_height =  248;
        point1_pix = [ 286  248-71]; %yvalue =  248(height) -  71
```

126

```matlab
                                                  measured from top left
            point2_pix = [  41  248-210]; %yvalue =  248(height) - 210
                                                  measured from top left

            point1_gps = [-80.544490 43.477738]; % Longitude & Latitude
            point2_gps = [-80.547108 43.476660];
    end

    %% Define Image Scale with GPS Scale
    % bw = imread('Fire Research Track.png');
    % b = bwboundaries(bw);
    imshow(rgb)    %Show Image
    [rgb_height, ~, ~] = size(rgb); %obtain image size!

    hold on
    % From point 1&2 find out the ratios/ slop relation
    delta_pix_x = point1_pix(1) - point2_pix(1);
    delta_pix_y = point1_pix(2) - point2_pix(2);

    delta_gps_x = point1_gps(1) - point2_gps(1);
    delta_gps_y = point1_gps(2) - point2_gps(2);

    % Find out zero ref value
    x_zero = point2_pix(1) - point2_gps(1) *(delta_pix_x/delta_gps_x);
    y_zero = point2_pix(2) - point2_gps(2) *(delta_pix_y/delta_gps_y);

    %% Scale Path Taken to Image from GPS Info
    % Find out other end of photo based on photo size
    path_x = pos_lon.* (delta_pix_x/delta_gps_x) + x_zero;
    path_y = pos_lat.* (delta_pix_y/delta_gps_y) + y_zero;

    %% Plot Path & Start/End Points
      % plot(path_x, rgb_height-path_y,'LineWidth',plotLnw);
      % Shows the path the vehicle moved
    % Using 3D plot with z as time, we know what time step the car is at
    % during the process, and view on plot details
    plot3(path_x, rgb_height-path_y,t,'LineWidth',plotLnw);
    % Shows the path the vehicle moved
    hold on;
    plot(path_x(1),   rgb_height-path_y(1),
          '-o','Color',[0.235,0.85,0.235],'LineWidth',plotLnw*3 );
      % Shows the starting point
    plot(path_x(end), rgb_height-path_y(end),
      '-o','Color',[0.85,0.235,0.235],'LineWidth',plotLnw*3 );
      % Shows the end point

    title({'Path Driven During Experiment'},'FontSize',titSize)
    % ylabel({'Latitude'},'FontSize',lblSize);
    % xlabel('Longitude','FontSize',lblSize);
    % grid on;

    hold off
end
```

Bibliography

[1]   G. Rill, *Vehicle Dynamics Lecture Notes,* Regensburg University of Applied Sciences, 2006.

[2]   Y. Hsu, Estimation and Control of Lateral Tire Forces Using Steering Torque, Stanford University, 2009.

[3]   H. B. Pacejka, Tyre and Vehicle Dynamics, Butterworth-Heinemann, 2006.

[4]   H. Pacejka and R. Sharp, "Shear Force Development by Pneumatic Tyres in Steady State Conditions: A Review of Modelling Aspects," *Vehicle System Dynamics,* vol. 20, no. 3-4, pp. 121-175, 1991.

[5]   E. Bakker, L. Nyborg and H. Pacejka, "Tyre Modelling for Use in Vehicle Dynamics Studies," *Society of Automotive Engineers, Technical Paper 870421,* 1987.

[6]   C. Carlson, *Estimation with Applications for Automobile Dead Reckoning and Control,* Stanford University, Mechanical Engineering, 2004.

[7]   C. Canudas-de-Wit, P. Tsiotras, E. Velenis, M. Basset and G. Gissinger, "Dynamic Friction Models for Road/Tire Longitudinal Interaction," *Vehicle System Dynamics,* vol. 39, no. 3, pp. 189-226, 2003.

[8]   J. Deur, J. Asgari and D. Hrovat, "A 3D Brush-type Dynamic Tire Friction Model," *Vehicle System Dynamics,* vol. 42, no. 3, pp. 133-173, 2004.

[9]   R. T. Uil, *Tyre models for steady-state vehicle handling analysis,* Eindhoven University of Technology, 2007.

[10] E. Velenis, P. Tsiotras and C. Canudas-de-Wit, "Extension of the Lugre Dynamic Tire Friction Model to 2D Motion," in *Proceedings of the 10th IEEE Mediterranean Conference on Control and Automation*, 2002.

[11] E. Velenis, P. Tsiotras and C. Canudas-de-Wit, "Dynamic Tyre Friction Models for Combined Longitudinal And Lateral Vehicle Motion," *Vehicle System Dynamics,* vol. 43, no. 1, pp. 3-29, 2005.

[12] C. Canudas-de-Wit and R. Horowitz, "Observers for tire/road contact friction using only wheel angular velocity information," in *Decision and Control, Proceedings of the 38th IEEE Conference on*, 1999.

[13] C. Canudas-de-Wit, R. Horowitz and P. Tsiotras, "Model-Based Observers for Tire/Road Contact Friction Prediction," *New Directions in nonlinear observer design SE - 2, Lecture Notes in Control and Information Sciences,* vol. 244, pp. 23-24, 1999.

[14] C. Canudas-de-Wit and P. Tsiotras, "Dynamic tire friction models for vehicle traction control," in *Decision and Control, 1999. Proceedings of the 38th IEEE Conference on*, 1999.

[15] C. Canudas-de-Wit, H. Olsson, K. J. Astrom and P. Lischinsky, "A New Model for Control of Systems with Friction," *IEEE Automatic Control,* vol. 40, no. 3, pp. 419-425, 1995.

[16] P. Tsiotras, E. Velenis and M. Sorine, "A Lugre Tire Friction Model with Exact Aggregate Dynamics," *Vehicle System Dynamics,* vol. 42, no. 3, pp. 195-210, 2004.

[17] S. Haykin, "Kalman Filters," in *Kalman Filtering and Neural Networks*, Toronto, John Wiley & Sons, Inc, 2001, pp. 1-21.

[18] R. E. Kalman, "A New Approach to Linear Filtering and Prediction Problems," *Transactions of the ASME–Journal of Basic Engineering,* vol. 82, no. Series D, pp. 35-45, 1960.

[19] S. J. Julier, J. K. Uhlmann and H. F. Durrant-Whyte, "A New Approach for Filtering Nonlinear Systems," *American Control Conference,* vol. 3, pp. 1628,1632, 1995.

[20] E. A. Wan and A. T. Nelson, "Dual Extended Kalman Filter Methods," in *Kalman Filtering and Neural Networks*, Toronto, John Wiley & Sons, Inc, 2001, pp. 123-173.

[21] E. A. Wan and R. V. D. Merwe, "The Unscented Kalman Filter," in *Kalman Filtering and Neural Networks*, John Wiley & Sons, Inc, 2001, pp. 221-280.

[22] R. Van Der Merwe, *Sigma-Point Kalman Filters for Probabilistic Inference in Dynamic State-Space Models,* Oregon Health & Science University, 2004.

[23] A. Asadian, M. R. Kermani and R. V. Patel, "A Compact Dynamic Force Model for Needle-Tissue Interaction," in *Engineering in Medicine and Biology Society (EMBC), Annual International Conference of the IEEE*, 2010.

[24] C. Yan and J. Wang, "Vehicle-longitudinal-motion-independent real-time tire-road friction coefficient estimation," in *Decision and Control (CDC), 49th IEEE Conference on*, 2010.

[25] W. Liang, J. Medanic and R. Ruhl, "Analytical dynamic tire model," *Vehicle System Dynamics,* vol. 46, no. 3, p. 197–227, 2008.

[26] J. Bernard and C. Clover, "Tire Modeling for Low-Speed and High-Speed Calculations," *SAE*

Technical Paper, no. 950311, 1995.

[27] P. Loannou and B. Fidan, Adaptive Control Tutorial, Philadelphia: Society for Industrial and Applied Mathematics, 2006.

[28] S. S. Rao, Applied Numerical Methods for Engineers and Scientists, Upper Saddle River, N.J: Prentice Hall, 2002.

[29] *Wheel Load Measurement System For Passenger Cars and Light Trucks, Revision 2.0, Michigan Scientific Corporation,* Milford, MI, 2008.

[30] "Region of Waterloo Emergency Services Training Area Satellite Image, Google Maps," Google, 2012. [Online]. Available: maps.google.ca. [Accessed 2012].

[31] "Region of Waterloo Satellite Image," iTouchMaps, [Online]. Available: http://itouchmap.com/latlong.html. [Accessed 2012].

[32] R. Van Der Merwe and E. A. Wan, "The Square-Root Unscented Kalman Filter for State and Parameter-Estimation," in *Proceedings of the IEEE International Conference, Acoustics, Speech, and Signal Processing*, Salt Lake City, 2001.

[33] Y. Chen and J. Wang, "Vehicle-Longitudinal-Motion-Independent Real-Time Tire-Road Friction Coefficient Estimation," in *Decision and Control (CDC), IEEE Conference*, 2010.